This file is a self-archived copy of the following article:

John G. Stevens and Michael J. Ruiz, "Mössbauer Spectroscopy," Chapter 6 *in Treatise on Analytical Chemistry Part I, Volume 10 Theory and Practice*, 2nd edition, edited by P. J. Elving, M. M. Bursey, and I. M. Kolthoff, 439 (John Wiley, New York 1983).

"This article may be used for non-commercial purposes in accordance with Wiley Terms and Conditions for Use of Self-Archived Versions. This article may not be enhanced, enriched or otherwise transformed into a derivative work, without express permission from Wiley or by statutory rights under applicable legislation. Copyright notices must not be removed, obscured or modified. The article must be linked to Wiley's version of record on Wiley Online Library and any embedding, framing or otherwise making available the article or pages thereof by third parties from platforms, services and websites other than Wiley Online Library must be prohibited."

For the latest resources on this topic, consult the Wiley Online Library (Analytical Chemistry).

Courtesy Wiley

© WILEY

Offprints From: Treatise on Analytical Chemistry, 2/ed, Pt. 1, V. 10.
Edited By: Philip J. Elving; Editor Emeritus: I. M. Kolthoff.
Published By: John Wiley & Sons, Inc., 1983

Part 1
Section I

Chapter 6

MÖSSBAUER SPECTROSCOPY

BY JOHN G. STEVENS AND MICHAEL J. RUIZ, *University of North Carolina at Asheville*

Contents

I. Introduction 440
II. Basic Principles 441
III. The Principal Interactions 450
A. Electric Monopole (E0) — Isomer Shift 450
B. Magnetic Dipole (M1) — Magnetic Hyperfine Splitting 452
C. Electric Quadrupole (E2) — Quadrupole Coupling Constant 458
IV. Experimental Methods 460
A. Spectrometers 460
B. Sources 462
C. Detectors 463
D. Absorbers 468
E. Temperature Considerations 469
F. Applied Magnetic Fields 471
G. Velocity Calibration 471
H. Curve Fitting 474
V. Isomer Shift and Its Application 475
A. Electron Density Calculations 475
B. Oxidation States 477
C. Electronegativity 477
D. Partial Chemical Shifts 478
E. Second-Order Doppler Shift 487
F. Phase Analysis 489
1. Phase Transitions 489
2. High Pressure 489
3. Chemical Identification 489
VI. Magnetism 490
A. Line Intensities 490
B. Contributions to the Magnetic Field Interactions 490
C. Magnetic Hyperfine Field Spectra 491
VII. Quadrupole Interaction and Its Application 491
A. Electric Field Gradients 491
B. Spectra 497
C. Additive Model 506
VIII. Spin Hamiltonian and Relaxation 506
Acknowledgments 513

Appendix, Nomenclature and Conventions for Reporting Mössbauer Spectroscopic Data 513
I. Introduction 513
II. Conventions for the Reporting of Mössbauer Data 513
A. Text 513
B. Numerical or Tabulated Data 514
C. Figures Illustrating Spectra 514
III. Terminology, Symbols, and Units 515
References 521

I. INTRODUCTION

Spectroscopic methods are important analytic tools in the study of various microscopic systems such as nuclei, atoms, molecules, and crystal lattices. The knowledge gained from the study of the various absorption, emission, or reemission processes in microscopic systems is generally of interest either to the nuclear physicist or to the solid-state physicist and the chemist, but seldom to both groups simultaneously. Mössbauer spectroscopy, however, makes very enriching contributions to both fields. This spectroscopy is based on observing recoilless emission and resonance absorption of gamma rays by nuclei in solids. Resonance absorption of gamma rays had been predicted since the beginning of this century; however, experimental observation of this behavior was difficult due to the amount of energy lost in the recoil of a nucleus emitting and/or absorbing a gamma ray. Below, we briefly describe this problem.

From a classical point of view, a free atom of mass m, moving in the x direction with a given velocity v, has a linear momentum of mv. If this free atom is in an excited nuclear state and undergoes an energy transition to the corresponding ground state by emitting a gamma ray, the momentum of the system must be conserved. To conserve momentum, the momentum of the emitted gamma ray must be balanced by a change in the velocity of the nucleus. This change in the velocity imparts to the nucleus an energy associated with its recoil after emission. In most optical spectroscopic studies, this loss of energy due to recoil is insignificant because it is much less than the experimental spectral line width. However, in the study of the recoilless emission and resonance absorption of gamma rays, the energy lost due to recoil is much greater than the line width and thus becomes an important factor.

In pre-Mössbauer time, several experimental methods were utilized to either broaden the line width or add to the energy of the gamma ray to make up for the loss in recoil. One such method was the utilization of the Doppler effect by accelerating the source toward the absorber in an attempt to compensate for the energy lost in recoil. Temperature broadening and the use of recoil momentum imparted by a preceding transition were also successfully employed in some cases in restoring energy lost due to recoil. However, these techniques did not afford the opportunity to observe hyperfine interactions due to the large broadening of the lines which were necessarily incurred.

In 1958 Rudolph L. Mössbauer discovered that recoilless emission and resonance absorption of gamma rays could be observed if solid substances were used (28). Without the need to compensate for energy loss due to recoil, line widths were greatly

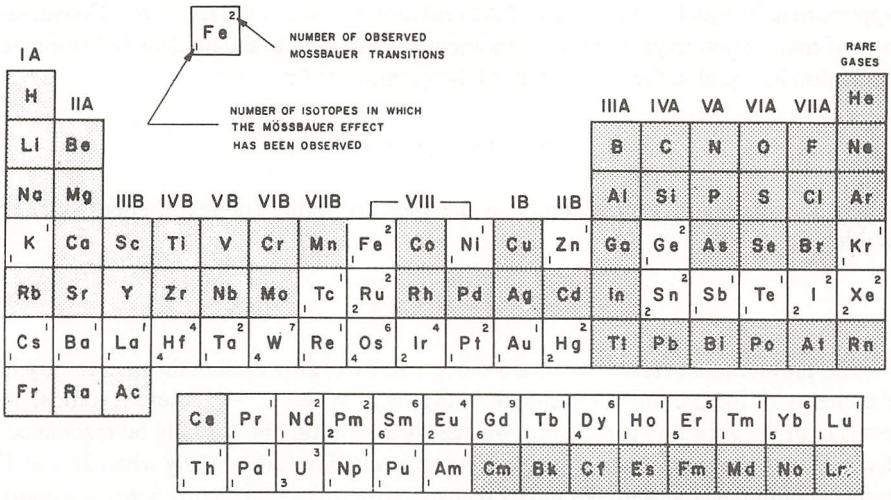

Fig. 6.1. Mössbauer periodic table.

reduced to the order of 10^{-7} eV. A high-resolution technique of this type enables one to observe hyperfine interactions and thus study events affecting the nucleus and its immediate environment.

This recoilless resonance phenomenon, which is referred to as the Mössbauer effect or nuclear gamma resonance (NGR), has been reported for over 100 nuclear gamma ray transitions. The elements in which these transitions are observable are shown in Fig. 6.1.

II. BASIC PRINCIPLES

NGR is the process whereby a gamma ray emitted during the transition of a nucleus from an excited to a ground level excites an identical nucleus in the reverse manner. This process is the basis of the Mössbauer effect. However, the unique characteristic of the Mössbauer effect is the ability to observe hyperfine interactions. This can largely be attributed to emission and absorption of the gamma ray by the nucleus without any loss of energy or line broadening due to recoil.

To fully appreciate the significance of recoilless emission, we will examine gamma emission from a classical point of view. Consider a nucleus of mass m at rest in an excited state. If during a transition from this excited state to the ground state, the nucleus emits a photon of energy E_γ, then, the conservation of energy principle states that the change in energy of the nucleus (E_0) due to the transition must be equal to the quantum of energy carried away by the photon plus the recoil kinetic energy (E_r) gained by the nucleus due to the emission process. Therefore, conservation of energy requires that

$$E_e - E_g = E_0 = E_\gamma + E_r \tag{1}$$

where E_e is the energy of the excited state and E_g is the energy of the ground state. For there to be appreciable resonance absorption, the energy of the transition must be

approximately equal to the energy of the radiation emitted, i.e., $E_0 \approx E_\gamma$. Conservation of momentum requires that the momentum imparted to the nucleus (p) from the transition be equal to the momentum of the gamma ray (p_γ), i.e.,

$$p = m\mathrm{v} = p_\gamma = \frac{E_\gamma}{c} \tag{2}$$

where v is the recoil velocity and c is the speed of light. The recoil energy can be written as

$$E_r = \tfrac{1}{2} m\mathrm{v}^2 = \frac{E_\gamma^2}{2mc^2} \tag{3}$$

The problem that results when the recoil energy is greater than the uncertainty in the energy of the photon (Γ) is shown in Fig. 6.2. When $E_r \approx \Gamma$ there is almost no overlap of the emission and absorption energies, resulting in virtually no resonance. Even for cases where $2E_r \approx \Gamma$, there is no appreciable overlap. Only when $3E_r \leqslant \Gamma$ is there significant overlap. For most other spectroscopies, the recoil energy is usually much smaller than the line width and resonance occurs frequently.

Now consider an atom bound inside a solid. If for low-energy nuclear gamma rays, the atom containing the nucleus of interest is bound strongly enough to its nearest neighbors, there is a probability that the entire solid will recoil instead of the individual atom. In this case, the mass in equation 3 must be replaced by the mass of the bulk material. The larger mass of the solid results in an extremely small recoil energy, virtually allowing for complete overlapping of the emission and absorption

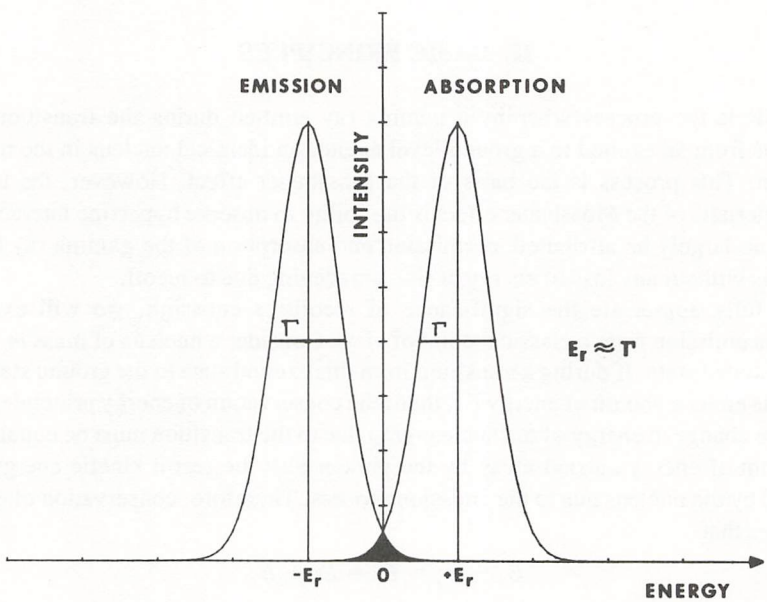

(a)

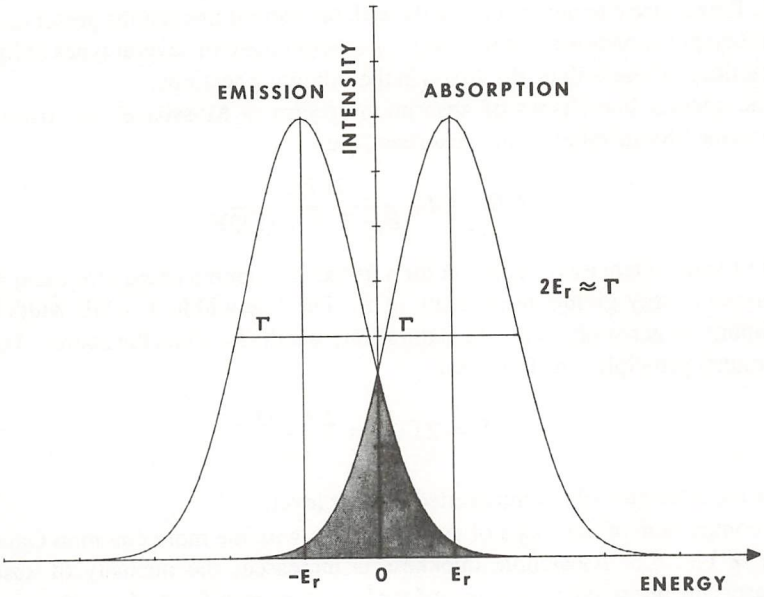

(b)

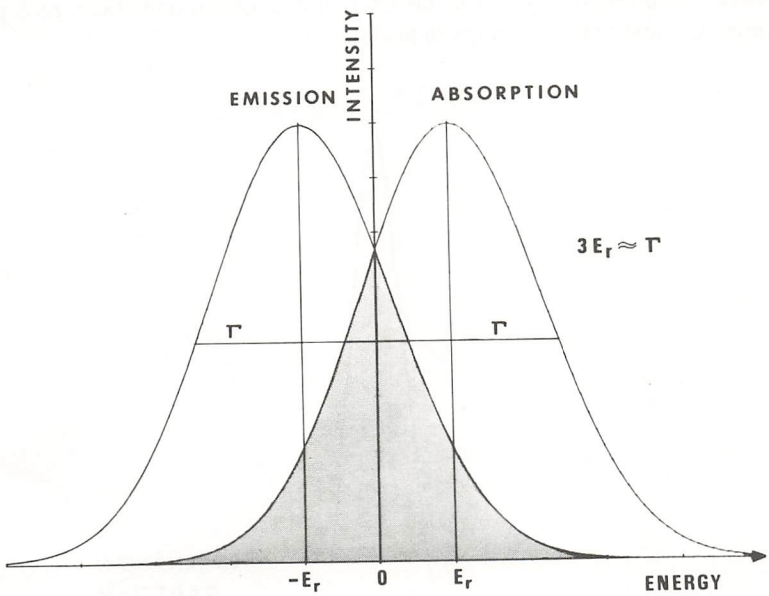

(c)

Fig. 6.2. Emission and absorption Lorentzian lines as a function of relative values of the recoil energy (E_r) and the line width (Γ). (*a*) $E_r \approx \Gamma$, (*b*) $2E_r \approx \Gamma$, and (*c*) $3E_r \approx \Gamma$.

lines. Resonance can now occur easily with the natural line widths preserved, a very important phenomenon since it allows for measurement of several types of hyperfine interactions. These will be discussed in the following sections.

The general line shapes of absorption spectra in Mössbauer spectroscopy are Lorentzian "for infinitely thin" absorbers, i.e.,

$$I(E_\gamma) = I_0 \frac{(\Gamma/2)^2}{(E_\gamma - E_0)^2 + (\Gamma/2)^2} \tag{4}$$

where I is the intensity of radiation for a particular gamma energy (E_γ) and E_0 is the resonance energy giving an intensity of I_0. The line width, Γ, (full width at half-maximum) is generally twice the natural line width (Γ_{NLW}) of the source. Using the uncertainty principle, one finds that

$$\Gamma = 2\,\Gamma_{NLW} = \frac{2\,\hbar\,\ln 2}{t_{1/2}} \tag{5}$$

where $t_{1/2}$ is the half-life of the excited nuclear level.

A comparison of the shape of the Lorentzian with the more common Gaussian is made in Fig. 6.3. As sample thickness is increased, the intensity of absorption increases, the line width broadens, and the line shape goes from a Lorentzian to that of a Gaussian. Before we define a "thin" or "thick" absorber, resonance cross sections and Mössbauer fractions will be discussed.

The general laws of quantum mechanical scattering give the cross-section for resonance, assuming a single line, no internal conversion and 100% zero phonon absorption (no loss of recoil energy to the lattice) as

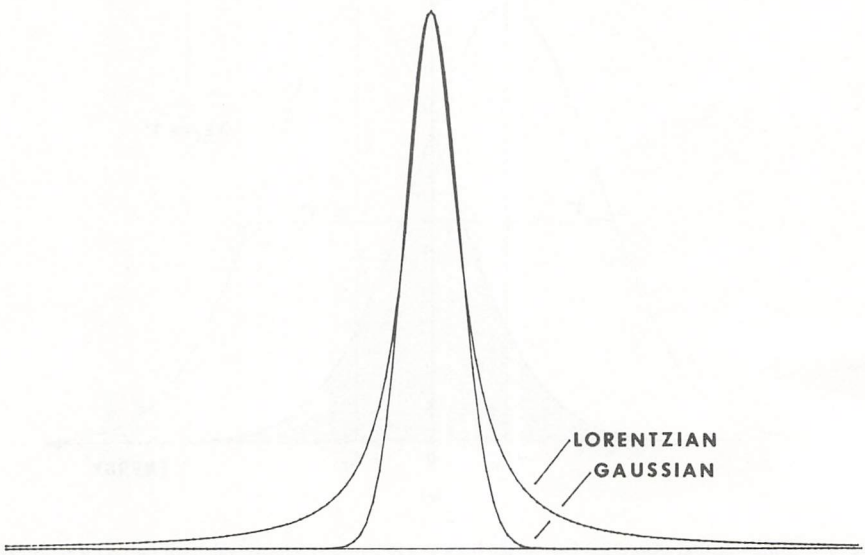

Fig. 6.3. Comparison of Lorentzian and Gaussian line shapes.

$$\sigma_0 = 2\pi\lambda\!\!\!^{-2}\frac{(2I_e + 1)}{(2I_g + 1)} \tag{6}$$

where $\lambda\!\!\!^{-}$ is the wavelength of the photon divided by 2π, I_e is the nuclear spin of the excited level, and I_g is the nuclear spin of the ground level. For most Mössbauer transitions internal conversion (IC) must be considered. Internal conversion is the deexcitation of an excited nucleus in which energy is carried away by the emission of an atomic electron. Inclusion of internal conversion modifies equation 6, giving for the resonance cross-section

$$\sigma_0 = 2\pi\lambda\!\!\!^{-2}\frac{(2I_e + 1)}{(2I_g + 1)} \cdot \frac{1}{(\alpha + 1)} \tag{7}$$

where α, the internal conversion coefficient, is the ratio of the probability of internal conversion to that of gamma emission.

To appreciate how large this cross section is, a comparison can be made between the actual geometric cross section of the nucleus and the calculated cross section from equation 7. For the case of the 14.4 keV transition in ^{57}Fe, the ratio of the Mössbauer resonance cross section to the nuclear geometric cross section is approximately 2.5×10^6.

This is the most dramatic of the Mössbauer transitions and is the main reason that the ^{57}Fe transition is the one most often used in Mössbauer spectroscopy. This and other more common Mössbauer transitions are listed in Table 6.I with useful

TABLE 6.I

Parameters for Selected Mössbauer Transitions

Isotope	Isotope abundance (%)	E_γ (keV)	I_e I_g	Half life $t_{1/2}$ (ns)	Internal conversion coefficient	Mössbauer cross section (10^{-20} cm^2)	Mössbauer line width (mm/s)
^{57}Fe	2.14	14.41	3/2 1/2	97.8	8.21	256	0.194
^{61}Ni	1.19	67.41	5/2 3/2	5.27	0.135	71.2	0.770
^{99}Ru	12.72	89.36	3/2 5/2	20.5	1.54	8.0	0.149
^{119}Sn	8.58	23.87	3/2 1/2	17.8	5.12	140	0.647
^{121}Sb	57.25	37.15	7/2 5/2	3.5	11.1	19.5	2.10
^{125}Te	6.99	35.46	3/2 1/2	1.48	13.6	26.6	5.21
^{127}I	100	57.60	7/2 5/2	1.91	3.78	20.6	2.49
^{129}I	[a]	27.77	5/2 7/2	16.8	5.1	39.0	0.586
^{133}Cs	100	81.00	5/2 7/2	6.31	1.72	10.3	0.535
^{151}Eu	47.82	21.53	7/2 5/2	9.7	28.6	23.8	1.31
^{153}Eu	52.18	103.18	3/2 5/2	3.9	1.78	5.46	0.68
^{155}Gd	14.73	86.54	5/2 3/2	6.33	0.43	34	0.499
^{161}Dy	18.88	25.66	5/2 5/2	28.2	2.9	95	0.378
^{166}Er	33.41	80.56	2 0	1.87	6.93	23.8	1.82
^{170}Yb	3.03	84.25	2 0	1.61	8.05	19.0	2.02
^{181}Ta	99.99	6.24	9/2 7/2	6800	46	167	0.0064
^{193}Ir	62.70	73.04	1/2 3/2	6.3	6.5	3.06	0.594
^{197}Au	100	77.34	1/2 3/2	1.88	4.30	3.86	1.88
^{237}Np	[b]	59.54	5/2 5/2	68.3	1.12	31	0.0673

[a] Radioactive, $t_{1/2} = 1.57 \times 10^7 y$.
[b] Radioactive, $t_{1/2} = 2.14 \times 10^6 y$.

information such as nuclear spin states, gamma energies, nuclear lifetimes, line widths, internal conversion coefficients, and cross sections.

The intensity of absorption can be related to two other parameters; these are the sample thickness and the fraction of recoilless emissions. This latter parameter is called the Mössbauer fraction or recoil-free fraction and will be discussed first.

For an emitting atom bound in a lattice, recoil energy can be given to the lattice in the form of vibrational energy (phonons). When this occurs, the emitted gamma has less energy than the transition energy due to the recoil energy gained by the emitting atom. If no energy is given to vibrational excitations in the lattice, the whole lattice recoils. Then the recoil energy is exceedingly small since the recoiling mass is very large, being the mass of the whole crystal. The emitted gamma energy is therefore essentially equal to the transition energy. This is called recoil-free or zero-phonon absorption. When both of these processes take place, there is nuclear gamma resonance.

A simplified description of the above processes can be found in the Einstein model of a lattice, where there is a single vibrational frequency (ν_E) for the atoms. If the recoil energy given by equation 3 is greater than $h\nu_E$, there will not be zero-phonon interactions as the atoms will absorb vibrational energy. However, if the recoil energy is less than $h\nu_E$, then the Mössbauer fraction, i.e., the fraction of recoilless emissions is

$$f = \mathrm{e}^{-\frac{E_r}{k\theta_E}} \tag{8}$$

where $\theta_E = \dfrac{h\nu_E}{k}$ is the Einstein temperature and k is the Boltzmann constant.

This factor can also be written as

$$f = \mathrm{e}^{\frac{-\langle \overline{x^2} \rangle}{\lambda\!\!\!^{-2}}} \tag{9}$$

where $\langle \overline{x^2} \rangle$ is the thermal average of the mean square displacement of the emitting or absorbing atom and $2\pi\lambda\!\!\!^{-}$ is the wavelength of the radiation. This factor was used in earlier X-ray diffraction studies and known as the Debye-Waller factor.

From equation 8, it is evident that the larger the recoil (corresponding to higher gamma energies), the smaller the Mössbauer fraction. Smaller atomic masses give smaller Mössbauer fractions while stronger lattice forces support larger recoilless fractions.

The Einstein model is oversimplified as it considers only one natural frequency for the oscillators. The Debye model is an improved model where a distribution of oscillator frequencies is incorporated into the calculation of the Mössbauer fraction. The distribution in the model is proportional to ν where ν goes from zero to a maximum called the Debye frequency (ν_D). The final result for the Mössbauer fraction is

$$f = \mathrm{e}^{-2W} \tag{10}$$

where

$$W = \frac{3E_r}{k\theta_D}\left[\frac{1}{4} + \left(\frac{T}{\theta_D}\right)^2 \int_0^{\theta_D/T} \frac{x\,dx}{e^x - 1}\right]$$

and $\theta_D = \frac{h\nu_D}{k}$. Plots of equation 10 are given for ^{57}Fe (14.4 keV), ^{121}Sb (37.15 keV), and ^{197}Au (77.34 keV) in Fig. 6.4.

In addition to the effect of the gamma energy and lattice force discussed above, note the additional effect of temperature in the Debye model. Increasing the temperature decreases the recoil-free fraction. Serious consideration must be given to the operating temperature for the experiment. This will be discussed in more detail in the experimental section.

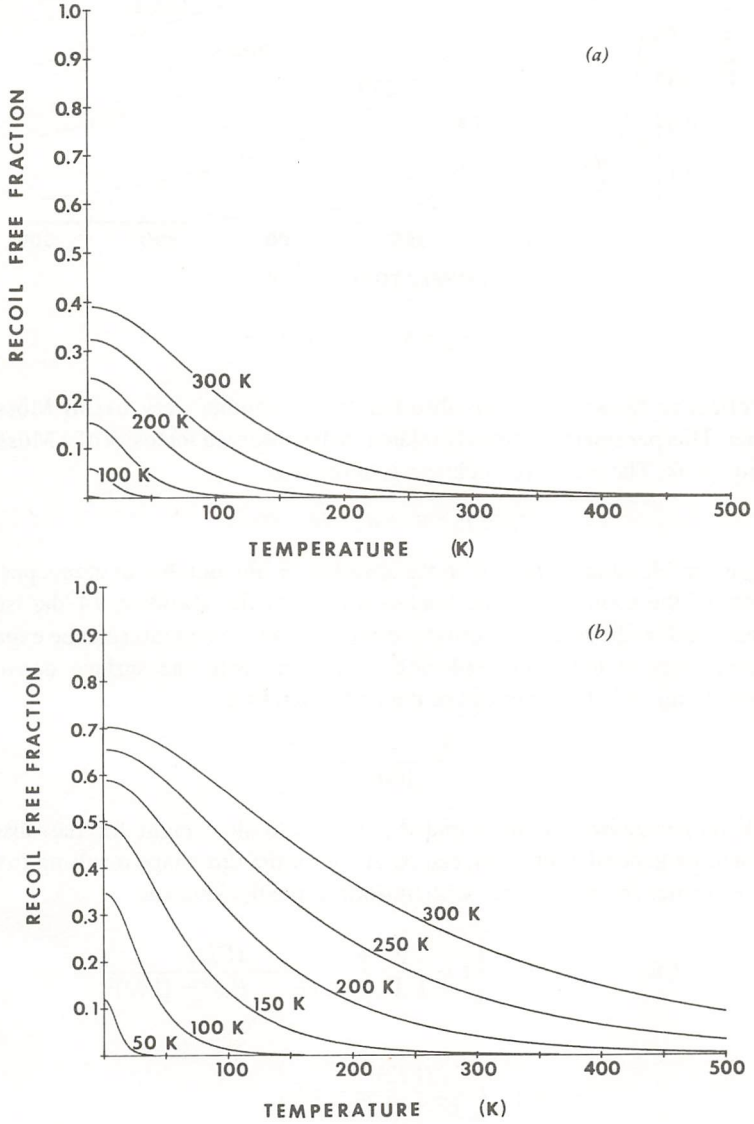

Fig. 6.4. Plots of the Mössbauer fraction versus temperature for various Debye temperatures. (*a*) ^{197}Au, (*b*) ^{121}Sb, and (*c*) ^{57}Fe.

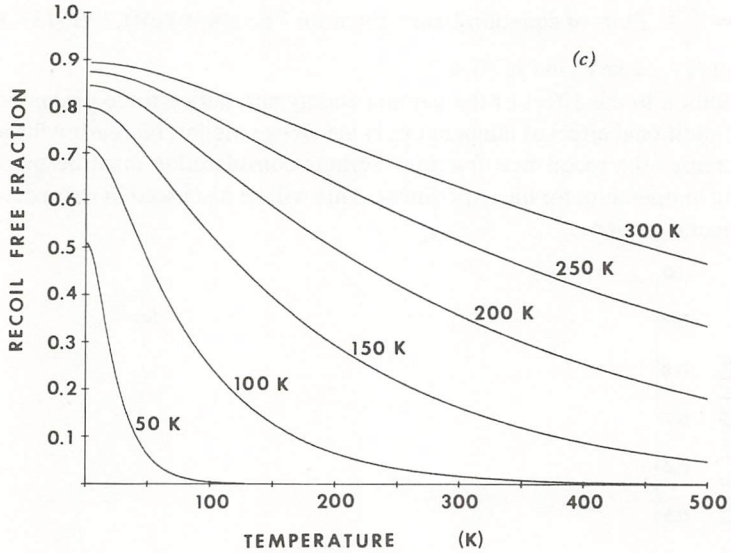

Fig. 6.4. (*Continued*).

The effective thickness for an absorber (t_a) is another very useful Mössbauer parameter. This parameter is directly related to the observed intensity of a Mössbauer absorption peak. The effective thickness is defined as

$$t_a = f_a \cdot n_a \cdot d_a \cdot IA \cdot \sigma_0 \tag{11}$$

where f_a is the Mössbauer fraction in the absorber, n_a the number of atoms per cubic centimeter of the element, d_a the thickness (cm) of the absorber, IA the isotopic abundance, and σ_0 the resonance cross section. The above equation can be expressed in more convenient terms by replacing n_a and d_a with the surface density σ_a expressed in mg/cm^2 of the element of interest. Therefore,

$$t_a = \frac{f_a \cdot N_0 \cdot IA \cdot \sigma_0}{1000 \cdot A_a} \tag{12}$$

where N_0 is Avogadro's number and A_a is the atomic weight for the absorber.

Now a more general expression can be given for the line shape resulting from the nuclear resonance for an absorber with uniform finite thickness as

$$I(E) = I_0 \left\{ 1 - f_s \left[1 - \frac{2}{\Gamma_s \Gamma_a} \int_{-\infty}^{+\infty} \frac{(\Gamma/2)^2}{(E - E_0)^2 + (\Gamma/2)^2} \right] \right.$$

$$\left. \times \exp\left[-t_a \frac{(\Gamma/2)^2}{E^2 + (\Gamma/2)^2} \right] dE \right\} \tag{13}$$

where f_s is the Mössbauer fraction for the source (26).

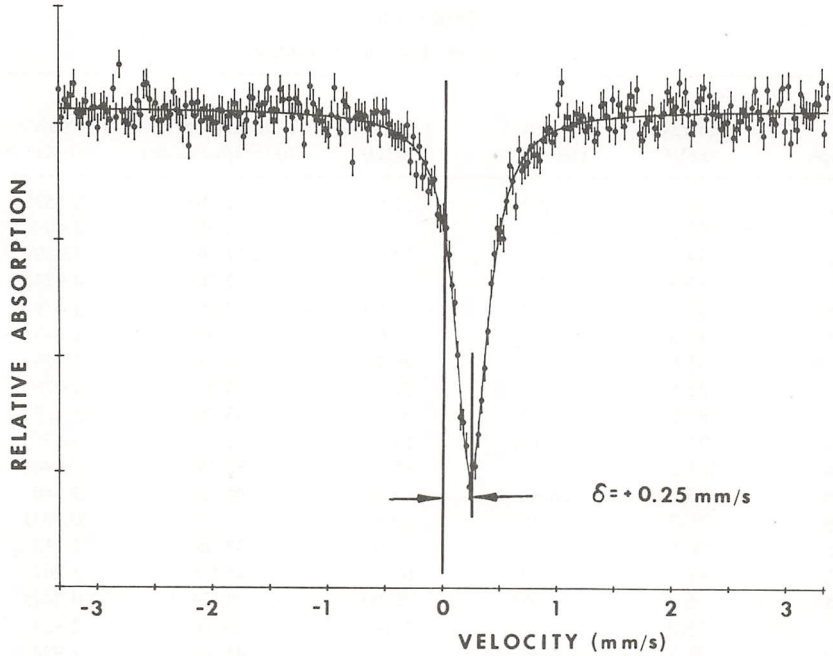

Fig. 6.5. ^{57}Fe Mössbauer spectrum of potassium ferrocyanide.

A Mössbauer spectrum of potassium ferrocyanide is shown in Fig. 6.5 in which the data points are fitted to a Lorentzian. Note that the energy axis is expressed in terms of velocity (mm/s). The reason for the choice of units has to do with the way in which the energy is varied to obtain the spectrum. The observable line widths are about one part in $10^{12}-10^{13}$ of the actual energy of the photon. Such resolution far exceeds any of the ordinary forms of spectroscopy and requires a unique method of varying the energy, one method of which utilizes the first-order Doppler shift (6). The absorber and source are moved relative to each other with velocity v resulting in a Doppler energy shift for the gamma ray of

$$\varepsilon = \frac{v}{c} E_\gamma \tag{14}$$

Conversions from the velocity units (mm/s) to several corresponding energy units are given in Table 6.II for a number of the more common transitions. Positive velocity refers to the case when the absorber and source are approaching each other. Methods for obtaining the velocities are discussed in the Experimental Methods section.

Observing nuclear gamma resonance is interesting, but the major usefulness comes as a result of the extremely high resolution that can be achieved. One of the main areas that can be investigated are nuclear hyperfine interactions. These are interactions between a property of the nucleus (e.g., magnetic dipole moment) and a feature of the environment of the nucleus (e.g., magnetic field). There are three such interactions that are extremely important to Mössbauer spectroscopy. These are the

TABLE 6.II
Energy Factors for Mössbauer Transitions

Isotope	Transition energy (keV)	1 mm/s = (10^{-8} eV)	1 mm/s = (MHz)	1 mm/s = (10^{-27} J/molecule)	1 mm/s = (mK)[a]
^{57}Fe	14.4	4.808	11.62	7.703	0.5579
^{61}Ni	67.4	22.48	54.37	36.02	2.609
^{99}Ru	89.4	29.81	72.07	47.76	3.459
^{119}Sn	23.9	7.963	19.25	12.76	0.9240
^{121}Sb	37.2	12.39	29.96	19.85	1.438
^{125}Te	35.5	11.83	28.60	18.95	1.373
^{127}I	57.6	19.21	46.46	30.78	2.230
^{129}I	27.8	9.263	22.40	14.84	1.075
^{133}Cs	81.0	27.02	65.33	43.29	3.135
^{151}Eu	21.5	7.182	17.37	11.51	0.8335
^{153}Eu	103.2	34.42	83.22	55.14	3.994
^{155}Gd	86.5	28.87	69.80	46.25	3.350
^{161}Dy	25.7	8.558	20.69	13.71	0.9931
^{166}Er	80.6	26.87	64.97	43.05	3.118
^{170}Yb	84.2	28.10	67.95	45.03	3.261
^{181}Ta	6.2	2.081	5.031	3.334	0.2415
^{193}Ir	73.0	24.36	58.91	39.03	2.827
^{197}Au	77.3	25.80	62.38	41.34	2.994
^{237}Np	59.5	19.86	48.02	31.82	2.305

[a] mK = milli Kelvin.

electric monopole interaction (E0), the magnetic dipole interaction (M1), and the electric quadrupole interaction (E2). We discuss these hyperfine interactions in the next section.

III. THE PRINCIPAL INTERACTIONS

A. ELECTRIC MONOPOLE (E0)—ISOMER SHIFT

An electrostatic interaction occurs between the nuclear charge of the nucleus and the atomic electrons that penetrate the nucleus. At the nucleus, the electronic charge density is given by $-e\left|\Psi(0)\right|^2$ and is approximately constant over the nuclear volume. Usually only the s electrons can penetrate the nucleus due to their wavefunction symmetries. The effect of this interaction is to raise the nuclear energy level slightly as shown in Fig. 6.6. Approximating the nucleus as a uniform sphere of radius R, one finds for this shift in energy

$$\delta E = \frac{2\pi}{5} Ze^2 \left|\Psi(0)\right|^2 R^2 \tag{15}$$

where Z is the nuclear charge. A net change in the energy of the transition (ΔE) will occur depending on the shifts for both the excited (δE_e) and ground (δE_g) levels, i.e.,

$$\Delta E = \delta E_e - \delta E_g = \frac{2\pi}{5} Ze^2 \left|\Psi(0)\right|^2 (R_e^2 - R_g^2) \tag{16}$$

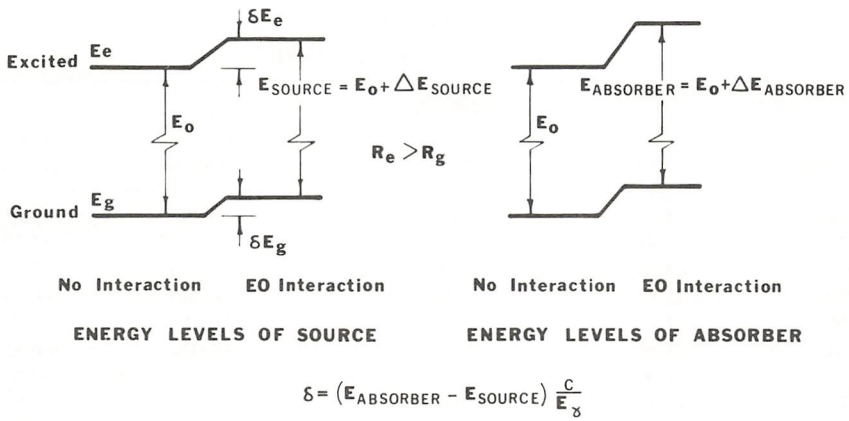

Fig. 6.6. Energy level diagrams for identifying the isomer shift.

This change in the transition energy will occur in both the source (emission) and the absorber (absorption). The difference between these in velocity units is called the isomer shift (δ) and can be measured as a shift in the absorption line as shown in Fig. 6.5. The expression for the isomer shift in velocity units using equation 16 becomes

$$\delta = [\Delta E_{\text{absorber}} - \Delta E_{\text{source}}]\frac{c}{E_\gamma}$$

$$= \frac{2\pi Ze^2c}{5E_\gamma}(R_e^2 - R_g^2)\,[|\Psi(0)|^2\,\text{absorber} - |\Psi(0)|^2\,\text{source}]$$

$$= \frac{4\pi Ze^2cR^2}{5E_\gamma}\left(\frac{\Delta R}{R}\right)[|\Psi_a(0)|^2 - |\Psi_s(0)|^2] \tag{17}$$

where $\Delta R = R_e - R_g$. The electron density terms in this equation are nonrelativistic; however, a relativistic model calculation (36) indicates that the only modification of equation 17 necessary is the addition of an overall factor $S(Z)$. Therefore

$$\delta = \frac{4\pi Ze^2cR^2}{5E_\gamma}S(Z)\frac{\Delta R}{R}[|\Psi_a(0)|^2 - |\Psi_s(0)|^2] \tag{18}$$

is the relativistic generalization of equation 17.

Equation 18 can be simply written as

$$\delta = \alpha\Delta|\Psi(0)|^2 \tag{19}$$

where α is called the isomer shift calibration constant and $\Delta|\Psi(0)|^2$ is the difference in electron densities at the nuclei in the two substances. Values for $\Delta R/R$, $S(Z)$, and α are given in Table 6.III. It is evident from these equations that the isomer shift is a function of the electron density at the nucleus. This electron density will be very much dependent on electronic structure of the Mössbauer atom and the bonding between this atom and its ligands. For α less than zero (e.g., ^{57}Fe), if iron compound

TABLE 6.III
Parameters for the Isomer Shift (34)

Isotope	E_γ (keV)	Relativistic correction $S(Z)$	α ($10^{-3}\ a_0^3$) (a_0 mm/s)[a]	$\Delta R/R$ (10^{-4})
^{57}Fe	14.41	1.294	−0.157	−5.6
^{61}Ni	67.41	1.343	−0.0085	−1.25
^{99}Ru	89.36	1.927	+0.060	+5.4
^{119}Sn	23.87	2.306	+0.042	+0.79
^{121}Sb	37.15	2.381	−0.21	−5.8
^{125}Te	35.46	2.438	+0.024	+0.62
^{127}I	57.60	2.530	−0.081	−3.3
^{129}I	27.77	2.530	+0.21	+4.2
^{133}Cs	81.00	2.685	+0.0156	+0.84
^{151}Eu	21.53	3.511	+0.34	+3.9
^{153}Eu	103.18	3.511	−0.40	−22
^{155}Gd	86.54	3.678	−0.025	−1.12
^{161}Dy	25.66	3.993	+0.115	+1.44
^{170}Yb	84.25	4.667	+0.0060	+0.22
^{181}Ta	6.24	5.196	−3.1	−7.8
^{193}Ir	73.04	6.213	+0.035	+0.95
^{197}Au	77.34	6.840	+0.053	+1.46
^{237}Np	59.54	13.580	−0.26	−4.1

[a] a_0 = Bohr radius.

A has a δ greater than that of iron compound B, then the electron density at nucleus B is greater than that at A.

Usually isomer shifts are given relative to the source used in the experiment or relative to a standard reference material. To compare literature data it is necessary to have all δ's relative to the same substance. Conversions relative to one material can be obtained relative to another by using the evaluated data given in Table 6.IV. This table also gives recommended standard reference materials. All δ data are usually reported relative to these materials.

B. MAGNETIC DIPOLE (M1)—MAGNETIC HYPERFINE SPLITTING

Energy levels in nuclei having spin quantum numbers (I) greater than zero will have a nonzero magnetic dipole moment ($\vec{\mu}$). In the presence of a magnetic field ($\vec{H}$), there will be an interaction that results in the splitting of nuclear energy levels removing degeneracies. The Hamiltonian describing this interaction is simply

$$\mathcal{H} = -\vec{\mu} \cdot \vec{H} \tag{20}$$

The magnetic moment can be expressed as

$$\vec{\mu} = g_N \beta_N \vec{I} \tag{21}$$

where g_N is the nuclear Landé factor (sometimes called the nuclear g factor) and β_N is

the nuclear magneton ($\beta_N = 5.051 \times 10^{-27}$ Joule/Tesla). Substituting equation 21 into equation 20 gives

$$\mathcal{H} = -g_N \beta_N \vec{I} \cdot \vec{H} \tag{22}$$

The diagonalization of the first-order perturbation matrix results in the following eigenvalues (E_M) for the Hamiltonian:

$$E_M(m_I) = -\mu H m_I / I = -g_N \beta_N H m_I \tag{23}$$

where m_I is the nuclear magnetic quantum number, having the $(2I+1)$ values: $-I$, $-I+1$, ... $I-1$, $+I$. As an example, the resulting splitting and transitions for ^{57}Fe are shown in Fig. 6.7. However, two of the transitions, $m_I = +3/2$ to $m_I = -1/2$ and $m_I = -3/2$ to $m_I = +1/2$, are forbidden since the selection rule is $\Delta m_I = 0$, ± 1. Spectra that result are often quite complex. In the spectrum for metallic iron, shown in Fig. 6.8, the magnetic field is an internal field of 33 Tesla.

As for the isomer shift, the term that is of most interest is the environmental parameter, in this case the magnetic field. This field can either exist internally or be applied. There are three principal contributions to the internal magnetic field, each being generated by unpaired electrons (45). Usually the dominant contribution is the Fermi contact field (H_c) which results from a spin density (either spin up or spin down) at the nucleus. These are the s-electrons that can be spin-polarized by the electrons in the outer shells. The other two fields are the orbital field (H_L), which results from the orbital motion of the valence electrons, and the dipolar field (H_D),

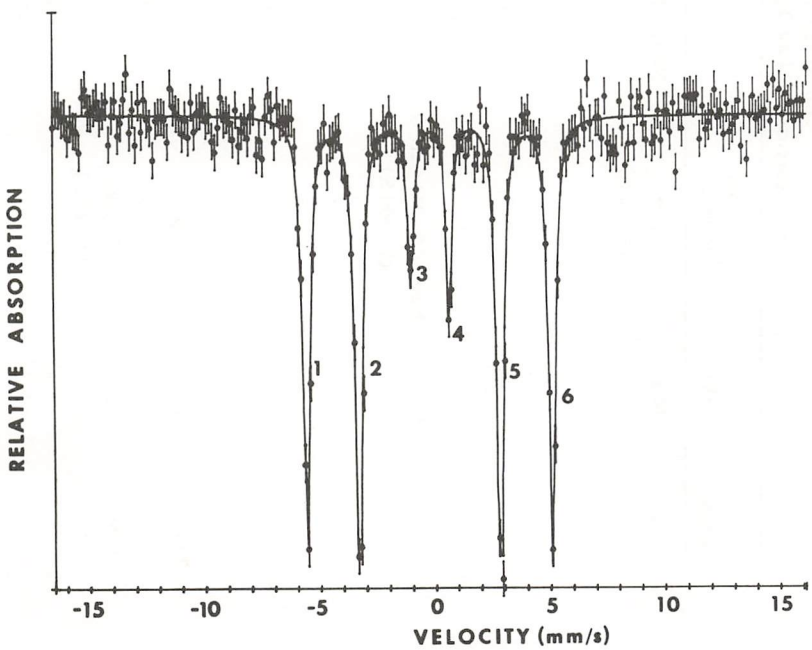

Fig. 6.7. ^{57}Fe Mössbauer spectrum of α-Fe.

TABLE 6.IV

Isomer Shift Reference Scales,
Uncertainty in Last Digit(s) Given in Parenthesis

Isotope	Transition (keV)	Reference material	Absorber and source materials (isomer shift relative to reference material in mm/s)		
^{57}Fe	14.4	α-Fe (T=300 K)	$Na_2Fe(CN)_5NO \cdot 2H_2O$ −0.2576(14)	Cr −0.146(3)	Stainless steel −0.086(3)
			$Na_4Fe(CN)_6 \cdot 10H_2O$ −0.0553(21)	$K_4Fe(CN)_6 \cdot 3H_2O$ −0.042(3)	Rh +0.1209(22)
			Pd +0.1798(12)	Cu +0.2242(10)	Pt +0.3484(24)
			α-Fe_2O_3 +0.365(3)		
		$Na_2Fe(CN)_5NO \cdot 2H_2O$ (T=300 K)	Cr +0.111(3)	Stainless steel +0.171(3)	$Na_4Fe(CN)_6 \cdot 10H_2O$ +0.2024(22)
			$K_4Fe(CN)_6 \cdot 3H_2O$ +0.2152(24)	α-Fe +0.2576(14)	Rh +0.3786(24)
			Pd +0.4374(13)	Cu +0.4819(13)	Pt +0.606(3)
			α-Fe_2O_3 +0.623(3)		
^{99}Ru	89.4	Ru	RuO_2 −0.249(8)	$K_4Ru(CN)_6 \cdot 3H_2O$ −0.224(10)	Ru(Rh) 0.000(4)
^{119}Sn	23.9	$BaSnO_3$ (T=77 K)	SnO_2 0.000	$CaSnO_3$ 0.000	Me_2SnF_2 +1.301(16)
			Pd(Sn) +1.505(13)	Pd_3Sn +1.571(14)	V(Sn) +1.577(6)
			Mg_2Sn +1.908(12)	α-Sn +1.998(15)	β-Sn +2.559(8)

			SnTe +3.446(15)		
		$BaSnO_3$ (T=300 K)	SnO_2 0.000	$CaSnO_3$ 0.000	Me_2SnF_2 +1.291(16)
			Pd(Sn) +1.507(13)	V(Sn) +1.624(14)	Pd_3Sn +1.579(7)
			Mg_2Sn +1.905(12)	α-Sn 1.995(15)	β-Sn +2.555(8)
			SnTe +3.441(15)		
^{121}Sb	37.2	InSb	β-Sn −2.70(4)	$Ni_{21}Sn_2B_6$ +1.648(19)	$BaSnO_3$ +8.47(4)
			SnO_2 +8.51(2)	$CaSnO_3$ +8.53(3)	
^{125}Te	35.5	ZnTe	β-TeO_3 −1.16(3)	PbTe +0.00(6)	Cu(I) +0.01(2)
			Rh(Sb) +0.05(10)	Cu(Sb) +0.08(3)	SnTe +0.23(5)
			Te +0.57(3)	TeO_2 +0.78(4)	
^{127}I	57.6	CuI	NaI −0.024(8)	KI −0.01(3)	CsI +0.00(3)
			ZnTe +0.12(2)		
^{129}I	27.8	CuI	NaI −0.076(18)	KI −0.062(14)	CsI +0.007(17)
			ZnTe +0.384(11)	SnTe +0.81(5)	
^{149}Sm	22.5	SmF_3	SmF_2 −0.90(8)	Eu −0.02(11)	Eu_2O_3 −0.01(6)

TABLE 6.IV (Cont.)
Isomer Shift Reference Scales,
Uncertainty in Last Digit(s) Given in Parenthesis

Isotope	Transition (keV)	Reference material	Absorber and source materials (isomer shift relative to reference material in mm/s)		
			EuF_3	Sm_2O_3	$SmAl_2$
			0.00(2)	+0.04(3)	+0.15(12)
^{151}Eu	21.5	EuF_3	EuS	$EuF_3 \cdot 2H_2O$	$SmF_3 \cdot 2H_2O$
			−11.65(4)	−0.046(9)	−0.003(13)
			SmF_3	Sm_2O_3	Eu_2O_3
			+0.05(3)	+0.85(4)	+1.017(8)
^{153}Eu	103.2	EuF_3	Eu_2O_3	Sm_2O_3	EuS
			−1.18(14)	−0.94(14)	+14.0(10)
^{155}Gd	86.5	GdF_3	Pd(Eu)	Gd	Sm(Eu)
			−0.684(9)	−0.678(9)	−0.53(4)
			EuF_2	$GdAl_2$	$SmAl_3$(Eu)
			−0.51(3)	−0.234(13)	−0.169(13)
			$GdAl_3$	$Sm_2Sn_2O_7$(Eu)	SmF_3(Eu)
			−0.159(12)	−0.12(2)	−0.02(4)
^{161}Dy	25.6	DyF_3	GdF_3(Tb)	Gd_2O_3(Tb)	Dy_2O_3
		(T=300 K)	+0.12(14)	+0.1(5)	+0.62(6)
			Gd(Tb)	Dy	
			+2.25(5)	+2.82(10)	
^{170}Yb	84.3	$YbAl_2$	$YbSO_4$	YbB_6	Yb
			−0.34(4)	−0.202(16)	0.00(2)
			TmB_{12}	$TmAl_2$	$YbAl_3$
			0.00(2)	+0.060(12)	+0.09(2)

			Tm +0.12(3)		
^{181}Ta	6.2	Ta	Mo(W) −22.56(8)	W −0.835(3)	Ta(W) −0.074(4)
			Pt(W) +2.71(8)		
^{193}Ir	73.0	Ir	Pt(Os) −0.644(6)	Os +0.539(7)	Nb(Os) +1.0(2)
			V(Os) +1.71(3)		
^{197}Au	77.3	Au	Pt +1.22(2)		
^{237}Np	59.5	$NpAl_2$	Th(Am) −8.9(3)	NpO_2 −6.10(4)	UO_2 −5.17(6)

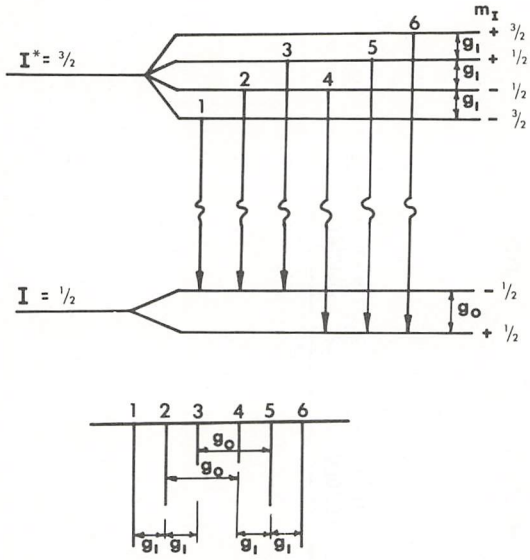

Fig. 6.8. Energy level diagram and line spectrum due to the magnetic hyperfine interaction in ^{57}Fe.

due to the coupling between the nucleus and outer electrons. Therefore, the total internal field is

$$H = H_C + H_L + H_D \tag{24}$$

C. ELECTRIC QUADRUPOLE (E2)—QUADRUPOLE COUPLING CONSTANT

When the nuclear-spin quantum number is greater than $\frac{1}{2}$ there is a nuclear quadrupole moment (Q). This moment can interact with the electric field gradient (EFG) to result in the splitting of nuclear energy levels. The EFG is $(-\vec{\nabla}\,\vec{\nabla}\,V)$, i.e.,

$$\text{EFG} = \vec{\nabla}\,\vec{E} = -\vec{\nabla}\,\vec{\nabla}\,V = \begin{bmatrix} V_{xx} & V_{xy} & V_{xz} \\ V_{yx} & V_{yy} & V_{yz} \\ V_{zx} & V_{zy} & V_{zz} \end{bmatrix} \tag{25}$$

where the components are given as

$$-V_{ij} = \frac{\partial^2 V}{\partial x_i \partial x_j}$$

The above symmetric tensor can be diagonalized by the appropriate choice of axes. The resulting tensor has three non-zero elements, which are the diagonal elements. Only two of these diagonal elements are independent due to Laplace's equation, which states

$$V_{xx} + V_{yy} + V_{zz} = 0$$

These two independent elements give rise to two experimentally observable parame-

ters. One of these is the z component of the electric field gradient defined as

$$q = \frac{V_{zz}}{e} \tag{26a}$$

while the other, the asymmetry parameter, is

$$\eta = \frac{V_{xx} - V_{yy}}{V_{zz}} \tag{26b}$$

where $|V_{zz}| \geqslant |V_{yy}| \geqslant |V_{xx}|$. This constraint restricts η to lie between 0 and 1.

The Hamiltonian for the interaction between the nuclear quadrupole moment and the EFG is

$$\mathcal{H}_Q = \frac{e^2Qq}{4I(2I-1)}[3I_z^2 - I^2 + \eta\,(I_+^2 + I_-^2)/2] \tag{27}$$

where I is the nuclear spin operator, I_z the operator for the nuclear spin projected in the z direction, and $I_\pm$ are shift operators. For cases of axial symmetry, i.e., $\eta = 0$, the energy eigenvalue equation is

$$E_Q = \frac{e^2Qq}{4I(2I-1)}[3m_I^2 - I(I+1)] \tag{28}$$

For the case where $I = 3/2$ (applicable to ^{119}Sn and ^{57}Fe) equation 27 becomes

$$E_Q(m_I) = \frac{e^2Qq}{12}\left[3m_I^2 - \frac{15}{4}\right][1 + \eta^2/3]^{1/2} \tag{29}$$

This gives two levels:

$$E_Q(\pm 1/2) = -1/4e^2Qq\,(1 + \eta^2/3)^{1/2}$$

$$E_Q(\pm 3/2) = +1/4e^2Qq\,(1 + \eta^2/3)^{1/2} \tag{30}$$

The resulting energy-level diagram for this interaction is shown in Fig. 6.9. Instead of a single absorption line there are two. The observed splitting of the single line into

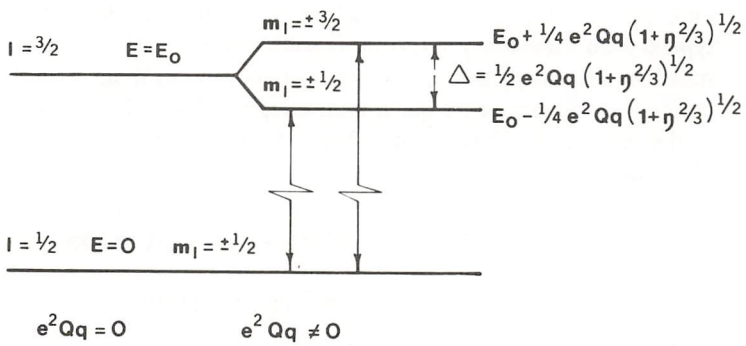

Fig. 6.9. Energy level diagram identifying the quadrupole splitting (Δ).

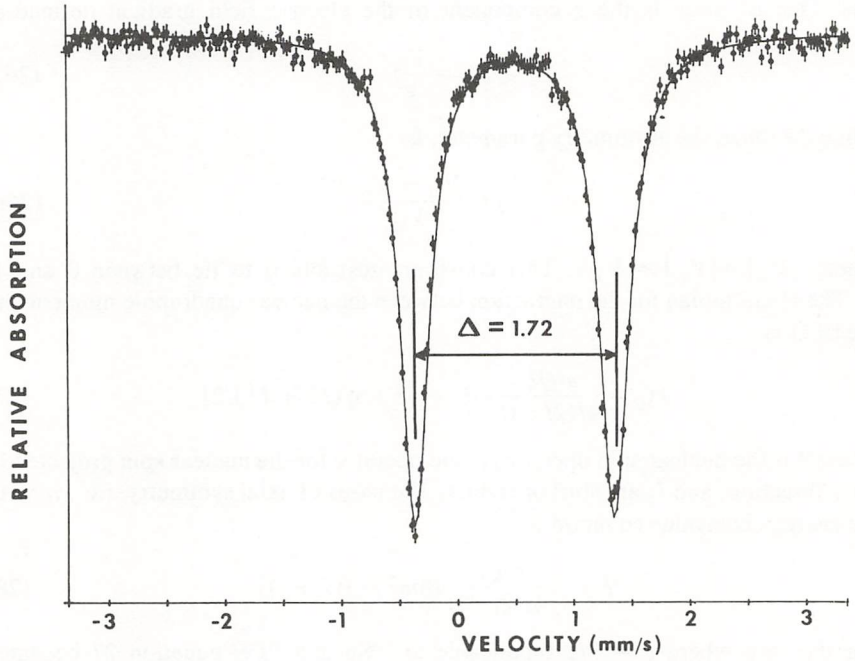

Fig. 6.10. ^{57}Fe Mössbauer spectrum of sodium nitroprusside.

two lines (see Fig. 6.10) is called the quadrupole splitting (Δ) and from equation 30

$$\Delta = 1/2e^2Qq\,(1 + \eta^2/3)^{1/2} \tag{31}$$

Often $\eta = 0$ and consequently the quadrupole splitting for a particular transition will be dependent only on V_{zz}.

When the nuclear spins are different from those of the common transitions in iron and tin, a much more complicated situation arises. For example, ^{121}Sb has a ground nuclear spin of 5/2 while the excited level is 7/2. If $\eta = 0$, there will be eight allowed transitions resulting in a more complex spectrum. It is unfortunate that for ^{121}Sb the eight absorption peaks overlap each other and none of the lines can be resolved. A typical ^{121}Sb Mössbauer spectrum is shown in Fig. 6.11. Because both the relative positions and intensities are known, it is not too difficult with the use of a digital computer to determine the quadrupole coupling. More details on this will be provided in the sections on Experimental Methods, (Section IV) and Quadrupole Coupling (Section VII).

IV. EXPERIMENTAL METHODS

A. SPECTROMETERS

A Mössbauer spectrum is a plot of intensity (of gamma rays) versus Doppler velocity. While gamma rays are detected and counted by using normal nuclear-counting instrumentation methods, velocity-modulation techniques are relatively

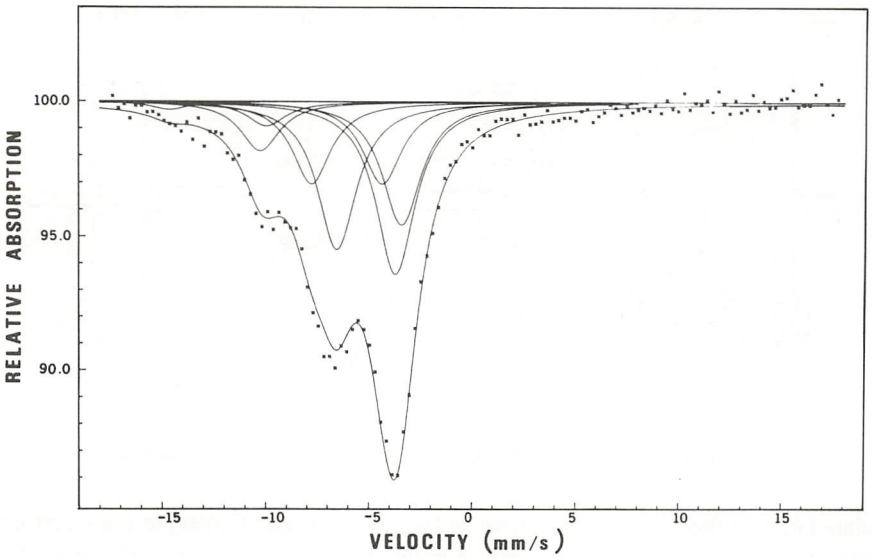

Fig. 6.11. ^{121}Sb Mössbauer spectrum of $PhSb(Et_2dtc)_2$.

unique to Mössbauer spectroscopy and are central to any Mössbauer spectrometer. Many of the earlier spectrometers were mechanical devices in which the source or absorber moved at a constant velocity relative to one another. With these devices, the spectrum is obtained by counting for a specific period of time at one velocity, recording the number of gammas counted, and then selecting another velocity, etc. Such a procedure is obviously very time-consuming and requires much effort. Programming techniques can be used to reduce some of this effort. However, current spectrometers use electromechanical devices which sweep a range of velocities with a frequency of the order of 10 Hz. This allows the complete range of velocities (i.e., energies) to be counted almost simultaneously, although a spectrum does not begin to appear until after many scans.

The primary element of a Mössbauer spectrometer is an electromagnetic transducer, often referred to as the Kankeleit drive. This has one basic design consisting of a drive coil, which is located in the field of a permanent cylindrical magnet, and a velocity-monitoring coil, both of which are attached to a center rod. The coils can be either specifically designed for the spectrometer or obtained from a commercially produced loudspeaker. A cross-section diagram of a drive is shown in Fig. 6.12.

The rod is driven by a current running through the drive coil. The current can be varied to produce several different periodic motions, shown in Fig. 6.13. The triangle, which is the most common waveform, and the sawtooth, sometimes called "flyback," both give velocities which vary linearly in time. The triangular waveform gives a true spectrum along with its mirror image. The sawtooth does not give a mirror spectrum. The sinusoidal waveform is especially suited for large velocities and fine precision.

A schematic block diagram of a typical Mössbauer spectrometer is shown in Fig. 6.14. It illustrates how the electromagnetic transducer, discussed above, is

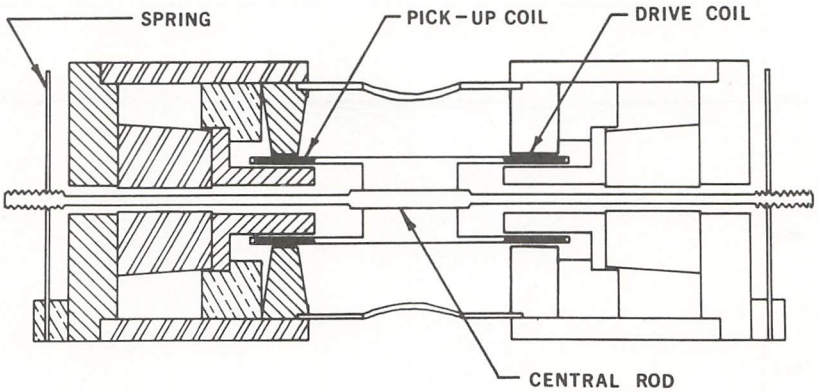

Fig. 6.12. Mössbauer drive motor (courtesy of Austin Science Associates).

related to the other major components of the spectrometer. Central to the electronic part of a Mössbauer spectrometer is a multichannel analyzer (MCA), an on-line computer system, or a microprocessor which stores the collected data in the form of the number of gammas counted at each velocity.

B. SOURCES

The usual sources are radioactive isotopes that first decay by electron capture or alpha, beta, or gamma ray emission. These radioactive isotopes subsequently undergo Mössbauer transitions. Simplified nuclear energy level diagrams illustrating typical decays are given in Fig. 6.15 for four typical Mössbauer transitions. It is

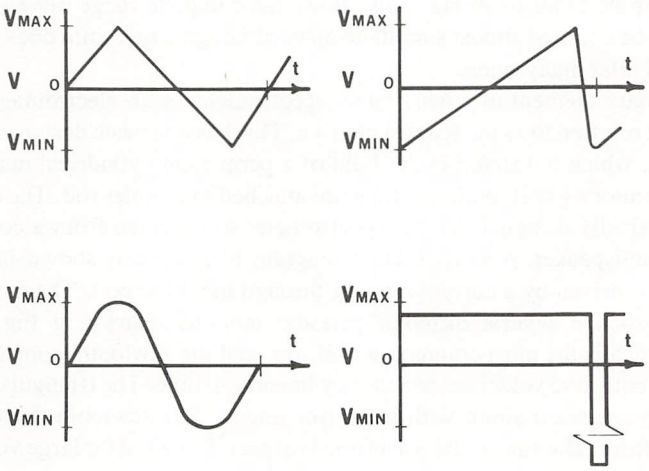

Fig. 6.13. Periodic motions of a Mössbauer spectrometer (triangle, sawtooth, sinusoidal, and flyback).

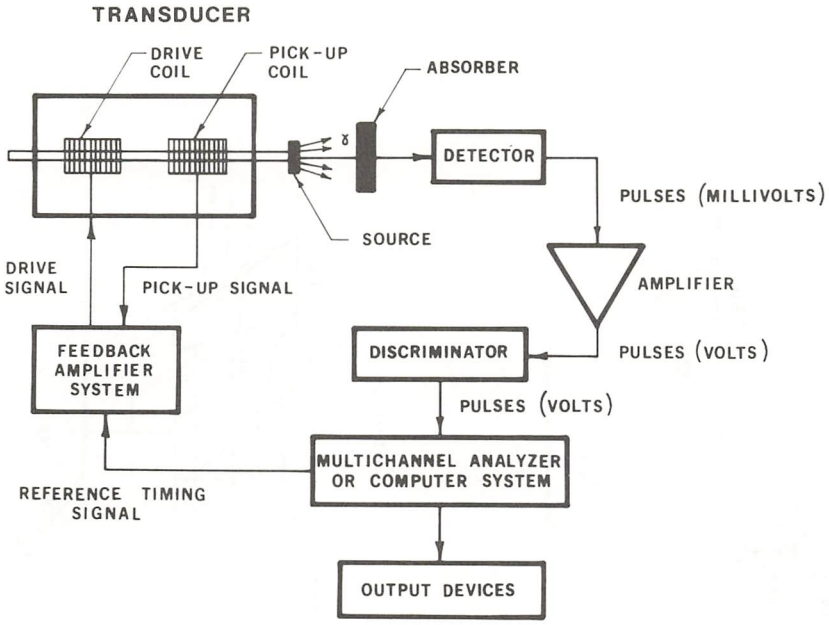

Fig. 6.14. Block diagram of a Mössbauer spectrometer.

desirable for the gamma ray to be emitted with zero recoil during the Mössbauer transition. From equations 8 and 10, it is apparent that the Mössbauer fraction, which gives the probability for a recoilless emission, is significant provided that the energy of the gamma is not too large. In fact, all the observable Mössbauer transitions have gamma energies below 200 keV. See Table 6.I for the energies of the more common transitions.

The lifetimes of any excited nuclear level used in Mössbauer spectroscopy must have natural line widths (see equation 5) that can be observed by the Doppler velocity-scan method of varying the energy. Consequently these lifetimes are usually in the range of 1 – 100 ns. If they are shorter, the line width will be too broad and, if longer, the line width will normally be too narrow to be observed. It is important to select source materials that give a large Mössbauer fraction (f_s) and have single, narrow lines. Table 6.V contains a list of such materials with f_s values at those temperatures normally used for the spectroscopy.

C. DETECTORS

Since Mössbauer gamma rays are quite low in energy, the detectors employed are those that normally detect X-rays. Basically there are three different types of detectors. These are the scintillation detectors, the proportional counters and the semiconductor devices. Scintillation detectors are usually NaI(Tl) crystals and are excellent for the higher-energy Mössbauer transitions due to their counting efficiency.

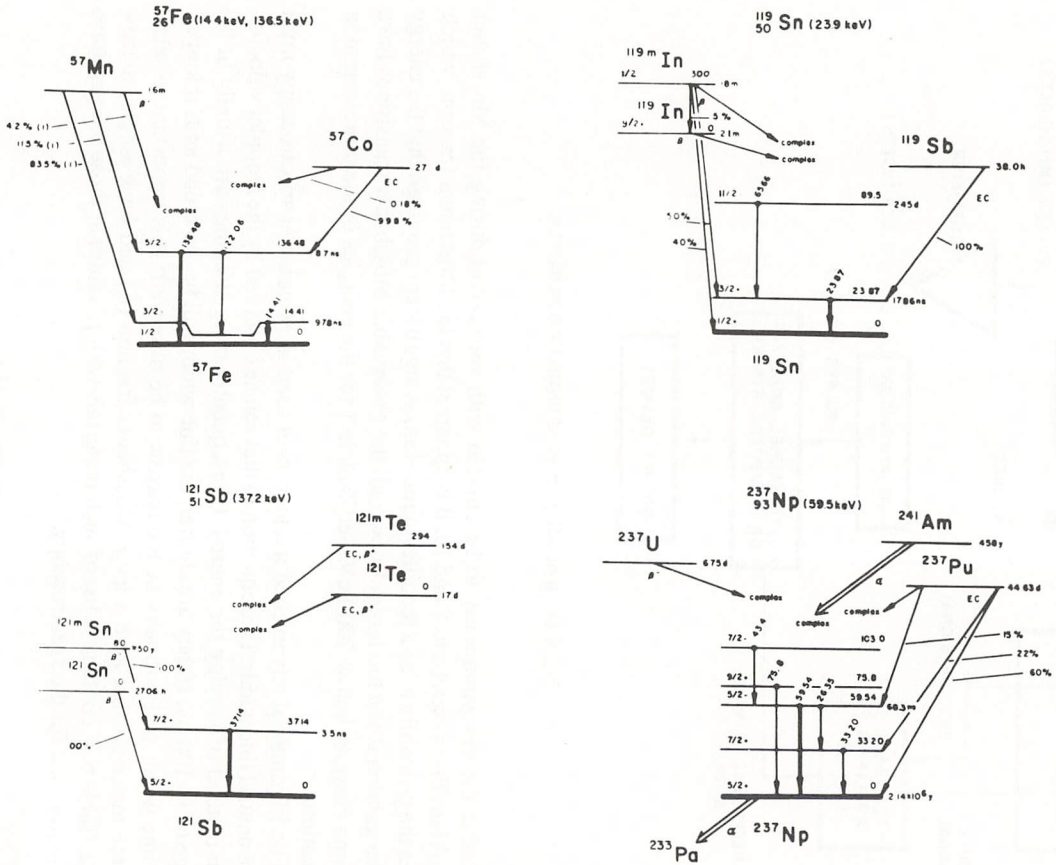

Fig. 6.15. Simplified nuclear energy level diagrams for ^{57}Fe, ^{119}Sn, ^{121}Sb and ^{237}Np.

They are also relatively inexpensive, but have poor resolution. This makes them inappropriate for many transitions. Proportional counters, also inexpensive, have resolutions that are much improved over the scintillation detectors, but have poor efficiency at the higher energies. The semiconductor detectors are usually Ge(Li) or Si(Li). More recently intrinsic Ge detectors have been employed. The efficiency is excellent for these devices at all gamma energies of interest and they have resolutions that are even better than proportional detectors. An example of their improvement in resolution can be seen in Fig. 6.16 where a comparison is made with results obtained from a proportional detector. However, their cost ranges from $5,000 to $15,000. In addition, they must be maintained at liquid nitrogen temperatures.

TABLE 6.V

Properties of Mössbauer Sources (37)

Isotope	Transition energy (keV)	$W_o{}^a$ (mm/s)	Source material	Source temperature (K)	f_s
^{57}Fe	14.41	0.194	Cr	300	0.784
			SS310	300	0.604
			SS	300	0.678
			Rh	300	0.784
				4.2	0.875
			Pd	300	0.660
				77	0.863
				4.2	0.813
			Cu	300	0.708
				4.2	0.910
			Pt	300	0.724
				77	0.890
				4.2	0.851
			CoO	300	0.735
^{61}Ni	67.41	0.770	Ni–Cr alloy	4.2	
			Ni–V alloy	4.2	0.162
^{99}Ru	89.36	0.149	Ru(Rh)	4.2	0.140
^{119}Sn	23.87	0.646	SnO_2	300	0.471
				77	0.585
				4.2	0.885
			$CaSnO_3$	300	0.574
			$BaSnO_3$	300	0.623
			Pd(Sn)	300	0.383
			Pd_3Sn	300	0.340
				4.2	0.750
			V(Sn)	300	0.460
				77	0.780
			Mg_2Sn	300	0.280
				77	0.770
			α-Sn	77	
			β-Sn	300	0.046
				77	0.446
				4.2	0.716

TABLE 6.V (Cont.)
Properties of Mössbauer Sources (37)

Isotope	Transition energy (keV)	W_o[a] (mm/s)	Source material	Source temperature (K)	f_s
^{121}Sb	37.15	2.10	SnO_2	300	0.212
				77	0.320
			$BaSnO_3$	77	0.450
			β-Sn	77	0.160
			$Ni_{21}Sn_2B_6$	300	0.070
				77	0.290
^{125}Te	35.46	5.209	β-TeO_3	300	0.320
				77	0.531
			PbTe	300	<0.029
				77	0.250
			Cu(I)	77	0.143
				4.2	0.400
			Rh(Sb)	4.2–77	
			Cu(Sb)	300	<0.029
				77	0.442
^{127}I	57.60	2.49	ZnTe	4.2	0.120
^{129}I	27.77	0.586	ZnTe	77	0.232
^{151}Eu	21.53	1.31	SmF_3	300	0.275
			$SmF_3 \cdot 2H_2O$	300	
			Sm_2O_3	300	0.440
^{153}Eu	103.2	0.68	Sm_2O_3	20	0.050
^{155}Gd	86.55	0.499	Pd(Eu)	4.2	0.110
			Sm(Eu)	4.2	
			$Sm_2Sn_2O_7$	4.2	
^{161}Dy	26.66	0.378	Gd_2O_3	300	0.230
			GdF_3	300	
			Gd(Tb)	300	
^{166}Er	80.56	1.816	$HoAl_2$	25–30	
^{170}Yb	84.25	2.019	TmB_{12}	4.2	0.340
			$TmAl_2$	4.2	0.180
			Tm	4.2	
^{181}Ta	6.24	0.0064	Mo(W)	300	
			W	300	
			Ta(W)	300	
			Pt(W)	300	
^{193}Ir	73.04	0.595	Pt(Os)	4.2	
			Os	4.2	
			Nb(Os)	4.2	
			V(Os)	4.2	
^{197}Au	77.35	1.882	Pt	77	0.069
				4.2	0.272
^{237}Np	59.54	0.067	Th(Am)	4.2–77	
			VO_2	4.2–77	

[a] Natural line width in units of mm/s.

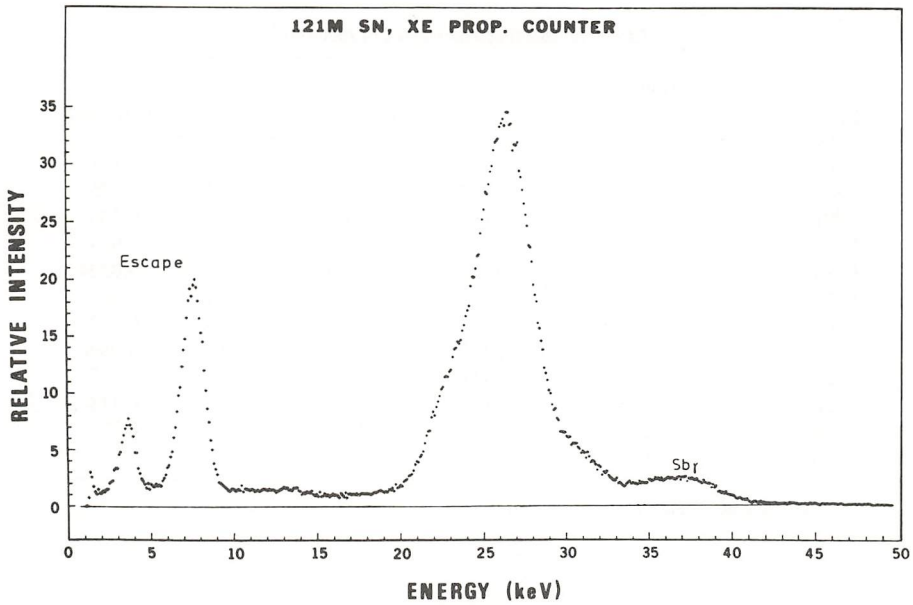

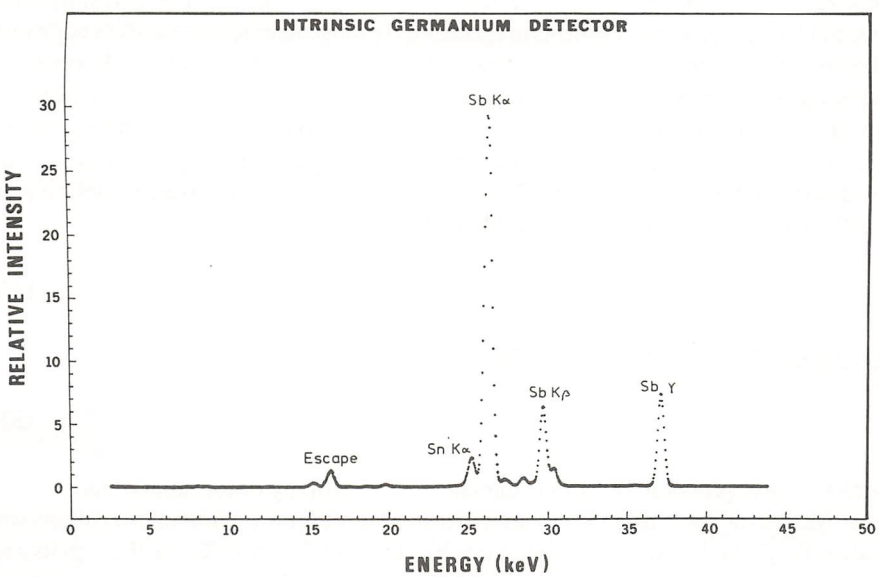

Fig. 6.16. Comparison of the emission spectra using a $Xe(CH_4)$ proportion detector and an intrinsic germanium detector.

TABLE 6.VI
Effective Absorber Thickness Constant (40)

Isotope	Transition (keV)	t_e (cm^2/mg)	Isotope	Transition (keV)	t_e (cm^2/mg)
^{57}Fe	14.4	0.578	^{155}Gd	86.5	0.194
^{61}Ni	67.4	0.0836	^{161}Dy	43.8	0.225
^{99}Ru	89.4	0.0622	^{166}Er	80.6	0.288
^{119}Sn	23.9	0.609	^{169}Tm	8.4	0.918
^{121}Sb	37.1	0.557	^{170}Yb	3.0	0.0204
^{125}Te	35.5	0.0895	^{181}Ta	6.2	5.56
^{127}I	57.6	0.975	^{182}W	100.1	0.219
$^{129}I^a$	27.8	1.82	^{193}Ir	73.0	0.0598
^{133}Cs	81.0	0.466	^{195}Pt	98.8	0.0637
^{149}Sm	22.5	0.0397	^{197}Au	77.3	0.118
^{151}Eu	21.5	0.453	$^{237}Np^a$	59.5	0.778
^{153}Eu	83.4	0.200			

[a] Isotopic abundance assumed to be one.

D. ABSORBERS

Special care needs to be taken in preparing an absorber with particular attention given to optimizing the thickness. A sample too thin will result in little observable absorption while one too thick will absorb most of the gammas nonresonantly, thus washing out the resonant absorption spectrum. In most other spectroscopies adjusting the thickness by trial and error is usually the most efficient procedure. However, in Mössbauer spectroscopy it often takes hours (and sometimes even days) to obtain a spectrum. Therefore it is important, if at all possible, to prepare the sample correctly on the first attempt. The thickness of the sample needed to give a good spectrum can be determined by using equation 12. This expression can be simplified by defining an "effective absorber thickness constant" (t_e) as

$$t_e = \frac{N_0 \cdot IA \cdot \sigma_0}{1000 \cdot A_a} \tag{32}$$

Using equation 32 with equation 12 we find

$$\sigma_a = \frac{t_a}{f_a \cdot t_e} \tag{33}$$

which is an expression for sample thickness in units of mg of the atom of interest per cm^2. Values for the constant t_e are given in Table 6.VI for the common transitions and values for f_a can be estimated using plots like those in Fig. 6.4. To use these plots one must assume an approximate Debye temperature for the material. Usually organic substances are 50–150K, inorganic substances 100–300 K, and metals and alloys 200–300 K. The Debye temperature is related to the strength of the bonds between the atom of interest and its neighbors. For selecting the sample thickness, a rough

value of θ_D will suffice. Using equation 33 and letting $t_a = 1$, an appropriate sample thickness can be determined. If a spectrum is expected to consist of more than a single line, then one should use a larger value for t_a up to five, depending on the anticipated complexity. Some values of sample thicknesses using $t_a = 1$ are listed in Table 6.VII.

It is quite important to have a sample that is approximately uniform in thickness. This is quite difficult to achieve when the sample needs to be as thin as indicated for some cases in the table. The usual procedure is to mix the material with a filler substance that is relatively transparent to the gamma ray. These substances should have atoms of low atomic weights (low Z) and be nonreactive with the sample. Examples are fine powders of boron nitride, sugar, polymethylmethacrylate and glass.

The absorber is placed in a container also made of a low Z material. Common materials include Plexiglass, beryllium, aluminum, and Teflon. If the absorber material is a metal, then it can be rolled into a thin foil.

It is important to maximize the count rate by minimizing the source detector distance. However, at some point minimizing can begin to add a serious error in the velocity scale. This is often referred to as the "cosine effect" because the error in the Doppler energy (ΔE) is

$$\Delta E = \frac{\mathrm{v}}{c} E_\gamma \cos\theta \tag{34}$$

where θ is the angle between the direction of the photon and the normal direction between the source and the absorber. As a general rule, it is desirable that the ratio between the detector-window radius and the source-detector distance be less (assuming the source radius is equal to the window radius) than 0.1. Sometimes when a particular source may be quite weak, closer distances are necessary to get any sort of spectrum in a reasonable amount of time.

E. TEMPERATURE CONSIDERATIONS

An examination of the plots in Fig. 6.4 reveal the importance of temperature in obtaining observable spectra. For most Mössbauer transitions, it is necessary that the experiment be done at low temperature, often down to 4.2 K, which can be achieved using liquid helium. Some spectra can be obtained using liquid nitrogen for cooling (77 K). Commercial Dewars readily available which are not already suitable can be easily modified for Mössbauer spectroscopy. The Dewars are constructed either from stainless steel or glass, the latter being less expensive but more easily broken.

Many different absorber-source-detector geometries and configurations are possible. The most common has the absorber and the source at the same temperature inside the cryostat, and the detector outside. Mylar windows (usually aluminum coated) are most commonly used to minimize the nonresonant absorption of the gammas.

Often it is quite important to gather Mössbauer data as a function of temperature. These can be obtained using feedback heating devices that give temperatures from 4.2 K to well above room temperature. For higher temperatures, specially con-

TABLE 6.VII

Calculated Values of Absorber Thickness (σ_a) in mg/cm^2 of the Natural Isotopic Abundance (2)

		$S(\theta_D = 100\ \mathrm{K})$			$S(\theta_D = 150\ \mathrm{K})$			$S(\theta_D = 200\ \mathrm{K})$			$S(\theta_D = 250\ \mathrm{K})$		
Isotope	Transition (keV)	300	77	4.2	300	77	4.2	300	77	4.2	300	77	4.2
^{57}Fe	14.4	261	11	5	24	5.9	4.4	10.3	4.8	4.1	7	4.3	4
^{61}Ni	67.4			40268			3281		18483	951		2341	454
^{99}Ru	89.4						6635			1735		4604	776
^{119}Sn	23.8	965	15	5.3	41	6.7	4.5	14	5	4.2	8.3	4.4	4
^{121}Sb	37.1		129	11	1447	19	7.3	105	9.5	6.1	31	7	5.4
^{125}Te	35.5		546	61		100	43	455	55	37	156	41	33
^{127}I	57.6			28		100	11		21	7.5	317	10	5.8
^{129}I	27.8		7.3	2	26	2.7	1.6	6.6	1.9	1.5	3.5	1.6	1.4
^{133}Cs	80.9			575			110		343	48		87	30
^{151}Eu	21.5	169	12	6	22	7	5.4	11	5.8	5.1	8	5.3	5
^{153}Eu	103						1765		8878	555		1288	278
^{155}Gd	86.5			1317			259		795	116		208	72
^{161}Dy	25.6	380[a]	11[a]	4.5[a]	26[a]	5.5[a]	3.9[a]	10[a]	4.3[a]	3.6[a]	6.5[a]	3.8[a]	3.5[a]
^{170}Yb	84.2			5014			1230		3240	614		1017	406
^{193}Ir	73			527		2040	208		395	131		183	100
^{197}Au	77.3			351		1552	126		255	76		110	56
^{237}Np	59.5		298[a]	11.4[a]	7084[a]	24[a]	6.9[a]	227[a]	9.8[a]	5.4[a]	46[a]	6.5[a]	4.6[a]

[a] Should be multiplied by a factor of 10 because of line broadening.

structed vacuum chambers are used. They are constructed with materials that are nonreactive with the sample at temperatures as high as 2000 K. On the other end of the temperature scale it is possible to carry out Mössbauer experiments well below 4.2 K (to the order of 10^{-4}) by using $^3He-^4He$ dilution refrigerators, now commercially available. More details of these cooling and heating devices are described in several good review articles (6,12,22).

F. APPLIED MAGNETIC FIELDS

The common types of electromagnets are usually not adequate for use in Mössbauer spectroscopy because they produce fields that are too small to resolve any interesting information. Most of the studies use superconducting solenoids capable of giving fields as high as 10 Tesla. These magnetic devices are constructed inside the Dewar to give large fields parallel (longitudinal) and perpendicular (transverse) to the source-absorber direction. These magnets are commercially available for Mössbauer spectroscopy.

G. VELOCITY CALIBRATION

Calibrating the energy function of a Mössbauer spectrometer is a nontrivial procedure. In most instances one of two types of procedures is used. The simplest and most common is the use of standard reference materials whose Mössbauer spectra have peaks that are well defined in velocity units. The other method is an optical one which uses either a Michelson interferometer or a Moiré fringe device.

Several standard calibration references are available. The most common reference is the ^{57}Fe Mössbauer spectrum of α-Fe. The splittings for various materials are given in Fig. 6.17. The α-Fe has several advantages, including multiple peaks that not only allow for the determination of the velocity calibration scale constant, but also enable a check of the linearity of the spectrometer. Sodium nitroprusside ($Na_2Fe(CN)_5NO \cdot 2H_2O$) is another common material but no check can be made on the linearity because there are only two peaks. This is usually employed when the velocity scale is small in a particular experiment, i.e., a maximum velocity of less than 3 mm/s. Although both of these materials are the most widely used, there are several other substances that are used. These give multiple line spectra for larger velocity scales than those for which α-Fe is suitable. α-Fe_2O_3 can be employed, but care must be taken because of the possibility of other phases. To achieve lines at larger velocities one can use a source of ^{57}Co in α-Fe and an α-Fe absorber, which will give lines over a range of velocities of 20 mm/s. Finally the largest practical splitting currently used is the ^{161}Dy Mössbauer spectrum of Dy metal, which gives peaks over a range of velocities exceeding 400 mm/s.

Recently two optical devices for calibration have been gaining wide support (9,13,14). These are now available on most commercial spectrometers and are more precise than the reference calibration discussed above. Both optical devices can use either a lamp or a laser, but the latter is preferred.

With a Michelson interferometer, one can measure distance and time very precisely to determine velocity. There are two basic mirrors: one is fixed and the other

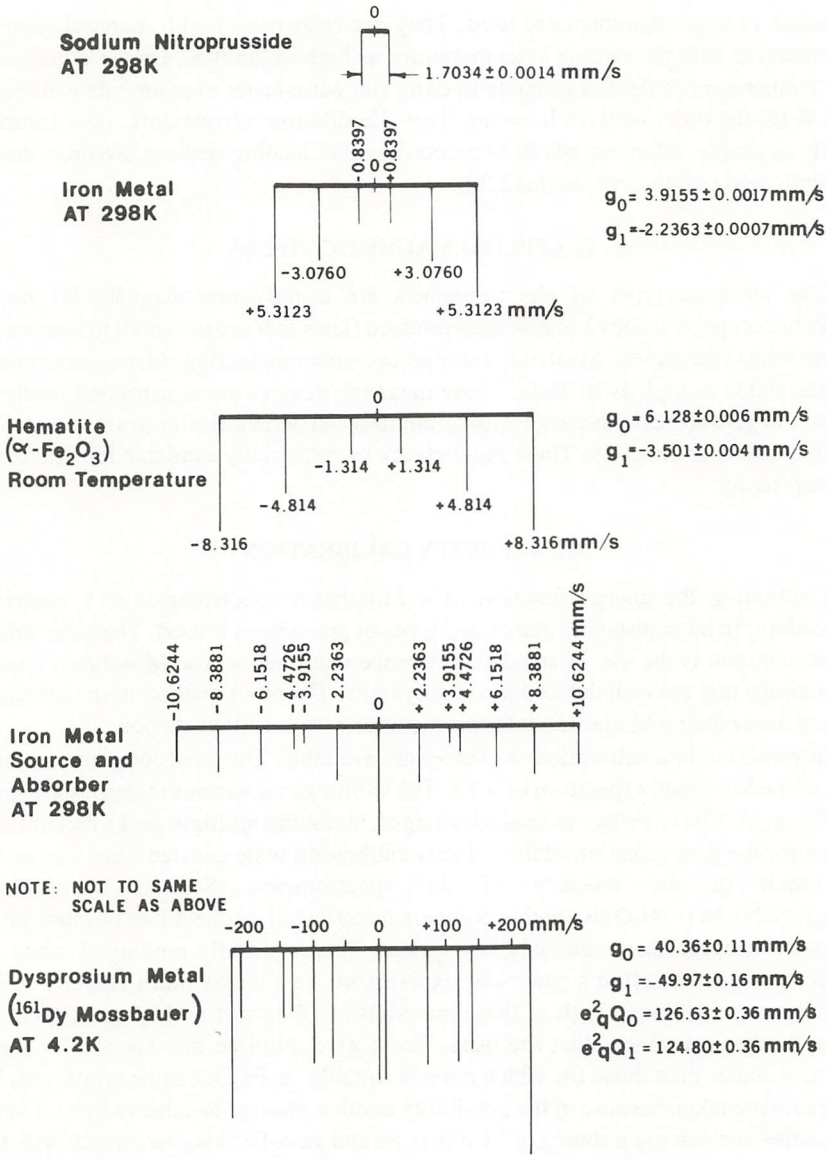

Fig. 6.17. Standard splittings for Mössbauer velocity calibrations.

is connected to the moving rod of the transducer. The intensity of light detected at the photodiode depends on the position (x) of the moving mirror (see Fig. 6.18), such that

$$I \sim \sin \frac{2\pi x}{\lambda/2} \tag{35}$$

where λ is the wavelength of the laser. When the mirror moves $\lambda/4$, the intensity of the laser beam at the photodiode will change from a maximum to zero. The photodiode is used to count the number (n_i) of the times there is a change from dark to bright to dark. The calibration of a particular velocity channel is achieved using the following relation for the average velocity:

$$\bar{v}_i = \frac{n_i \lambda}{2N\Delta t_i} \tag{36}$$

where Δt_i is the time spent in the channel and N is the number of times the channel has been opened for counting.

Similar is the Moiré fringe method, which is also shown in Fig. 6.18. The average velocity of the i channel is given by

$$\bar{v}_i = \frac{n_i d}{4N\Delta t_i} \tag{37}$$

where d is the grating distance. The Moiré method does not require the sometimes difficult aligning and focusing necessary when the interferometer is used, but it is an order of magnitude less precise. The interferometer gives a "direct measurement," while the Moiré method requires a knowledge of the spacing between lines in the grating. However, an advantage of the Moiré devices is their compactness.

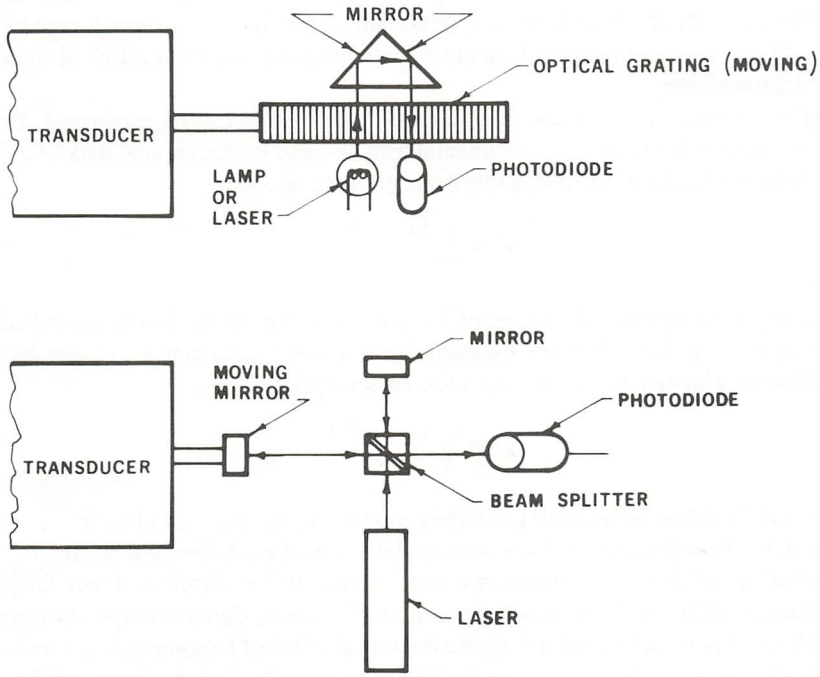

Fig. 6.18. Schematic diagram for a Moiré fringe device (upper diagram) and a Michelson interferometer (lower diagram).

H. CURVE FITTING

Mössbauer spectra are collected and stored in the form of digital data. This allows spectra to be examined very carefully, usually by attempting to fit the data to a theoretical model. The most important data frequently are the positions of each of the spectral lines. In fitting the data to the model, it is normally important to know the intensity and the line width of each absorption peak. As discussed earlier, the shape of absorption peaks for zero-thickness absorbers is Lorentzian. Even though samples are of finite thickness, the Lorentzian shape is a good approximation and can be treated with computers quite easily. A more general line shape is the "transmission integral" but the computer time necessary for the fitting is long and prohibitively expensive. However, when there are two or more Lorentzians overlapping, serious consideration must be given to using a transmission integral fit as opposed to a simple sum of Lorentzians.

Most of the computer programs used contain subroutines that perform least-square fits for the data. Before this is done, a certain amount of preprocessing of the data is required. The digital data is in the form of channel numbers (representing velocity) versus counts (representing intensity). If the spectrometer is not linear in velocity, velocity values are assigned to each data point using the data obtained by one of the calibration techniques described earlier. If a transmission integral fit is desired for the least squares, then the velocity scales must be adjusted to allow for a constant velocity increment between data points. If the asymmetric velocity waveform is used, then the spectrum can also be folded since the first half of the data is a mirror image of the second half. This procedure will remove some of the unwanted features of the data due to the geometry.

After the preprocessing, the least-squares computation can be performed. Comparison is made between the experimental data (Y_i) and the theoretical data (A_i) for a particular model. In particular, a function (χ^2) is minimized:

$$\chi^2 = \sum_i \frac{(Y_i - A_i)^2}{\sigma_i^2} \tag{38}$$

where σ_i is the standard deviation of Y_i. Since nuclear decay data is described by Poisson statistics, i.e., the standard deviation is nothing more than the square root of counts in the channel of interest, equation 38 becomes

$$\chi^2 = \sum_i \frac{(Y_i - A_i)^2}{Y_i} \tag{39}$$

Care must be taken in proposing a certain model and getting a good fit for the data, since it is often possible to have two models give almost identical values for χ^2.

Some laboratories do not perform a least-squares fit but merely estimate the peak positions, widths, and intensity from a plot. However, digital computation gives experimental parameters that are approximately an order of magnitude more accurate and precise. The data from a storage device can be outputted by one of several devices such as *x-y* plotters, strip chart recorders, paper computer tapes, oscilloscopes, teletypes, and even on-line devices.

V. ISOMER SHIFT AND ITS APPLICATION

The basic interaction which results in the isomer shift (δ) has already been described in Section III. The isomer shift can be used to measure electron densities at the nucleus although primarily one measures changes in it when going from one state to another (e.g., changes in the chemical species, the physical phases, or reference frames). Of the various Mössbauer parameters, δ is certainly the most unique since the information it provides cannot easily be obtained by other means. The first report of δ data was made in 1960 by Kistner and Sunyar (23). Since then there has been a voluminous amount of experimental and theoretical work reported in the literature. One of the major contributions has been an entire book on the subject (35). This approximately 1000-page volume covers a comprehensive range of topics discussed by leading Mössbauer spectroscopists.

For chemists and solid-state physicists the isomer shift can be correlated to a number of factors. These include the number of ligands, the geometric arrangement of the ligands about the Mössbauer nucleus, the electronegativity of the ligands, the bonding characteristics between the Mössbauer atom and the ligands, and the electronic state of the Mössbauer atom. Most fruitful Mössbauer isomer shift data is obtained when a series is considered in which all variables are held constant except one.

Most of the δ data is interpreted in the context of empirical relations, i.e., the isomer shift is correlated either with those factors mentioned above or with data from other experimental methods (e.g., NMR, IR, ESCA, and powder X-ray diffraction). Theoretical development has been gradual but shows promise as quantum methods are continuously being refined.

A. ELECTRON DENSITY CALCULATIONS

Since the isomer shift is a measurement of electron density in the vicinity of the nucleus, quantum determinations in the form of $\Psi^2(r = 0)$ have offered much insight into those species studied. For example, various self-consistent field (SCF) calculations have been used. In these calculations the Mössbauer atom is treated independently of any ligands, i.e., as a free ion. One of the first treatments was the Hartree-Fock calculations for iron by Walker, Wertheim, and Jaccarino (43). Their results are given in Fig. 6.19. This plot can be used to interpret isomer shifts of ionic materials. Similar calculations have been done for a number of other Mössbauer atoms. As an example, the results for antimony are shown in Fig. 6.20 (32). In both of these figures of plots of electron density versus electronic configuration, the isomer-shift scale has been superimposed.

While the SCF results are instructional in understanding factors that affect the isomer shift, they neglect covalency. This can be incorporated into the model by using some type of molecular orbital (MO) method, which usually considers only the valence atomic orbitals. Specifically, molecular orbitals are assumed to be made up of a linear combination of atomic orbitals (LCAO), i.e.,

$$\Psi_{\mathrm{MO}} = a_M\phi_M + a_L\phi_L \tag{40}$$

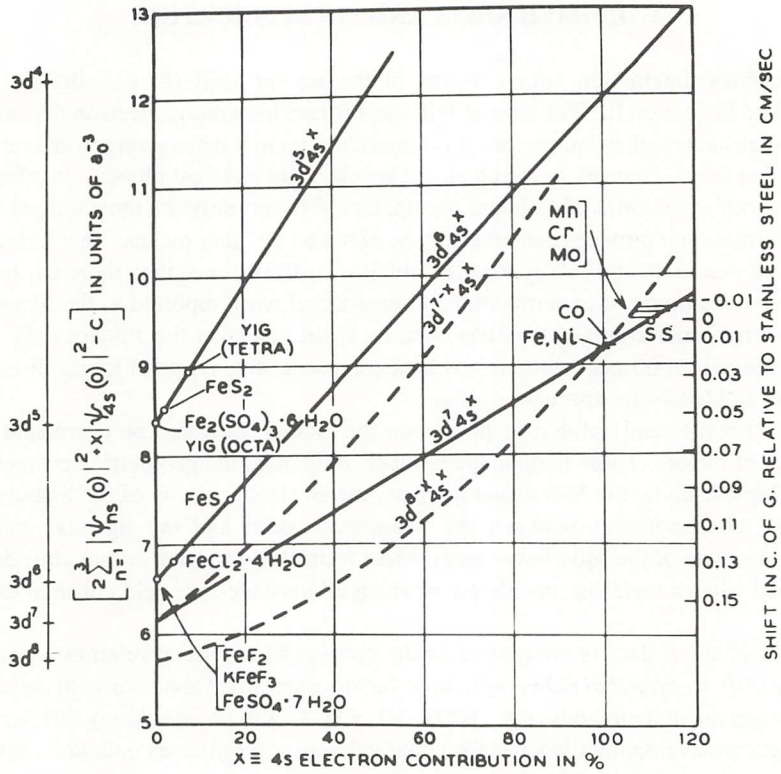

Fig. 6.19. Hartree-Fock calculations for the isomer shift of ^{57}Fe as a function of 3d- and 4s- electron charge density. Reproduced by permission from *Phys. Rev. Letters* (43).

where ϕ_M and ϕ_L are the atomic orbitals of the metals and its ligands. The coefficients a_M and a_L control the amount of mixing of each atomic orbital which gives the molecular orbital. An example of an energy diagram which results from these considerations is given in Fig. 6.21 for transition octahedral metal complexes containing ligands with bonding (17). The relative spacing of the energy of the molecular orbitals is related to the ligands and the geometric structure. The filling of these levels and values for the coefficients (a_M and a_L) are quite important in the interpretation of isomer shift data since they allow the determination of electron populations for the Mössbauer atom.

Extended Hückel MO theory provides a fairly simple procedure for obtaining the needed electron population to interpret Mössbauer parameters. In this procedure all atoms in the molecular system are considered. The basis set is usually taken from Slater-type atomic orbitals in which all the valence orbitals of each atom are considered. Overlap integrals are calculated, but Coulomb integrals are set equal to the proper valence state ionization energies (42). The Wolfsberg-Helmholtz approximation is used to obtain numerical results for the Hamiltonian matrix (47). This model has been successful as a semiempirical approach.

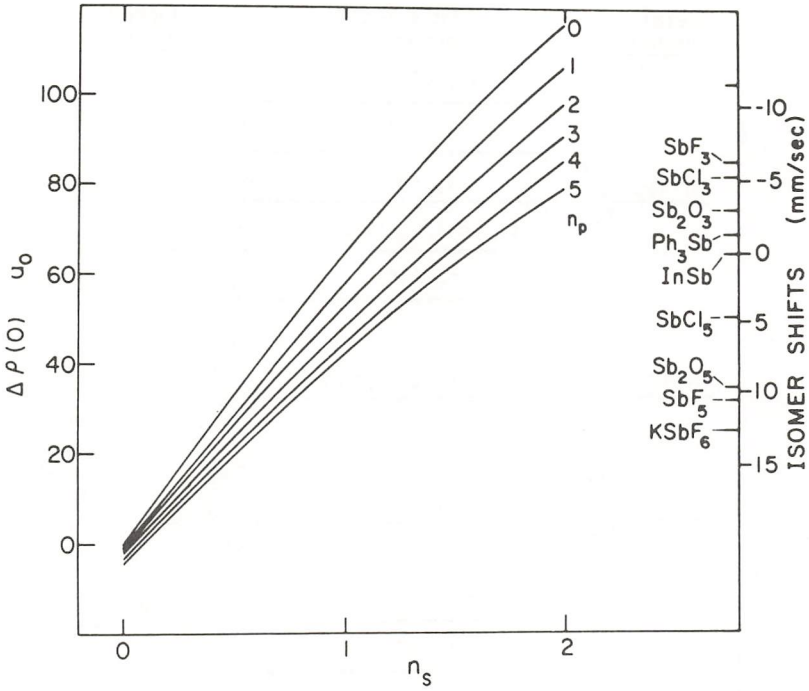

Fig. 6.20. Hartree-Fock calculations for the isomer shift of ^{121}Sb as a function of 5p- and 5s- electron charge density. Reproduced by permission from *Phys. Rev.* (32).

B. OXIDATION STATES

From Figs. 6.19 and 6.20, it can be seen that isomer shifts can easily be used in many cases to differentiate between oxidation states. Even for iron where the difference between Fe(II) and Fe(III) is only a $3d$ electron, it is usually fairly simple to differentiate between the two δ's for many compounds. While $3d$ electrons have essentially no direct effect on the electron density at the nucleus because they do not penetrate it, they do shield the $4s$ electron of an iron atom from the nucleus. Fig. 6.22 contains several examples of collected data showing the relation between δ and the oxidation state of the Mössbauer atom. In many cases, there is a distinct range of isomer shifts for a particular oxidation that does not overlap with the range of another.

C. ELECTRONEGATIVITY

Within the range of isomer shifts for a particular oxidation state, the second factor that affects these values is the electronegativities of the ligands. Generally, as the electronegativity of the ligand increases, there is a corresponding decrease in electron density at the nucleus. There are many cases of linear relations between the isomer shift and electronegativity or a related parameter. For example, many iodine-containing molecules are made of bonds which are only pure p. One such empirical

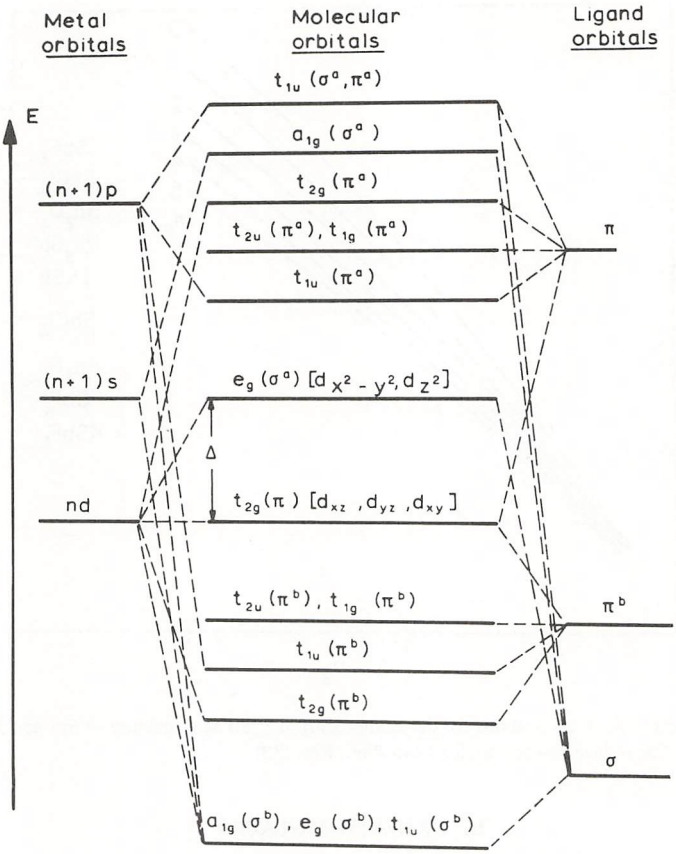

Fig. 6.21. Molecular orbital energy level diagram for octahedral metal complexes containing ligands with π^b (bonding) and relatively stable π^a (antibonding) orbitals. Reproduced from (17).

result for this class of compounds is

$$\delta = 0.136h_p - 0.54 \tag{41}$$

where h_p is the number of vacant "p" orbitals at the iodine (30). The values for h_p are directly related to electronegativity.

More commonly, the linear empirical relation exists directly between the isomer shift and the ligand electronegativity. Such an example is shown in Fig. 6.23. The resulting linear equations for these two series are $\delta = 2.6 + 0.019 \cdot$ (Ionicity in percent) for R_4SbX and $\delta = 1.4 + 0.034 \cdot$ (Ionicity in percent) for R_3SbX_2 (10).

D. PARTIAL CHEMICAL SHIFTS

Numerous cases of linear relations between ligand electronegativity and isomer shift have led to the concept of partial chemical shift (pcs) (18), i.e.,

$$\delta = \text{Constant} + \sum_{i=1}^{n} (\text{pcs})_i \tag{42}$$

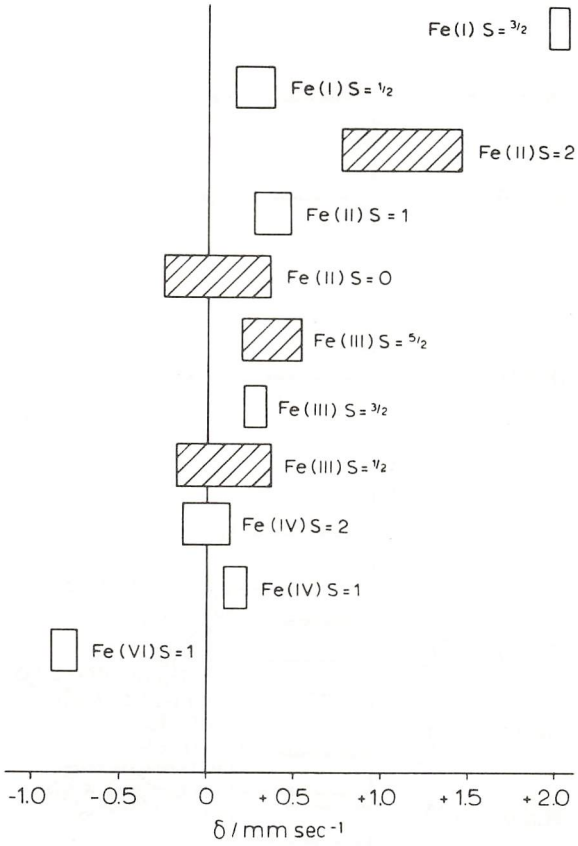

(a)

Fig. 6.22. Relation between isomer shift and oxidation state of several elements. (*a*) ^{57}Fe, reproduced from (29); (*b*) ^{99}Ru, reproduced from (19); (*c*) ^{119}Sn, reproduced from (20); (*d*) ^{121}Sb, reproduced from (16); (*e*) ^{170}Yb, reproduced from (21); (*f*) ^{197}Au, reproduced from (16); and (*g*) ^{237}Np, reproduced from (24).

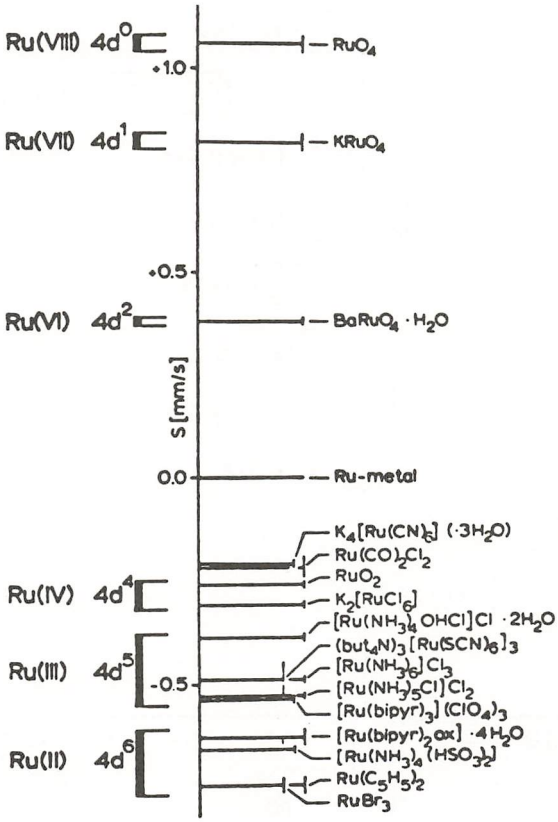

(b)

Fig. 6.22. (*Continued*).

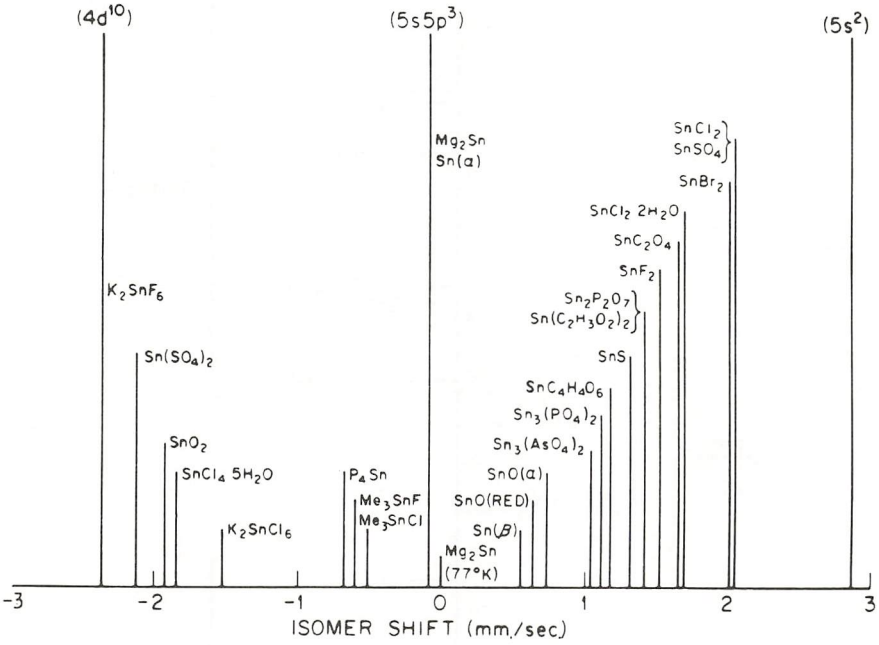

(c)

Fig. 6.22. (*Continued*).

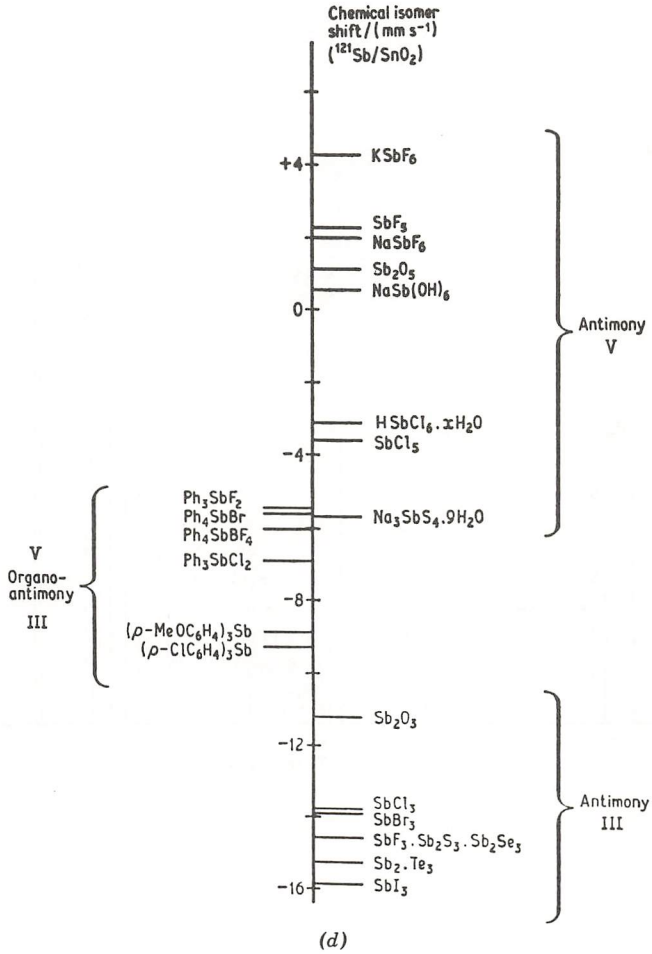

(d)

Fig. 6.22. (*Continued*).

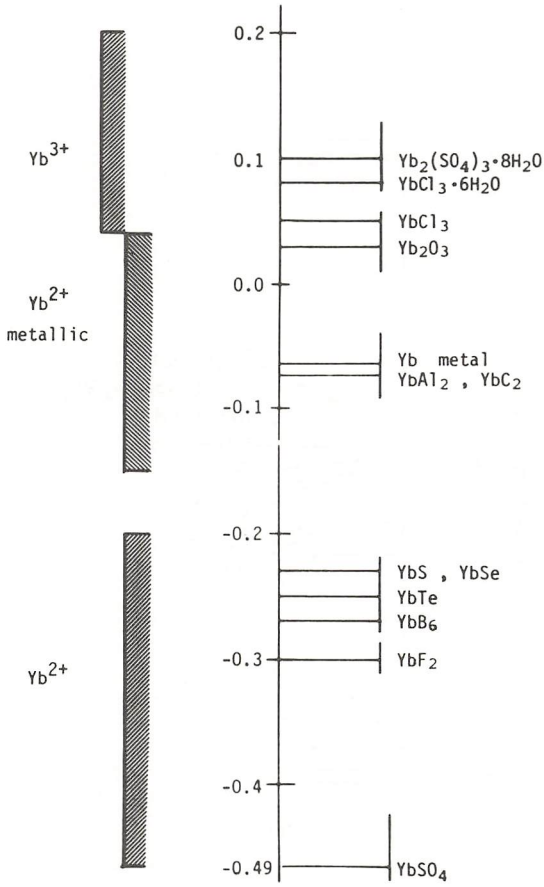

(e)

Fig. 6.22. (*Continued*).

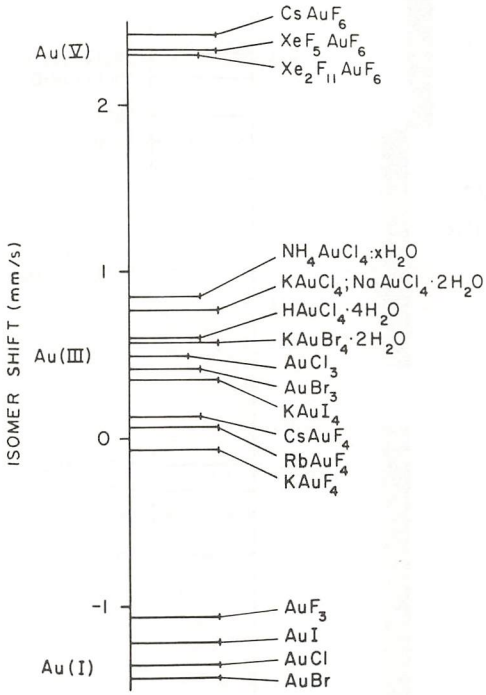

(f)

Fig. 6.22. (*Continued*).

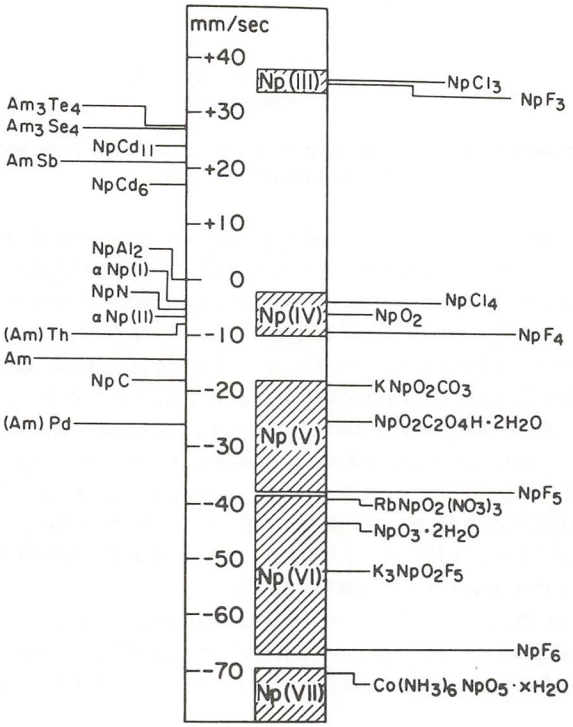

(g)

Fig. 6.22. (*Continued*).

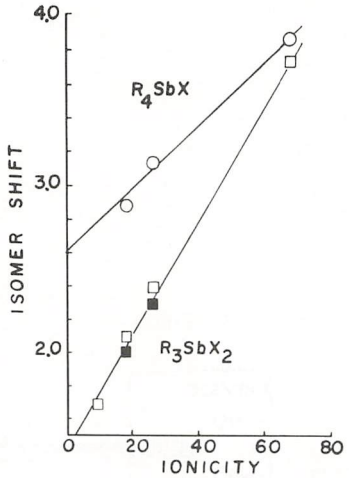

Fig. 6.23. Isomer shift vs. Pauling bond ionicity (of the SbX bond) from some organoantimony compounds. □, 0(R = C_6H_5); ■ R = CH_3. Reproduced from (10).

where n is the coordination number. Using pcs tables, it is possible to predict isomer shift values for various compounds, or conversely, isomer-shift data can possibly be used to determine geometric structures. For example, see the recent ^{121}Sb Mössbauer data summarized in Table 6.VIII for $Me_xSbCl_{(3-x)}$. X-ray single-crystal data is only available for $SbCl_3$, which indicates that the Cl's are trigonally coordinated to the antimony and the Cl–Sb–Cl bond angles are about 95° (25). It is unlikely that X-ray structural data can be obtained for the other three compounds due to the difficulty of growing single crystals and their reactivity. Mössbauer spectroscopy is then of special value because it gives clues to structure. In this particular example, it is apparent that the structures of all four species are quite similar since there is the constant change in δ's, i.e., $[pcs(CH_3^-) - pcs(Cl^-)] = 1.9$ mm/s and the model of partial chemical shifts requires that the structures in a series be the same.

The values of the pcs, as has been mentioned above, depend on a number of factors; but if all of these are kept constant and only the ligands are allowed to vary, then regardless of the particular Mössbauer isotope or the structure being considered,

TABLE 6.VIII

^{121}Sb Mössbauer Data for $Me_xSbCl_{(3-x)}$ (39)

x	δ (mm/s)	e^2qQ | exp (mm/s) (±1.0)	e^2qQ | theory (mm/s)	η exp (±0.1)	η theory
0	−5.9	+13.3	+15	0.2	0.0
1	−4.2	+31.0	+29	0.4	0.3
2	−2.5	−30.8	−28	0.8	0.6
3	−0.1	+15.8	+15	0.0	0.0

a special ordering is observed. That is, if the ligands are ordered according to their pcs values, the resulting series will be nearly identical to the spectrochemical series.

E. SECOND-ORDER DOPPLER SHIFT

Care must be taken when interpreting isomer-shift data because included with all isomer shift values is a very small contribution due to the second-order Doppler (SOD) shift. This contribution needs to be considered and corrected for in those few cases when it is significant enough to measurably change an isomer-shift value.

SOD shift results from the relativistic emission or absorption energy shift of a stationary system seen by another system that is moving; in this case the systems are the source and the absorber. This energy shift in the emitting (or absorbing) gamma is given by

$$\delta_{\mathrm{SOD}} = E_\gamma (1 + \mathrm{v}/c + 1/2\,(\mathrm{v}/c)^2 + \ldots) \tag{43}$$

The second term will average out since $\langle \mathrm{v} \rangle$ for a vibrating nulceus is zero; however $\langle \mathrm{v}^2 \rangle$ is nonzero. Therefore, the second-order term will contribute to an energy change in the gamma referred to as the second-order Doppler shift. The Debye model can be used to evaluate this shift (δ_{SOD}). One finds

$$\delta_{\mathrm{SOD}} = \frac{-3kT}{2mc}\left[\frac{3}{8}\frac{\theta_D}{T} + 3\left(\frac{T}{\theta_D}\right)^3 \int_0^{\theta_D/T} \frac{x^3 dx}{(e^x - 1)}\right] \tag{44}$$

Values of these shifts have been calculated for ^{57}Fe, ^{119}Sn, and ^{121}Sb and are in Table 6.IX.

TABLE 6.IX
Second-Order Doppler Shifts in mm/s

Isotope	Debye temperature (K)	Experiment temperature (K) 4.2	40	77	100	150	200	250	300
^{57}Fe	20	0.0059	0.0296	0.0564	0.0731	0.1096	0.1461	0.1826	0.2191
	40	0.0110	0.0306	0.0570	0.0736	0.1099	0.1463	0.1827	0.2192
	60	0.0164	0.0324	0.0579	0.0743	0.1104	0.1467	0.1830	0.2194
	80	0.0219	0.0348	0.0592	0.0753	0.1111	0.1472	0.1834	0.2198
	100	0.0274	0.0377	0.0609	0.0766	0.1119	0.1478	0.1840	0.2202
	120	0.0329	0.0411	0.0629	0.0782	0.1130	0.1486	0.1846	0.2208
	140	0.0383	0.0450	0.0652	0.0800	0.1142	0.1496	0.1854	0.2214
	160	0.0438	0.0491	0.0678	0.0821	0.1157	0.1506	0.1862	0.2221
	180	0.0493	0.0535	0.0707	0.0844	0.1173	0.1519	0.1872	0.2229
	200	0.0548	0.0582	0.0738	0.0870	0.1190	0.1532	0.1883	0.2239
	220	0.0602	0.0630	0.0772	0.0897	0.1210	0.1547	0.1895	0.2249
	240	0.0657	0.0680	0.0808	0.0927	0.1231	0.1563	0.1908	0.2260
	260	0.0712	0.0730	0.0847	0.0959	0.1254	0.1581	0.1923	0.2272
	280	0.0767	0.0782	0.0887	0.0993	0.1278	0.1600	0.1938	0.2285

TABLE 6.IX (Cont.)

Second-Order Doppler Shifts in mm/s

Isotope	Debye temperature (K)	Experiment temperature (K) 4.2	40	77	100	150	200	250	300
	300	0.0821	0.0834	0.0928	0.1028	0.1304	0.1620	0.1954	0.2298
	320	0.0876	0.0887	0.0971	0.1065	0.1332	0.1642	0.1972	0.2313
	340	0.0931	0.0940	0.1016	0.1104	0.1361	0.1664	0.1990	0.2329
	360	0.0986	0.0993	0.1062	0.1144	0.1391	0.1688	0.2010	0.2345
	380	0.1040	0.1047	0.1108	0.1185	0.1422	0.1713	0.2030	0.2363
	400	0.1095	0.1101	0.1156	0.1228	0.1455	0.1739	0.2052	0.2381
^{119}Sn	20	0.0028	0.0142	0.0270	0.0350	0.0525	0.0700	0.0874	0.1049
	40	0.0053	0.0147	0.0273	0.0352	0.0526	0.0701	0.0875	0.1050
	60	0.0079	0.0155	0.0277	0.0356	0.0529	0.0703	0.0877	0.1051
	80	0.0105	0.0167	0.0284	0.0361	0.0532	0.0705	0.0879	0.1053
	100	0.0131	0.0181	0.0292	0.0367	0.0536	0.0708	0.0881	0.1055
	120	0.0157	0.0197	0.0301	0.0374	0.0541	0.0712	0.0884	0.1057
	140	0.0184	0.0215	0.0312	0.0383	0.0547	0.0716	0.0888	0.1060
	160	0.0210	0.0235	0.0325	0.0393	0.0554	0.0722	0.0892	0.1064
	180	0.0236	0.0256	0.0338	0.0404	0.0562	0.0727	0.0897	0.1068
	200	0.0262	0.0279	0.0354	0.0417	0.0570	0.0734	0.0902	0.1072
	220	0.0288	0.0302	0.0370	0.0430	0.0580	0.0741	0.0908	0.1077
	240	0.0315	0.0326	0.0387	0.0444	0.0590	0.0749	0.0914	0.1082
	260	0.0341	0.0350	0.0405	0.0459	0.0601	0.0757	0.0921	0.1088
	280	0.0367	0.0375	0.0425	0.0476	0.0612	0.0766	0.0928	0.1094
	300	0.0393	0.0399	0.0445	0.0493	0.0625	0.0776	0.0936	0.1101
	320	0.0420	0.0425	0.0465	0.0510	0.0638	0.0786	0.0944	0.1108
	340	0.0446	0.0450	0.0487	0.0529	0.0652	0.0797	0.0953	0.1115
	360	0.0472	0.0476	0.0508	0.0548	0.0666	0.0809	0.0963	0.1123
	380	0.0498	0.0501	0.0531	0.0568	0.0681	0.0821	0.0973	0.1132
	400	0.0525	0.0527	0.0554	0.0588	0.0697	0.0833	0.0983	0.1140
^{121}Sb	20	0.0028	0.0139	0.0266	0.0345	0.0516	0.0688	0.0860	0.1032
	40	0.0052	0.0144	0.0268	0.0347	0.0518	0.0689	0.0861	0.1033
	60	0.0077	0.0153	0.0273	0.0350	0.0520	0.0691	0.0862	0.1034
	80	0.0103	0.0164	0.0279	0.0355	0.0523	0.0693	0.0864	0.1035
	100	0.0129	0.0178	0.0287	0.0361	0.0527	0.0696	0.0867	0.1037
	120	0.0155	0.0194	0.0296	0.0368	0.0532	0.0700	0.0870	0.1040
	140	0.0181	0.0212	0.0307	0.0377	0.0538	0.0705	0.0873	0.1043
	160	0.0206	0.0231	0.0319	0.0387	0.0545	0.0710	0.0877	0.1046
	180	0.0232	0.0252	0.0333	0.0398	0.0552	0.0715	0.0882	0.1050
	200	0.0258	0.0274	0.0348	0.0410	0.0561	0.0722	0.0887	0.1055
	220	0.0284	0.0297	0.0364	0.0423	0.0570	0.0729	0.0893	0.1059
	240	0.0310	0.0320	0.0381	0.0437	0.0580	0.0736	0.0899	0.1064
	260	0.0335	0.0344	0.0399	0.0452	0.0591	0.0745	0.0906	0.1070
	280	0.0361	0.0368	0.0418	0.0468	0.0602	0.0754	0.0913	0.1076
	300	0.0387	0.0393	0.0437	0.0484	0.0614	0.0763	0.0921	0.1083
	320	0.0413	0.0418	0.0458	0.0502	0.0627	0.0773	0.0929	0.1090
	340	0.0438	0.0443	0.0479	0.0520	0.0641	0.0784	0.0938	0.1097
	360	0.0464	0.0468	0.0500	0.0539	0.0655	0.0795	0.0947	0.1105
	380	0.0490	0.0493	0.0522	0.0558	0.0670	0.0807	0.0956	0.1113
	400	0.0516	0.0519	0.0545	0.0578	0.0686	0.0819	0.0967	0.1122

The isomer shift measured is a sum of the chemical isomer shifts, the primary contribution, and the second-order Doppler shift (δ_{SOD}), which in most cases can be ignored. Therefore, in general one has

$$\delta_{measure} = \delta_{SOD} + \delta \tag{45}$$

F. PHASE ANALYSIS

1. Phase Transitions

In most cases, the electronic structure is different enough in two different phases to allow the use of the isomer shift to determine if and where a phase transition has occurred. In these cases of first-order transitions, there will be a discontinuity in the isomer-shift value. The usual parameter varied is temperature.

Some spectrometers have been designed that operate at a single velocity set on an absorption peak. Then the temperature is varied and the number of gammas detected for each temperature increment is recorded. When a phase change occurs, the count rate will increase due to a decrease in resonance absorption. The resulting plot of counts versus temperature is called a thermal scan and is considerably less complicated than obtaining a complete Mössbauer spectrum at each temperature.

2. High Pressure

Besides temperature, the pressure can also be varied. This has been successfully accomplished for about 10 Mössbauer transitions. Studies have usually been centered around phase transitions and/or the effect of pressure on the isomer shift. There is a definite volume dependence of the isomer shift which can be expressed as

$$\left(\frac{\partial \delta}{\partial \ln V}\right)_T = \text{constant} \tag{46}$$

As for temperature, it is possible to vary the pressure as a function of the number of counts at a constant velocity.

3. Chemical Identification

Mössbauer spectroscopy can be used for assisting in the identification of particular chemical substances. For example, it has been used to identify those iron minerals found in samples brought back from the moon. In these identifications, the isomer shift is usually used along with possible quadrupole coupling and magnetic hyperfine data when attempting to identify unknown materials. Other active scientific areas of interest in which chemical identification is important include corrosion processes, mechanisms in catalysts, biological activity of iron-containing systems, and even the history of ancient artifacts, primarily pottery. Using Mössbauer spectroscopy as a fingerprint is discussed quite thoroughly in several chapters of a book by Bancroft (3). Numerous detailed examples can be found in Stevens and Shenoy (39a).

VI. MAGNETISM

A. LINE INTENSITIES

As discussed in an earlier section, there are six Mössbauer transitions observable for ^{57}Fe due to the interaction of the nuclear magnetic moment and a magnetic field. For these transitions $\Delta m_I = 0, \pm 1$. The intensities of these transitions have an angular dependence which is related to Δm_I. A convenient angle (θ) is defined as the angle between the directions of the magnetic field and the gamma-ray emission. A number of the angular relations are listed in Table 6.X. Usually there is no preferred direction, and thus the relative intensities of the peaks can be determined by averaging the angular dependence over all angles. For ^{57}Fe this gives a 3:2:1:1:2:3 ratio of line intensities. If a ^{57}Fe magnetic Mössbauer spectra does not give this ratio, then there is a preferred orientation in the material. For example, in the two extreme cases, $\theta = 0°$ gives 3:0:1:1:0:3 and $\theta = 90°$ gives 3:4:1:1:4:3. The spectrum shown in Fig. 6.8 is, in fact, closer to this latter ratio, indicating that the aligned fields in the foil are mainly in a direction approximately 90° relative to the gamma direction. It is useful to know if there are preferred magnetic field directions in materials and a determination of this is possible with Mössbauer spectroscopy. When preferred directions do exist these materials are said to have "texture."

B. CONTRIBUTIONS TO THE MAGNETIC FIELD INTERACTIONS

Besides magnetic fields due to external sources, there are three primary internal magnetic field interactions (44) which have been discussed previously in Section III.B. One of these, the Fermi contact interaction, results from a direct coupling between the spin density of s electrons at the nucleus and the nuclear spin. It can be expressed as

$$H_c = -\frac{16}{3}\pi\beta\sum_i \delta(\vec{r}_i)\,\vec{S}_i \cdot \vec{I} \tag{47}$$

where β is the Bohr magneton ($\beta = 9.274\text{x}/10^{-24}$ Joule/Tesla) and S_i is the core electron spin. The summation represents an imbalance of electron density at the nucleus. This polarization comes about via the unpaired electrons in the outer electron shells of the atom. The Fermi contact is usually the largest of the magnetic field interaction terms.

A second contribution to the internal magnetic field interaction is the orbital term

$$H_L = 2\beta\frac{1}{r^3}\vec{L} \cdot \vec{I} \tag{48}$$

There are several cases when this term is zero. These include those when an outer electronic shell is either half full and is high spin or completely full. For example, high-spin Fe(III) compounds do not have this magnetic field contribution.

While the Fermi contact considers the interaction of the nucleus and the spin density of the electrons at the nucleus, a third contribution considers the interaction

between the nuclear spin and the spin of the electrons outside of the nucleus. This is called the dipole interaction and the resulting field can be expressed as

$$H_D = -2\beta \left[3\vec{r}\frac{\vec{S}\cdot\vec{r}}{r^5} - \frac{\vec{S}}{r^3} \right] \cdot \vec{I} \tag{49}$$

The dipole contribution is usually quite small compared to the others and is zero in cases of cubic symmetry.

Other possible sources for an effective magnetic field include the conduction electrons that are polarized by neighboring atoms or other electrons in the atom. Also possibly contributing are fields produced by neighboring atoms either by overlap distortion of the core s orbitals or dipole fields of localized moments (41).

C. MAGNETIC HYPERFINE FIELD SPECTRA

The common difficulty encountered when interpreting quantitatively the Mössbauer data (δ, e^2qQ, magnetic hyperfine interaction) is not knowing the value of the nuclear components of the interaction equations. In the case of the magnetic hyperfine field interactions, however, the nuclear term (the nuclear moment or nuclear g factor) is often known well enough. Values of these are given in Table 6.XI. The nuclear g factors in this table are given in units such that the values in mm/s of observed spectra splittings can be then directly converted to units of Tesla. For example, (see Figs. 6.7 and 6.8 for α-Fe) using the g_0 and g_1 splittings in mm/s and the values 0.1188 mm/(S · T) and 0.06790 mm/(S · T), respectively, the value of 33 Tesla is obtained for the effective internal field of metallic iron.

VII. QUADRUPOLE INTERACTION AND ITS APPLICATION

A great deal of our understanding about the nuclear quadrupole interaction has come from NQR (nuclear quadrupole resonance) spectroscopy, which was already fairly well established when Mössbauer spectroscopy began to be used for making quadrupole measurements. While Mössbauer spectroscopy does not have the precision of NQR, it does add to our knowledge of quadrupole interactions because it enables observations of quadrupole coupling in many materials not possible with NQR. These are materials that have no quadrupole interaction in their ground states since their spins are either 0 or 1/2. However, excited nuclear states usually have spins of 1 or greater. As nuclei undergo Mössbauer transitions, their spectra reveal information about the quadrupole coupling in their excited states. Primary examples of such cases are ^{57}Fe and ^{119}Sn. Another contribution of Mössbauer spectroscopy to the study of quadrupole interactions is the easy determination of the sign of the quadrupole coupling constant. Examples include ^{121}Sb and ^{129}I.

A. ELECTRIC FIELD GRADIENTS

Quadrupole measurements give information about the electric field gradient (EFG). Although the EFG in general contains nine elements (see equation 25), the information of interest is condensed into two parameters: the principal diagonal

TABLE 6.X

Relative Line Intensities of Magnetic Hyperfine Interactions (15)

I_1	I_2	Multipolarity	Examples	$\lvert m_I(1)\rangle$	$\lvert m_I(2)\rangle$	$\lvert \Delta m_I \rvert$ [a]	A^2	$A^2(\theta = 0°)$ [b]	$A^2(\theta = 90°)$ [b]
3/2	1/2	M1	^{57}Fe, ^{119}Sn,	±3/2	±1/2	1	3	3	3
			^{125}Te	±1/2	±1/2	0	2	0	4
				∓1/2	±1/2	1	1	1	1
2	0	E2	^{166}Er, ^{170}Yb	±2	0	2	1	0	1
				±1	0	1	1	1	1
				0	0	0	1	0	0
5/2	3/2	M1	^{61}Ni, ^{99}Ru,	±5/2	±3/2	1	10	10	10
			^{155}Gd	±3/2	±3/2	0	4	0	8
				±1/2	±3/2	1	1	1	1
				±3/2	±1/2	1	6	6	6
				±1/2	±1/2	0	6	0	12
				∓1/2	±1/2	1	3	3	3
5/2	5/2	M1	^{161}Dy, ^{237}Np	±5/2	±3/2	0	25	0	25
				±3/2	±5/2	1	10	10	5
				±5/2	±3/2	1	10	10	5
				±3/2	±3/2	0	9	0	9
				±1/2	±3/2	1	16	16	8
				±3/2	±1/2	1	16	16	8
				±1/2	±1/2	0	1	0	1
				∓1/2	±1/2	1	18	18	9
7/2	5/2	M1	^{121}Sb, ^{127}I,	±7/2	±5/2	1	21	21	21
			^{129}I, ^{151}Eu	±5/2	±5/2	0	6	0	12
				±3/2	±5/2	1	1	1	1
				±5/2	±3/2	1	15	15	15
				±3/2	±3/2	0	10	0	20
				±1/2	±3/2	1	3	3	3
				±3/2	±1/2	1	10	10	10

				±1/2	±1/2	0	12	0	24
				∓1/2	±1/2	1	6	6	6
9/2	7/2	M1	^{191}Ta	±9/2	±7/2	1	36	36	36
				±7/2	±7/2	0	8	0	16
				±5/2	±7/2	1	1	1	1
				±7/2	±5/2	1	28	28	28
				±5/2	±5/2	0	14	0	28
				±3/2	±5/2	1	3	3	3
				±5/2	±3/2	1	21	21	21
				±3/2	±3/2	0	18	0	36
				±1/2	±3/2	1	6	6	6
				±3/2	±1/2	1	15	15	15
				±1/2	±1/2	0	20	0	40
				∓1/2	±1/2	1	10	10	10

[a] The angular dependence is related to the multipolarity and the $|\Delta m_I|$ value, i.e., or dipole radiation (M1)

$|\Delta m_I| = 0 : \sin^2\theta$

$|\Delta m_I| = 1 : (1 + \cos^2\theta)^{\frac{1}{2}}$

and for quadrupole radiation (E2)

$|\Delta m_I| = 0 : 3/4 \sin^2 2\theta$

$|\Delta m_I| = 1 : 1/2 (\cos^2\theta + \cos^2 2\theta)$

$|\Delta m_I| = 2 : 1/8 (4 \sin^2\theta + \sin^2 2\theta)$

where θ is the angle between the direction of the magnetic field and the direction of the emission of the gamma.

[b] A^2 are relative intensities.

TABLE 6.XI

Nuclear Magnetic Moment Data (38)[a]

Isotope	E_γ (keV)	I_e	I_g	Magnetic moment: μ_0 Ground (nuclear magnetons)	Magnetic moment: μ Excited (nuclear magneton)	Ratio of magnetic moments	Gyromagnetic ratio: g_0 Ground mm/(S · T)	Gyromagnetic ratio: g_1 Excited mm/(S · T)
^{57}Fe	14.4	3/2	1/2	0.090604(9)	−0.15532(4)	−1.7142(4)	0.118821(12)	−0.067897(17)
^{61}Ni	67.4	5/2	3/2	0.74980(10)	0.478(7)	−0.637(11)	0.070083(12)	0.0268(4)
^{99}Ru	89.4	3/2	5/2	−0.626(13)	−0.285(5)	0.456(2)	−0.0265(6)	−0.0201(4)
^{119}Sn	23.9	3/2	1/2	−1.0461(3)	0.633(18)	−0.605(17)	−0.8283(3)	0.167(5)
^{121}Sb	37.2	7/2	5/2	3.3591(6)	2.47(3)	0.735(9)	0.3418(2)	0.180(2)
^{125}Te	35.5	3/2	1/2	−0.8872(3)	0.604(6)	−0.681(4)	−0.4729(4)	0.1073(11)
^{127}I	57.6	7/2	5/2	2.8091(4)	2.54(4)	0.905(16)	0.18436(7)	0.1191(19)
^{129}I	27.8	5/2	7/2	2.6174(8)	2.797(3)	1.0687(11)	0.2545(2)	0.3808(5)
^{133}Cs	81.0	5/2	7/2	−2.5786(8)	3.443(21)	1.335(8)	−0.08596(3)	0.1607(10)
^{151}Eu	21.5	7/2	5/2	3.465(2)	2.587(3)	0.7465(6)	0.6083(4)	0.3244(3)
^{153}Eu	103.2	3/2	5/2	1.5294(7)	2.043(5)	1.336(3)	0.05604(3)	0.1248(3)
^{155}Gd	86.5	5/2	3/2	−0.2584(5)	−0.529(5)	2.05(2)	−0.01881(4)	−0.0231(2)
^{161}Dy	25.7	5/2	5/2	−0.479(5)	0.592(6)	−1.2368(14)	−0.0706(7)	0.0872(9)
^{166}Er	80.6	2	0	0.0	0.629(10)	—	0.0	0.0369(6)
^{170}Yb	84.3	2	0	0.0	0.669(8)	—	0.0	0.0375(4)
^{181}Ta	6.2	9/2	7/2	2.356(7)	5.24(7)	2.23(3)	1.020(4)	1.764(24)
^{193}Ir	73.0	1/2	3/2	0.1583(6)	0.4683(20)	2.958(6)	0.1366(5)	0.1212(5)
^{197}Au	77.3	1/2	3/2	0.1448(7)	0.416(3)	2.875(22)	0.01180(6)	0.1017(7)
^{237}Np	59.5	5/2	5/2	2.5(3)	1.34(12)	0.535(4)	0.159(19)	0.085(8)

[a] Uncertainties in the last digit(s) are given in the parenthesis.

TABLE 6.XII
The Elements of the Electric Field Gradient in Spherical Coordinates for a Point Charge q

$V_{xx} = qr^{-3}(3\sin^2\theta\cos^2\phi - 1)$
$V_{yy} = qr^{-3}(3\sin^2\theta\sin^2\phi - 1)$
$V_{zz} = qr^{-3}(3\cos^2\theta - 1)$
$V_{xy} = V_{yx} = qr^{-3}(3\sin^2\theta\sin\phi\cos\phi)$
$V_{xz} = V_{zx} = qr^{-3}(3\sin\theta\cos\theta\cos\phi)$
$V_{yz} = V_{zy} = qr^{-3}(3\sin\theta\cos\theta\sin\phi)$

component of the diagonalized EFG (see equation 26a) and the asymmetry parameter (see equation 26b).

The elements of the EFG for a single point charge q are given in Table 6.XII. In generalized coordinates these elements are

$$V_{ij} = q(3x_i x_j - r^2\,\delta_{ij}).$$

When there are several point charges, the contributions from each must be added to obtain the EFG elements of the configuration. The source of the point charges are either valence electrons or ligands. The contributions to the EFG can often be obtained from theoretical calculations using molecular orbital-wave functions. For convenience, the EFG should be diagonalized. By choosing the most apparent symmetry axis of the system as the z axis, the EFG matrix will usually be diagonalized with V_{zz} as the maximum valued element.

An immediate application of the terms in Table 6.XII can be made by comparing the ligand contribution of the *cis*- and *trans*-octahedral complexes of type MA_2B_4. The diagonalized matrix elements for the *cis*-ligand complex are

$$\begin{aligned} V_{xx} &= V_{yy} = (A - B)e \\ V_{zz} &= (-2A + 2B)e \end{aligned} \tag{51}$$

where $A = Z_A/r_A^2$ and $B = Z_B/r_B^2$. The asymmetry parameter, $\eta = 0$. Likewise, for the *trans*-ligand complex, the diagonal elements are

$$\begin{aligned} V_{xx} &= V_{yy} = -2(A - B)e \\ V_{zz} &= -2(-2A + 2B)e \end{aligned} \tag{52}$$

and the asymmetry parameter $\eta = 0$ once again. Note the difference in sign and a factor of 2 when comparing equation 51 with equation 52. Mössbauer spectroscopy allows for easy differentiation between these two structures. The success of the Mössbauer results is demonstrated in Table 6.XIII.

As mentioned above, valence electrons can also contribute to the EFG. S electron wave functions are spherical and therefore do not contribute to the EFG. Likewise, if the valence p or d shells are half filled with no spin-pairing or completely filled, there is no contribution to the EFG. In all other cases, valence electrons contribute to the components of the diagonalized EFG. The q values (see equation 26a) for each of the p and d electrons are listed in Table 6.XIV.

TABLE 6.XIII

Comparison of Quadrupole Splittings for *cis-trans* Isomers of Low-Spin Fe(II) (4,7)

Compounds	Δ (mm/s)
trans-$FeCl_2(ArNC)_4$[a]	+1.55
cis-$FeCl_2(ArNC)_4$	−0.78
trans-$Fe(SnCL_3)_2(ArNC)_4$	(+)1.05
cis-Fe $(SnCl_3)_2(ArNC)_4$	(−)0.50
trans-Fe $(CN)_2(EtNC)_4$	−0.60
cis-Fe $(CN)_2(EtNC)_4$	(+)0.30

[a] ArNC = *p*-methoxyphenylisocyanide.

A general expression for the total q value can be written by summing the contributions from the ligands (lattice) and the valence electrons, i.e.,

$$q = (1 - \gamma_\infty)\, q_{\text{lattice}} + (1 - R)\, q_{\text{valence}}$$

where γ_∞ and R are Sternheimer antishielding factors. These factors correct for the polarization of the core electrons by the ligands (γ_∞) and the valence electrons (R). They can be calculated from self-consistent field methods.

The valence term can be further subdivided into the contributions from the crystal field and from the electrons in the molecular orbitals that are created by the metal and its ligands. The crystal field term will be important when considering nontransition metal complexes. Using the values in Table 6.XIV, an expression for the p (q_p) and d (q_d) contributions can be written based on the populations of the atomic orbitals, i.e.,

$$q_p = \frac{-4/5\,(1 - R_p)\,[N_z - 1/2\,(N_x + N_y)]}{\langle r_p^{-3} \rangle} \tag{53}$$

TABLE 6.XIV

Magnitude of the Diagonal Electric Field Gradient Tensor Elements for p and d Electrons

Wavefunction	V_{xx} $(e\langle r^{-3}\rangle)$	V_{yy} $(e\langle r^{-3}\rangle)$	V_{zz} $(e\langle r^{-3}\rangle)$
p_x	−4/5	+2/5	+2/5
p_y	+2/5	−4/5	+2/5
p_z	+2/5	+2/5	−4/5
d_{xy}	−2/7	−2/7	+4/7
d_{xz}	−2/7	+4/7	−2/7
d_{yz}	+4/7	−2/7	−2/7
d_{x2-y2}	−2/7	−2/7	+4/7
d_{z2}	+2/7	+2/7	−4/7

$$q_d = \frac{-4/7\,(1 - R_d)\,[N_{z2} + 1/2\,(N_{xz} + N_{yz}) - (N_{x2-y2} + N_{xy})]}{\langle r_d^{-3} \rangle} \tag{54}$$

The lattice term can be evaluated if it is assumed that contributions come from only the nearest neighbor. When the particular geometry is known, the components of the EFG can be found from Table 6.XV. The remaining quantities to be determined are the charges (Z_A, Z_B, ...) and the radii ($1/r_A^3$, $1/r_B^3$, ...). It is possible to use MO calculations for the Z values and structural data for the $1/r^3$ values. Another method for evaluating this data which is qualitative, will be described in the Section "Additive Models."

Recall from equation 26b that the values of the diagonalized elements of the EFG all contribute to the asymmetry parameter, η. If $V_{xx} = V_{yy}$ (true for the many complexes that have cylindrical symmetry), then $\eta = 0$. The other extreme occurs when either V_{xx} or V_{yy} is equal to zero; then $\eta = 1$. It is unfortunate that for ^{57}Fe and ^{119}Sn Mössbauer spectroscopy the value for η cannot be determined from data for the pure quadrupole interaction. This is due to the fact that the measured quadrupole splitting (Δ) is a function of both q and η (see equation 31), therefore not allowing for the independent determination of these two parameters. However, these quantities can be determined from Mössbauer spectra of higher-spin nuclei. For ^{57}Fe and ^{119}Sn, it is possible to determine η by removing the remaining degeneracy in nuclear levels through the application of a magnetic field.

B. SPECTRA

As discussed in Section III.C, when a nucleus has a nuclear quadrupole moment and an electric field gradient is present, the nuclear level splits into $(2I - 1)$ levels. The energies of the two resulting levels for $I = 3/2$ are given in equation 30. It is not possible to express the energies of the split levels for most cases of I in closed form. A series approximation has been worked out for the various I states (33). These can be obtained by using the series expression for the split energy levels:

$$E_q(I,m_I) = e^2 q\, Q \sum_{n=0}^{4} a_n(I,m_I)\eta^n \tag{55}$$

The values for a_n are given in Table 6.XVI. The Mössbauer spectra will indicate quadrupole splittings, if they are present, in both the excited and the ground nuclear levels. The shift for each possible Mössbauer line (ΔE_Q) can then be expressed as

$$\Delta E_Q = E_Q^* - E_Q \tag{56}$$

where the * represents the excited nuclear level. When $I \geqslant 1$ for both excited and ground nuclear levels, one may substitute equation 56 into equation 55 giving the energy shift as

$$\Delta E(I,m_I) = e^2 q\, Q\, [R_Q E_Q^*(I^*, m_{I^*}) - E_Q(I,m_I)] \tag{57}$$

TABLE 6.XV.

Point Charge Model Expressions for the Components of the EFG Tensor at a Nucleus M Due to Ligands A,B,C,D for Common Structures (5)

Structure	Components of the EFG [a,b]	Structure	Compound of the EFG
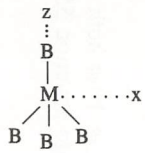	$V_{zz} = V_{xx} = V_{yy} = 0$	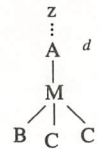	$V_{zz} = \{2[A] - 2/3([B] + 2[C])\}e$ $V_{yy} = \{-[A] - [B] + 2[C]\}e$ $V_{xx} = \{-[A] + 5/3\,[B] - 2/3[C]\}e$ $V_{xz} = V_{zx} = \{\sqrt{2}/3(-2[B] + 2[C])\}e$ $V_{xy} = V_{yx} = V_{yz} = V_{zy} = 0$ $\eta \neq 0$
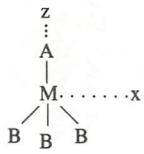	$V_{zz} = \{2[A] - 2[B]\}e$ $V_{yy} = \{-[B] + [A]\}e$ $V_{xx} = \{+[B] + [A]\}e$ $\eta = 0$		$\Delta = 1/2e^2Q(4/3p^2 + 8/3\,Q^2)^{1/2}$ $P = [A] + [B] - 2[C]$ $Q = [A] - [B]$ Sign = sign of P
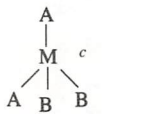	$V_{zz} = \{2[A] - 2[B]\}e$ $V_{yy} = \{2[B] - 2[A]\}e$ $V_{xx} = 0$ $\eta = 1$	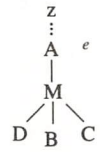	$V_{zz} = \{2[A] - 2/3([B] + [C] + [D])\}e$ $V_{yy} = \{-[A] - [B] + [C] + [D]\}e$ $V_{xx} = \{-[A] + 5/3[B] - 1/3([C] + [D])\}e$ $V_{yz} = V_{zy} = \{\sqrt{2}/\sqrt{3}([C] - [D])\}e$ $V_{xz} = V_{zx} = \{\sqrt{2}/3(-2[B] + [C] + [D])\}e$ $V_{xy} = V_{yx} = \{2/\sqrt{3}([C] - [B])\}e$ $\eta \neq 0$
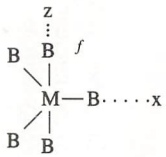	$V_{zz} = \{4[B]^{\mathrm{tba}} - 3[B]^{\mathrm{tbe}}\}e$ $V_{yy} = \{3/2[B]^{\mathrm{tbe}} - 2[B]^{\mathrm{tba}}\}e$ $V_{xx} = \{3/2[B]^{\mathrm{tbe}} - 2[B]^{\mathrm{tba}}\}e$ $\eta = 0$	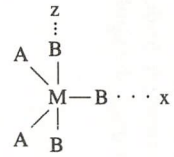	$V_{zz} = \{-2[A]^{\mathrm{tbe}} - [B]^{\mathrm{tbe}} + 4[B]^{\mathrm{tba}}\}e$ $V_{yy} = \{5/2[A]^{\mathrm{tbe}} - [B]^{\mathrm{tbe}} - 2[B]^{\mathrm{tba}}\}e$ $V_{xx} = \{-1/2[A]^{\mathrm{tbe}} + 2[B]^{\mathrm{tbe}} - 2[B]^{\mathrm{tba}}\}e$ $\eta = 0$

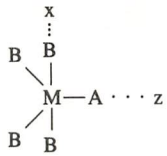

$$V_{zz} = \{2[A]^{\mathrm{tbe}} - 2[B]^{\mathrm{tba}} - 1/2[B]^{\mathrm{tbe}}\}e$$
$$V_{yy} = \{-[A]^{\mathrm{tbe}} - 2[B]^{\mathrm{tba}} + 5/2[B]^{\mathrm{tbe}}\}e$$
$$V_{xx} = \{-[A]^{\mathrm{tbe}} + 4[B]^{\mathrm{tba}} - 2[B]^{\mathrm{tbe}}\}e$$
$$\eta \neq 0$$

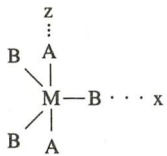

$$V_{zz} = \{4[A]^{\mathrm{tba}} - 3[B]^{\mathrm{tbe}}\}e$$
$$V_{yy} = \{-2[A]^{\mathrm{tba}} + 3/2[B]^{\mathrm{tbe}}\}e$$
$$V_{xx} = \{-[A]^{\mathrm{tba}} + 3/2[B]^{\mathrm{tbe}}\}e$$
$$\eta = 0$$

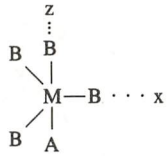

$$V_{zz} = \{2[A]^{\mathrm{tba}} - 3[B]^{\mathrm{tbe}} + 2[B]^{\mathrm{tba}}\}e$$
$$V_{yy} = \{-[A]^{\mathrm{tba}} + 3/2[B]^{\mathrm{tbe}} - [B]^{\mathrm{tba}}\}e$$
$$V_{xx} = \{-[A]^{\mathrm{tba}} + 3/2[B]^{\mathrm{tbe}} - [B]^{\mathrm{tba}}\}e$$
$$\eta = 0$$

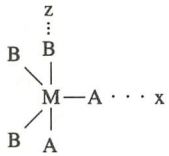

$$V_{zz} = \{2[B]^{\mathrm{tba}} - 2[B]^{\mathrm{tbe}} + 2[A]^{\mathrm{tba}} - [A]^{\mathrm{tbe}}\}e$$
$$V_{yy} = \{-[B]^{\mathrm{tba}} + 5/2[B]^{\mathrm{tbe}} - [A]^{\mathrm{tba}} - [A]^{\mathrm{tbe}}\}e$$
$$V_{xx} = \{-[B]^{\mathrm{tba}} - 1/2[B]^{\mathrm{tbe}} - [A]^{\mathrm{tba}} + 2[A]^{\mathrm{tbe}}\}e$$
$$\eta \neq 0$$

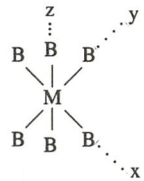

$$V_{zz} = V_{xx} = V_{yy} = 0$$

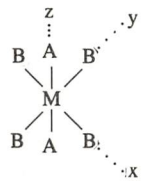

$$V_{zz} = \{4[A] - 4[B]\}e$$
$$V_{yy} = \{2[B] - 2[A]\}e$$
$$V_{xx} = \{2[B] - 2[A]\}e$$
$$\eta = 0$$

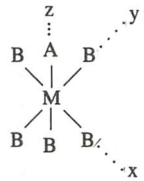

$$V_{zz} = \{2[A] - 2[B]\}e$$
$$V_{yy} = \{[B] - [A]\}e$$
$$V_{xx} = \{[B] - [A]\}e$$
$$\eta = 0$$

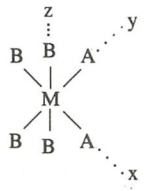

$$V_{zz} = \{2[B] - 2[A]\}e$$
$$V_{yy} = \{[A] - [B]\}e$$
$$V_{xx} = \{[A] - [B]\}e$$
$$\eta = 0$$

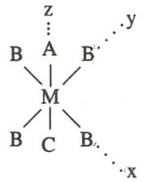

$$V_{zz} = \{2[A] + 2[C] - 4[B]\}e$$
$$V_{yy} = \{2[B] - [A] - [C]\}e$$
$$V_{xx} = \{2[B] - [A] - [C]\}e$$
$$\eta = 0$$

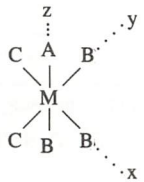

$$V_{zz} = \{2[A] - 2[C]\}e$$
$$V_{yy} = \{[C] - [A]\}e$$
$$V_{xx} = \{[C] - [A]\}e$$
$$\eta = 0$$

TABLE 6.XV. *(Cont.)*

Point Charge Model Expressions for the Components of the EFG Tensor at a Nucleus M Due to Ligands A,B,C,D for Common Structures (5).

Structure	Components of the EFG [a,b]	Structure	Compound of the EFG
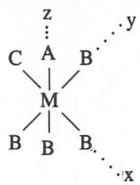	$V_{zz} = \{2[A] - [B] - [C]\}e$ $V_{zz} = \{-[B] + 2[C] - [A]\}e$ $V_{yy} = \{2[B] - [C] - [A]\}e$ $\eta \neq 0$	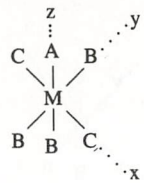	$V_{zz} = \{2[A] - 2[C]\}e$ $V_{xx} = \{4[C] - 3[B] - [A]\}e$ $V_{yy} = \{3[B] - 2[C] - [A]\}e$ $\eta \neq 0$
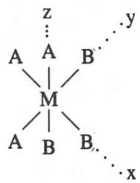	$V_{zz} = V_{yy} = V_{xx} = 0$	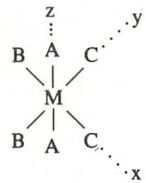	$V_{zz} = \{4[A] - 2[B] - 2[C]\}e$ $V_{yy} = \{[C] + [B] - 2[A]\}e$ $V_{xx} = \{[C] + [B] - 2[A]\}e$ $\eta = 0$
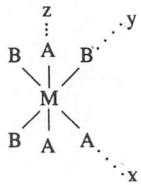	$V_{zz} = \{3[A] - 3[B]\}e$ $V_{yy} = \{3[B] - 3[A]\}e$ $V_{xx} = 0$ $\eta = 1$	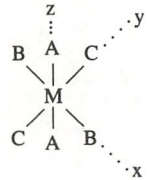	$V_{zz} = \{4[A] - 2[B] - 2[C]\}e$ $V_{xx} = \{4[B] - 2[C] - 2[A]\}e$ $V_{yy} = \{4[C] - 2[B] - 2[A]\}e$ $\eta \neq 0$

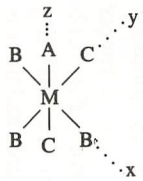

$V_{zz} = \{2[A] + [C] - 3[B]\}e$
$V_{xx} = \{3[B] - 2[C] - [A]\}e$
$V_{yy} = \{[C] - [A]\}e$
$\eta \neq 0$

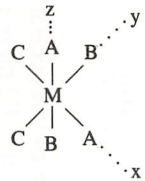

$V_{zz} = \{[A] + [B] - 2[C]\}e$
$V_{yy} = \{[B] + [C] - 2[A]\}e$
$V_{xx} = \{[A] + [C] - 2[B]\}e$
$\eta \neq 0$

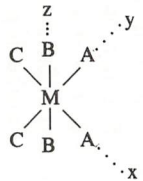

$V_{zz} = \{4[B] - 2[A] - 2[C]\}e$
$V_{yy} = \{[A] + [C] - 2[B]\}e$
$V_{xx} = \{[A] + [C] - 2[B]\}e$
$\eta = 0$

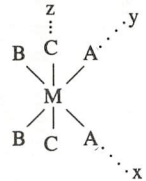

$V_{zz} = \{4[C] - 2[A] - 2[B]\}e$
$V_{yy} = \{[A] + [B] - 2[C]\}e$
$V_{xx} = \{[A] + [B] - 2[C]\}e$
$\eta = 0$

---

[a] The choice of EFG axes is usually indicated on the diagram of the structure or in a footnote. In all cases, except the four-coordinate $MABC_2$ and MABCD structures, this choice of axes serves to diagonalize the EFG tensor. The ordering of the axes to preserve the convention $|V_{zz}| \geq |V_{yy}| \geq |V_{xx}|$ will depend on the $[L]$ values. Thus, the final choice of axes may not be the same as given here; i.e., V_{zz} may become V_{xx} or V_{yy}, etc.

[b] Whenever η is not 0 or 1, it is easily calculated (after diagonalizing the tensor), taking $|V_{xx}| \leq |V_{yy}| \leq |V_{zz}|$, and using $\eta = (V_{xx} - V_{yy})/V_{zz}$. For example, take the third last structure in the table, $MA_2B_2C_2$: $\eta = 3[C] - 3[B]/[B] + [C] - 2[A]$.

[c] The x axes coincide with the C_2 symmetry axis, and the y and z axes lie in the symmetry planes.

[d] The y axis is perpendicular to the symmetry plane, while the x and z axes lie in the plane. The orientation of the x and z axes depends on the relative magnitudes of $[A]$, $[B]$, and $[C]$, and the tensor must be diagonalized separately for each case considered. The P and Q expressions lead to the magnitude of the quadrupole splitting and is obtained from the symmetrized parameters of Clark (2).

[e] The EFG tensor must be diagonalized for each example considered.

[f] The superscripts tbe and tba refer to trigonal-bipyramidal equatorial and trigonal-bipyramidal axial bonds, respectively.

TABLE 6.XVI

Eigenvalue Coefficients (A_n) for the Nuclear Quadrupole Interaction (33)

I	m_I	a_0	a_1	a_2	a_3	a_4
3/2	±3/2	0.2500	−0.0001	0.0425	−0.0020	−0.0017
	±1/2	−0.2500	−.0001	−0.0425	0.0020	0.0017
2	2	0.2500	0	0	0	0
	1	−0.1250	0.1250	0	0	0
	0	−0.2500	0.0001	−0.0425	0.0020	0.0017
	−1	−0.1250	−0.1250	0	0	0
	−2	0.2500	−0.0001	0.0425	−0.0020	−0.0017
5/2	±5/2	0.2500	0.0003	0.0125	0.0020	−0.0003
	±3/2	−0.0500	−0.0001	0.0880	−0.0431	0.0006
	±1/2	−0.2000	0.0001	−0.1005	0.0410	−0.0006
7/2	±7/2	0.2500	0.0001	0.0063	0.0048	−0.0026
	±5/2	0.0357	0.0008	0.0242	0.0124	−0.0058
	±3/2	−0.1071	−0.0009	0.1318	−0.1327	0.0417
	±1/2	−0.1785	0.0003	−0.1659	0.1239	−0.0385
9/2	±9/2	0.2500	−0.0004	0.0077	−0.0020	0.0009
	±7/2	0.0833	0.0001	0.0201	−0.0014	0.0017
	±5/2	−0.0417	0.0009	0.0359	0.0253	−0.0204
	±3/2	−0.1250	0.0052	0.1404	−0.2085	0.0842
	±1/2	−0.1667	−0.0048	−0.2066	0.1898	−0.0679

R_Q is the ratio of the excited nuclear quadrupole moment to that of the ground nuclear quadrupole moment. Values of R_Q are listed in Table 6.XVII. If $I = 0$ or 1/2 for one of the nuclear levels, then simply

$$E_Q = E_Q\,(I, m_I) \text{ or}$$
$$E_Q = E_Q^*\,(I^*, m_I{*}) \tag{58}$$

Table 6.XVII also gives values for the nuclear quadrupole moments and for the quadrupole coupling constant e^2qQ, which are needed for evaluating and interpreting quadrupole Mössbauer spectra.

The only remaining items that need to be evaluated are the transition intensities for each Mössbauer line. Again, in most cases, these are not known in closed form, but have been evaluated as a series (33). The intensities can be expressed as

$$A(I^*, I, m_I{*}, m_I) = \sum_{n=0}^{4} b_n\,(I^*, I, m_I{*}, m_I)\eta^n \tag{59}$$

where the values of b_n are given in Table 6.XVIII.

In Fig. 6.24 ^{121}Sb is considered in which plots are shown of the energy splittings, the relative intensity of each transition, and the effect of η on the relative energy positions of each peak. An example spectrum in which $\eta = 0$ is shown in Fig. 6.11.

For many substances $\eta = 0$, simplifying a number of factors. For ^{57}Fe and ^{119}Sn, the spectra reduce to doublets (see Fig. 6.10). If the absorber is powdered and there is

TABLE 6.XVII

Nuclear Quadrupole Moment Data (38)

Isotope	E_γ	I_e	I_g	Quadrupole Moments Q_0 ground[a]	Q excited[a]	Ratio of quadrupole moments[a]	$\frac{eQ}{4I(2I-1)}$ [10^{-22} (mm/s)($V \cdot m^2$)] Ground[a]	Excited[a]
^{57}Fe	14.4	3/2	1/2	0.0	0.21(1)[s]		0.0	0.364(17)
^{61}Ni	67.4	5/2	3/2	0.162(15)[s]	−1.21(13)[s]	−1.21(13)	0.060(6)	−0.134(15)
^{99}Ru	89.4	3/2	5/2	0.12(3)	0.35(9)	2.93(5)	0.010(3)	0.10(3)
^{119}Sn	23.9	3/2	1/2	0.0	−0.06		0.0	−0.063(11)
^{121}Sb	37.2	7/2	5/2	0.28(6)	−0.38(8)	1.340(10)	−0.057(17)	−0.37(8)
^{125}Te	35.5	3/2	1/2	0.0	−0.20(2)		0.0	−0.141(14)
^{127}I	57.6	7/2	5/2	−0.79(10)	−0.71(9)	−0.896(2)	−0.103(13)	−0.044(6)
^{129}I	27.8	5/2	7/2	−0.55(7)	−0.68(6)	1.2380(16)	−0.071(9)	−0.184(16)
^{133}Cs	81.0	5/2	7/2	−0.0030(7)			−0.00013(3)	
^{151}Eu	21.5	7/2	5/2	1.14(5)	1.50(7)	1.312(9)	0.397(17)	0.249(12)
^{153}Eu	103.2	3/2	5/2	2.90(12)	1.51(6)	0.520(3)	0.211(9)	0.366(15)
^{155}Gd	86.5	5/2	3/2	1.59(16)	0.32(8)	0.20(5)	0.46(5)	0.028(7)
^{161}Dy	25.7	5/2	5/2	2.35(16)[s]	2.34(16)[s]	0.9996(4)	0.69(5)	0.68(5)
^{166}Er	80.6	2	0	0.0	−1.59(15)		0.0	−0.247(23)
^{170}Yb	84.3	2	0	0.0	−2.11(11)		0.0	−0.313(16)
^{181}Ta	6.2	9/2	7/2	3.9(4)	4.4(5)	1.133(10)	2.23(23)	1.47(17)
^{193}Ir	73.0	1/2	3/2	0.70(18)	0.0		0.24(6)	0.0
^{197}Au	77.3	1/2	3/2	0.594(10)	0.0		0.192(3)	0.0
^{237}Np	59.5	5/2	5/2	4.1(7)	4.1(7)	0.990(10)	0.52(9)	0.52(9)

[a] Uncertainties in the last digit(s) are given in the parenthesis.

[s] Sternheimer corrected

TABLE 6.XVIII

Intensity Coefficients (b_n) for the Nuclear Quadrupole Interaction (33)

I^*	I	m_I^*	m_I	b_0	b_1	b_2	b_3	b_4
7/2	9/2	±7/2	±9/2	0.2000	0	−0.0021	0.0003	−0.0005
		±7/2	±7/2	0.0444	−0.0001	0.0014	−0.0009	0.0007
		±7/2	±5/2	0.0056	0.0001	−0.0003	−0.0001	0.0007
		±7/2	±3/2	0	−0.0001	0.0007	0.0011	0.0011
		±7/2	±1/2	0	0.0001	0.0002	−0.0003	0.0002
		±5/2	±9/2	0	0	0.0019	−0.0007	0.0006
		±5/2	±7/2	0.1555	−0.0007	−0.0027	−0.0168	0.0093
		±5/2	±5/2	0.0778	0.0028	−0.0245	0.0725	−0.0346
		±5/2	±3/2	0.0167	−0.0073	0.0321	−0.0546	0.0224
		±5/2	±1/2	0	0.0051	−0.0058	−0.0020	0.0031
		±3/2	±9/2	0	0	0.0004	0	0
		±3/2	±7/2	0	0.0007	−0.0025	0.0229	−0.0118
		±3/2	±5/2	0.1167	−0.0135	−0.0190	0.0275	−0.0178

TABLE 6.XVIII (Cont.)

Intensity Coefficients (b_n) for the Nuclear Quadrupole Interaction (33)

I^*	I	m_I^*	m_I	b_0	b_1	b_2	b_3	b_4
		±3/2	±3/2	0.1000	0.0640	0.1008	−0.2557	0.1359
		±3/2	±1/2	0.033	−0.0513	−0.0790	0.2043	−0.1058
		±1/2	±9/2	0	0	0	0.0001	0
		±1/2	±7/2	0	0	0.0041	−0.0055	0.0020
		±1/2	±5/2	0	0.0105	0.0441	−0.1003	0.0519
		±1/2	±3/2	0.0833	−0.0566	−0.1327	0.3076	−0.1564
		±1/2	±1/2	0.1667	0.0461	0.0847	−0.2021	0.1026
5/2	7/2	±5/2	±7/2	0.2500	0.0007	−0.0097	0.0100	−0.0061
		±5/2	±5/2	0.0715	0.0001	0.0011	−0.0033	0.0064
		±5/2	±3/2	0.0120	−0.0027	0.0037	0.0029	−0.0041
		±5/2	±1/2	0	0.0013	0.0021	−0.0045	0.0017
		±3/2	±7/2	0	−0.0004	0.0040	−0.0001	0.0009
		±3/2	±5/2	0.1784	0.0014	−0.0677	0.0839	−0.0338
		±3/2	±3/2	0.1189	0.0043	0.2327	−0.3327	0.1393
		±3/2	±1/2	0.0356	−0.0033	−0.1743	0.2543	−0.1081
		±1/2	±7/2	0	−0.0012	0.0056	−0.0058	0.0020
		±1/2	±5/2	0	−0.0017	0.0672	−0.0819	0.0286
		±1/2	±3/2	0.1191	−0.0011	−0.2379	0.3294	−0.1340
		±1/2	±1/2	0.2140	0.0099	0.1344	−0.1907	0.0775
5/2	5/2	±5/2	±5/2	0.2381	0	−0.0110	−0.0022	0.0007
		±5/2	±3/2	0.0952	0.0009	−0.0251	0.0454	−0.0154
		±5/2	±1/2	0	−0.0008	0.0361	−0.0435	0.0149
		±3/2	±5/2	0.0952	0.0009	−0.0251	0.0454	−0.0154
		±3/2	±3/2	0.0857	−0.0035	0.2519	−0.3138	0.1109
		±3/2	±1/2	0.1524	0.0025	−0.2265	0.2679	−0.0952
		±1/2	±5/2	0	−0.0008	0.0361	−0.0435	0.0149
		±1/2	±3/2	0.1524	0.0025	−0.2265	0.2679	−0.0952
		±1/2	±1/2	0.1810	−0.0017	0.1903	−0.2242	0.0803
3/2	5/2	±3/2	±5/2	0.3333	0.0003	−0.0205	0.0049	0.0013
		±3/2	±3/2	0.1333	−0.0019	0.0707	−0.0436	0.0081
		±3/2	±1/2	0.0333	0.0015	−0.0498	0.0380	−0.0092
		±1/2	±5/2	0	−0.0003	0.0205	−0.0049	−0.0013
		±1/2	±3/2	0.2000	0.0018	−0.0704	0.0430	−0.0078
		±1/2	±1/2	0.3000	−0.0015	0.0498	−0.0380	0.0092
3/2	1/2	±3/2	±1/2	0.5000	0	0	0	0
		±1/2	±1/2	0.5000	0	0	0	0
2	0	All five transitions		0.2000	0	0	0	0
5/2	1/2	All three transitions		0.3333	0	0	0	0

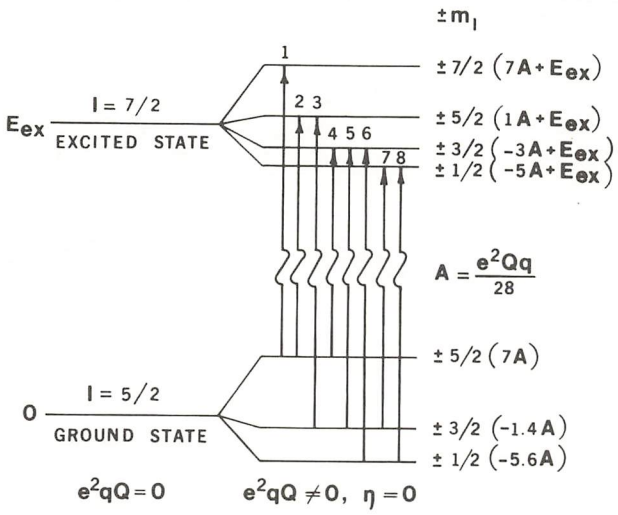

ENERGY LEVEL DIAGRAM

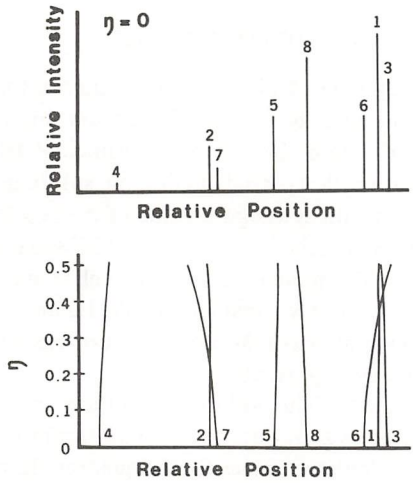

EFFECT OF η ON THE ENERGY TRANSITIONS

Fig. 6.24. Quadrupole splittings for ^{121}Sb.

no preferred direction for the small crystals, the intensities of the two peaks will be the same. An additional requirement, however, is that there be no lattice anisotropy. If there are preferred directions, the intensities will be unequal. This is illustrated in Fig. 6.25 where the intensities are plotted as a function of the angle between the direction of the gamma and the crystallographic z direction.

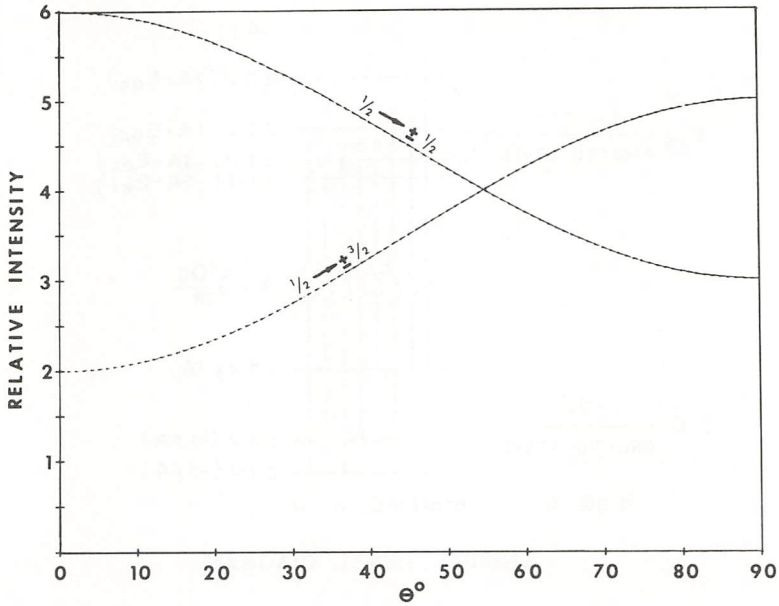

Fig. 6.25. Relative intensities of the two quadrupolar split absorption peaks as a function of the angle between the direction of the gamma and the crystallographic direction.

C. ADDITIVE MODEL

The quadrupole coupling data can be used quite successfully with the additive model. This model has similarities to the partial chemical shifts discussed in Section V.D. Using the equations in Table 6.XV and the experimental data, *A*'s, *B*'s . . . can be determined. These values are called partial quadrupole splittings (pqs). To determine the rest of the pqs values, one must assign a value of the pqs for one ligand. These values can then be used to assist in the interpretation of Mössbauer data on substances about which little is known. The model works quite well in most instances because, although the equations in Table 6.XV consider only the ligand contribution to q, they are also applicable to the populations of the molecular orbitals when the orbitals are in the direction of the ligands, as they usually are.

Examples of the usefulness of the additive model are apparent in Table 6.VIII. Using pqs values for chloride as zero, for methyl as 13.0 mm/s, and for the lone pair as 7.5 mm/s, one gets the calculated values for the quadrupole splitting shown there. The relative values of the pqs for these ligands indicate, as expected, that the methyls are electron-donating while the chlorides are electron-withdrawing.

Many other examples have been reported by Bancroft and are summarized in a book (3). This model has also been extensively discussed by M.G. Clark (11).

VIII. SPIN HAMILTONIAN AND RELAXATION

The principal interactions discussed in Section III can be collected and the interaction Hamiltonian written as

$$\mathcal{H}_{\text{Int}} = \mathcal{H}_{(E0)} + \mathcal{H}_{(M1)} + \mathcal{H}_{(E2)} \tag{60}$$

The magnetic interaction $\mathcal{H}_{(M1)}$ consists of the nuclear Zeeman interaction (Z), the orbital term (L), and the magnetic or spin hyperfine interaction (M):

$$\mathcal{H}_{(M1)} = \mathcal{H}_Z + \mathcal{H}_L + \mathcal{H}_M \tag{61}$$

The nuclear Zeeman interaction occurs when there is an externally applied magnetic field, while the magnetic hyperfine interaction is due to internal magnetic fields produced by the electronic spins. These internal fields produce the Fermi contact and dipole interactions which have been discussed in Section VI along with the orbital term in equation 61.

The magnetic hyperfine interaction is analogous to the electric quadrupole interaction, which is an electric hyperfine interaction. A magnetic hyperfine tensor $\vec{\vec{A}}$, similar to the electric field gradient tensor of equation 25, can be defined and a spin Hamiltonian written as

$$\mathcal{H}_M = \vec{I} \cdot \vec{\vec{A}} \cdot \vec{S} \tag{62}$$

where $\vec{I}$ is the instrinsic nuclear spin and $\vec{S}$ is the effective electronic spin. For many applications $\vec{\vec{A}}$ can be taken to be diagonal, i.e.,

$$\vec{\vec{A}} = \begin{pmatrix} A_x & 0 & 0 \\ 0 & A_y & 0 \\ 0 & 0 & A_z \end{pmatrix}$$

Substituting the above tensor in equation 62 gives

$$\mathcal{H}_M = A_x I_x S_x + A_y I_y S_y + A_z I_z S_z \tag{63}$$

Following Wickman, Klein, and Shirley (45) the effects of equation 63 on the Mössbauer spectrum for iron are investigated below. The effective electronic-spin case considered is $S = 1/2$.

For the Mössbauer transition in ^{57}Fe, $I_e = 3/2$ and $I_g = 1/2$ for the excited and ground states, respectively. The excited state has $(2I_e + 1)(2S + 1) = 8$ degenerate levels while the ground state has $(2I_g + 1)(2S + 1) = 4$ degenerate levels. Each of the $2I + 1$ nuclear spin states can occur with an effective electronic spin $S_z = \pm 1/2$. With a magnetic field in the z direction only, equation 63 reduces to

$$\mathcal{H}_M = A_z I_z S_z \tag{64}$$

Since the degenerate states are not mixed by the Hamiltonian of equation 64, the energies are simply

$$E_{mM} = \langle m M \mid \mathcal{H}_M \mid m M \rangle \tag{65}$$

where m and M are the z quantum numbers of the nuclear and electron spins, respectively. Equation 65 implies four energy levels for the excited state and two for the ground state. However, each of these levels have two-fold degeneracy (see Fig. 6.26). The dipole selection rule allows for six pairs of transitions, one (see

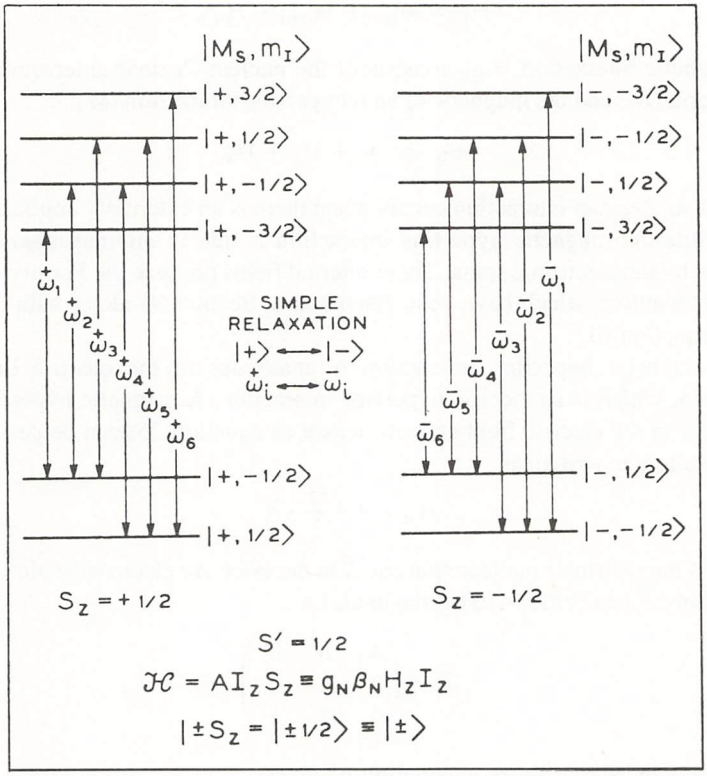

Fig. 6.26. Twofold degeneracy of energy levels in ^{57}Fe where the z component of the effective electron spin can have values $S_z = \pm\frac{1}{2}$. Reproduced by permission from *Phys. Rev.* (45).

Fig. 6.7) for each of the two electronic spin states. Since the Lorentzian pairs overlap, the resulting Mössbauer spectrum consists of six line shapes.

Maintaining axial symmetry, but allowing small transverse magnetic fields such that $A_x = A_y \ll A_z$, the Mössbauer spectrum becomes more complicated. Note that the components of the hyperfine tensor are different for the excited and the ground states. The spin Hamiltonian equation 63 in terms of raising and lowering operators is

$$\mathcal{H}_M = A_z I_z S_z + \left(\frac{A_x + A_y}{4}\right)(I_+S_- + I_-S_+) + \left(\frac{A_x - A_y}{4}\right)(I_+S_+ + I_-S_-) \quad (66)$$

The last term in equation 66 is zero when $A_x = A_y$. However, the second term removes the degeneracy of the $|\pm 1/2, \mp 1/2\rangle$ states in both the excited and ground nuclear levels. The splitting is illustrated in Fig. 6.27 which also indicates the second-order nondegenerate perturbation shifts on the adjacent pairs in the excited nucleus. Two transitions between the split levels are forbidden and the resulting spectrum consists of ten line shapes.

For the case $A_z \gg A_x > A_y$, the axial symmetry is destroyed. The third term in equation 66 splits the degenerate levels $|\pm 1/2, \pm 1/2\rangle$ in both excited and ground-

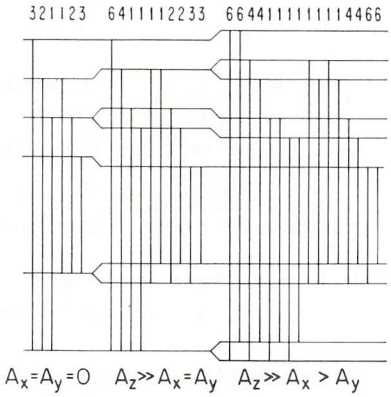

Fig. 6.27. Energy levels and transitions with relative intensities for ^{57}Fe (effective electronic spin case $S=\frac{1}{2}$) under various magnetic hyperfine interactions. Reproduced by permission from *Phys. Rev.* (45).

state nuclei. Adjacent levels in the excited nuclear state are shifted in second order (see Fig. 6.27). The Mössbauer spectrum now has 16 different transition energies.

The above considerations assume static magnetic fields. However, the internal fields at the nuclear sites are time dependent. The simple case of a random or randomly fluctuating magnetic field in the z direction is considered below with particular attention given to rapid fluctuations (fast relaxation) and slow fluctuations (slow relaxation). To determine whether the magnetic field is changing rapidly, one compares the time for the field to change polarity (τ) with the period (τ_L) of the Larmor precession. A magnetic moment $\vec{\mu} = \gamma \vec{I}$ in a constant magnetic field $\vec{H} = (0,0,H)$ rotates about the z axis with the Larmor frequency $\omega_L = \gamma H$. The discussion below is patterned after Blume and Tjon (8).

The line shape for gamma emission is determined by the transition probability (27) (for an exponential decay law)

$$P(E_\gamma) = \frac{|\langle f | \mathcal{H}^{(+)} | i \rangle|^2}{(E_\gamma - E_f + E_i)^2 + \Gamma^2/4} \tag{67}$$

In equation 67 i and f represent the initial (excited) and final (ground) states respectively, E_γ is the gamma energy, Γ is the line width, and $\mathcal{H}^{(+)}$ contains the creation operator for the photon.

The energies of the nuclear states $| I\ m \rangle$ are found from the unperturbed and the spin Hamiltonians

$$\mathcal{H} = \mathcal{H}_0 + A_z I_z(1/2) \tag{68}$$

where the effective spin is assumed to be constant ($S_z = 1/2$) for the moment. It is the effective spin that produces the internal magnetic field at the nucleus. There is a finite probability for the effective spin to flip to $S_z = -1/2$; such transitions induce the time-dependent magnetic fields. The energies calculated from equation 68 are

$$E_i = \langle I_e\ m_e | \mathcal{H} | I_e\ m_e \rangle = E_e + \frac{A_e}{2} m_e \equiv E_e + g\beta H\ m_e \tag{69a}$$

$$E_f = \langle I_g\, m_g \mid \mathcal{H} \mid I_g\, m_g \rangle = E_g + \frac{A_g}{2} m_g \equiv E_g + g'\beta H\, m_g \tag{69b}$$

where H is the internal magnetic field, g and g' are Landé factors, and β is the Bohr magneton. The probability for the emission of a photon with energy E_γ is obtained by averaging over the four initial states and summing over final states:

$$P(E_\gamma) = 1/4 \sum_{m_e m_g} \frac{\mid \langle I_g\, m_g \mid \mathcal{H}^{(+)} \mid I_e\, m_e \rangle \mid^2}{[E_\gamma - E_o - (gm_e - g'm_g)\beta H]^2 + \Gamma^2/4} \tag{70}$$

where $E_o = E_e - E_g$. If $H = 0$, there is one Lorentian peek at $E_\gamma = E_o$; however, equation 70 implies six Lorentzians when $H \neq 0$ with peaks $E_\gamma = E_o + (gm_e - g'm_g)$.

The fluctuations of the magnetic field due to the spin of the electronic spins can be easily incorporated in the calculations by letting

$$H \rightarrow H f(t) \tag{71}$$

where $f(t)$ randomly takes on values of ± 1.

The generalization of equation 70 for time dependent fields is (8,46)

$$P(E_\gamma) = \frac{2}{\Gamma} Re \int_0^\infty e^{\,iE_\gamma t/\hbar - \frac{1}{2}\Gamma t}\, G(t)\, dt \tag{72}$$

where

$$G(t) = 1/4 \sum_{m_e m_g} \mid \langle I_g m_g \mid \mathcal{H}^{(+)} \mid I_e m_e \rangle \mid^2 e^{-iE_o t/\hbar}$$

$$\overline{X \exp[-i(gm_e - g'm_o)\,\beta\, H \int_0^t f(t')dt']} \tag{73}$$

The bar in equation 73 designates averaging. When the magnetic field is constant, i.e., $f(t) = 1$, one finds

$$G(t) = 1/4 \sum_{m_e m_g} \mid \langle I_g m_g \mid \mathcal{H}^{(+)} \mid I_e m_e \rangle \mid^2 e^{-i[E_o + (gm_e - g'm_o)\beta H t]/\hbar} \tag{74}$$

If equation 74 is substituted into equation 72, the real part of the resulting integral gives equation 70.

Defining $\alpha = g'm_o - gm_e$, the average needed in equation 73 is (1,8)

$$e^{i\alpha \int_0^t f(t')\, dt'} = \left(\cos xWt + \frac{\sin xWt}{x}\right) e^{-Wt} \tag{75}$$

where $W \approx 1/\tau$ is the probability for the effective spin to flip and $x = (\alpha^2/W^2 - 1)^{\frac{1}{2}}$. For slow relaxation $\tau \gg \tau_L \approx \dfrac{1}{\alpha}$, i.e., $W \ll \alpha$ and

$$e^{i\alpha \int_0^t f(t')dt'} \approx \cos \alpha\, t = 1/2(e^{i\alpha t} + e^{-i\alpha t}) \tag{76}$$

using equation 75. Equation 76 implies two sets of six Lorentzians (see Fig. 6.27); there will be six line shapes in the Mössbauer spectrum as pairs overlap.

For fast relaxation $W \gg \alpha$ and $x = \sqrt{-1} = i$. The right side of equation 75 becomes

$$\left(\cos iWt + \frac{\sin iWt}{i}\right) e^{-Wt} = e^{-i(iWt)} e^{-Wt} = 1 \tag{77}$$

using the Euler formula

$$\cos\theta + \sin\theta/i = \cos\theta - i\sin\theta = e^{-i\theta} \tag{78}$$

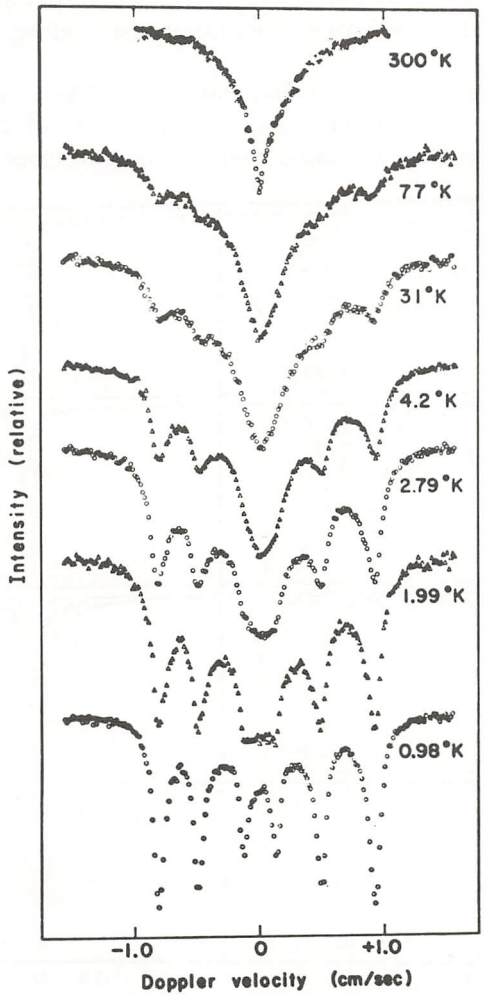

Fig. 6.28. ^{57}Fe Mössbauer spectra of Ferrichrome A at various temperatures. Reproduced by permission from *Phys. Rev.* (45).

Equation 73 is then simply

$$G(t) = 1/4 \sum_{m_e m_g} | \langle I_g m_g | \mathcal{H}^{(+)} | I_e m_{ei} \rangle |^2 e^{-iE_0 t} \tag{79}$$

and equation 70 reduces to

$$P(E_\gamma) = 1/4 \sum_{m_e m_g} \frac{| \langle I_g m_g | \mathcal{H}^{(+)} | I_e m_e \rangle |^2}{(E_\gamma - E_0)^2 + \Gamma^2/4} \tag{80}$$

The Mössbauer spectrum consists of one line shape. The fluctuations of the magnetic field are so rapid that the field at the nucleus averages to zero during times of the order of the Larmor period. Fig. 6.28 indicates how the six line shapes reduce to one as temperature is increased. Increasing temperature induces rapid spin flips and therefore fast relaxation. However, due to other factors the resulting single line is non-Lorentzian.

An alternative approach to relaxation employs the Bloch equations (1,31). A theoretical spectrum using this approach is given for iron (45,46) in Figure 6.29. Once again, the six line shapes collapse to one as relaxation times become short.

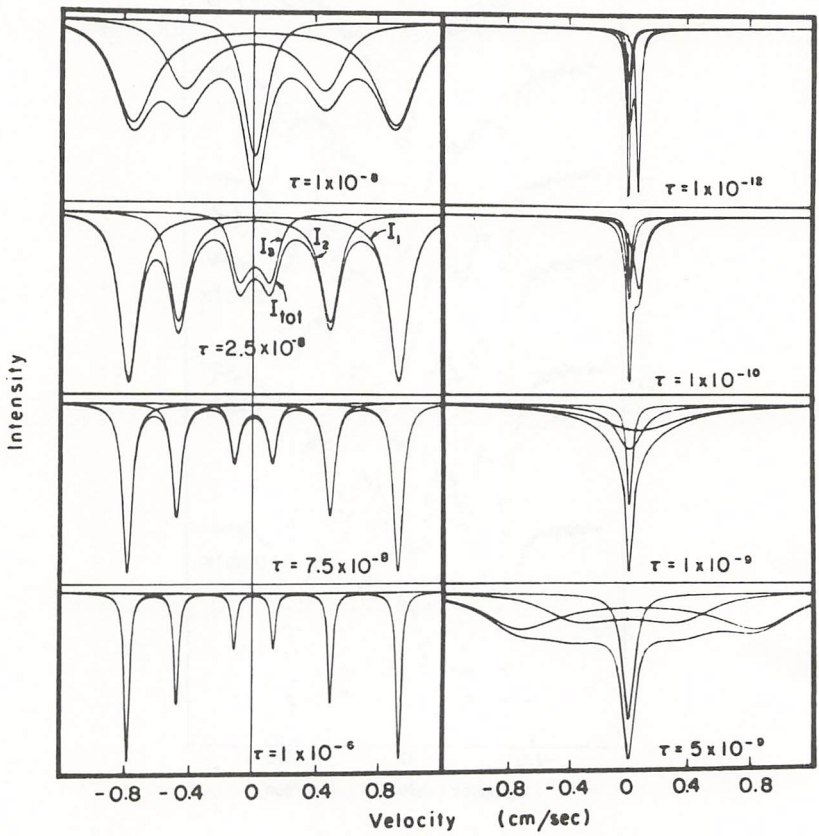

Fig. 6.29. ^{57}Fe iron relaxation spectra for Ferrichrome A with various relaxation times. Reproduced by permission from *Phys. Rev.* (45).

Acknowledgments

We express our special appreciation to Virginia Stevens and Robert Detjen who have laboriously proofread the text. We thank Karen Ball and Mary Jane Winfrey for typing this manuscript and Julie Blankenship for preparation of the figures. This chapter has been adapted from a set of notes for a course on Mössbauer spectroscopy and we wish to thank the students for their suggestions and comments.

APPENDIX

Nomenclature and Conventions for Reporting Mössbauer Spectroscopic Data

I. INTRODUCTION

The guidelines that follow are based considerably on the reports of several groups; most notably the Mössbauer Spectroscopy Task Group of Committee E-4 (Metallography) of the American Society for Testing and Materials, the *ad hoc* Panel on Mössbauer Data of the Numerical Data Advisory Board of the Division of Chemistry and Chemical Technology of the National Research Council (USA), and the Commission on Molecular Structure and Spectroscopy (Physical Chemistry Division) of the International Union of Pure and Applied Chemistry.

II. CONVENTIONS FOR THE REPORTING OF MÖSSBAUER DATA

A. TEXT

The text should include information about the following:

1. Method of sample mounting, sample thickness control, sample confinement, and appropriate composition data for alloys, solid solutions, or frozen solution samples;
2. Absorber form (single crystal, polycrystalline powder, inert matrix if used, evaporated film, rolled foil, isotopic enrichment, etc.);
3. Apparatus and detector used and comments about associated electronics (e.g., single-channel window, escape-peak measurements, solid-state detector characteristics, etc.) if appropriate or unusual; data acquisition time if unusual;
4. Geometry of the experiment (transmission, scattering, in-beam, angular dependence, etc.); direction and strength of applied magnetic field if used;
5. Critical absorbers of filters if used;
6. Method of data reduction (e.g., visual, computer, etc.) and curve-fitting procedure; (1)
7. Isomer-shift convention used or the isomer shift of a standard (reference) absorber. Positive velocities are defined as source approaching absorber. Sufficient details concerning the isomer shift standard should be included to facilitate interlaboratory comparison of data;

8. Method of energy calibration (e.g., calibrated absorber, Michelson interferometer, Moiré fringes, etc.);

9. An estimate of systematic and statistical errors of the quoted parameters.

B. NUMERICAL OR TABULATED DATA

Information collected and summarized in tabular form should include:

1. Chemical state of source matrix and absorber;

2. Temperature of source and absorber and the constancy of these parameters over the length of the data acquisition period;

3. Values of the parameters required to characterize the features in the Mössbauer spectrum (given in mm/s or other appropriate units) with estimated errors (see below the section on "Terminology, Symbols, and Units" for parameters used);

4. Isomer shift reference point with respect to which the positional parameter is reported;

5. Observed line widths defined as the full-width at half-maximum peak-height or other appropriate line width (e.g., line widths calculated by a transmission integral computer fit, line widths of the single Lorentzian peaks when the spectrum is the result of a sum of overlapping Lorentzian peaks, etc);

6. Line intensities or (relative) area of each component of the hyperfine interaction spectrum observed, if pertinent.

C. FIGURES ILLUSTRATING SPECTRA

Scientific communications in which Mössbauer effect measurements constitute a primary or significant source of experimental information should include an illustration of one spectrum (i.e., percent transmission or absorption or counting rate versus an appropriate energy parameter) to indicate the quality of the data. Such figures should include the following information:

1. A horizontal axis normally scaled in velocity (mm/s; channel number or analyzer address values should not be used for this purpose);

2. A vertical axis normally scaled in terms of the effect magnitude, transmission per scattering intensity, counts per channel, or related units; (2)

3. Statistical counting error limits indicated for at least one data point; (3)

4. Individual data points (rather than a smoothed curve alone) should be shown. Computed fits should be indicated in such a way that they are clearly distinguished from the experimental points.

III. TERMINOLOGY, SYMBOLS, AND UNITS

If the units selected by the experimenter are not SI units, they should be defined in the text.

Name	Symbol	SI Unit	Suggested decimal multiple of submultiple SI Units for Mössbauer data	Definition and comments
Isomer Shift	δ	m/s	mm/s ($=10^{-3}$m/s)	Measure of the energy difference between the source (E_s) and the absorber (E_a) transition. The measured Doppler velocity shift, δ, is related to the energy difference by $E_a - E_s = E_\gamma v/c$ (where E_γ is the Mössbauer gamma energy and c is the speed of light in a vacuum). [4],[5]
Nuclear/gyromagnetic ratio	γ	$T^{-1}s^{-1}$		The parameter that is the proportionality constant between the nuclear moment and the angular momentum. [6]

III. TERMINOLOGY, SYMBOLS, AND UNITS *(Cont.)*

Name	Symbol	SI Unit	Suggested decimal multiple of submultiple SI Units for Mössbauer data	Definition and comments
Magnetic flux density	B	T		Magnetic flux density at the nucleus (from experiment) in those cases in which the magnetic hyperfine interaction can be described by an effective field. In other cases the tensor components of the magnetic hyperfine interaction should be reported if possible.
Magnetic hyperfine splitting	$\gamma \hbar B$	J	mm/s($=10^{-3}$m/s)	The energy difference between two adjacent levels that are the results of the interaction of the nuclear magnetic dipole moment and the magnetic flux density. (5)
Components of the magnetic hyperfine interaction tensor	A_x, A_y, A_z	J	mm/s($=10^{-3}$m/s)	Used when the magnetic hyperfine interaction is to be described by the Hamiltonian $\vec{I} \cdot \overleftrightarrow{A} \cdot \vec{S}$.(7)
Nuclear quadrupole moment (spectroscopic)	eQ	Cm^2		A parameter that describes the effective shape of the equivalent

				ellipsoid of nuclear charge distribution $Q>O$ for a prolate (e.g., ^{57}Fe, ^{197}Au) and $Q < O$ for an oblate (e.g., ^{119}Sn, ^{129}I) nucleus.
Electric field gradient (EFG) tensor		V/m^2		A second-rank tensor describing the electric field gradient specified by η and V_{zz}.[8]
Principal component of EFG	$-V_{zz}$	V/m^2		$\partial^2 V/\partial z^2 = eq$ (e is the proton charge, V_{zz} is the largest component of the diagonalized EFG).
Quadrupole coupling constant	e^2qQ/h	Hz	MHz($=10^6$Hz)	Product of V_{zz}/h and the nuclear quadrupole moment, eQ.[5]
Asymmetry	η			$= (V_{xx} - V_{yy})/V_{zz}$.
Line width	W	m/s	mm/s($=10^{-3}$m/s)	Full width at half maximum of the observed resonance line(s).[5]
Natural line width	W_0	m/s	mm/s($=10^{-3}$m/s)	Theoretical value of the full width at half maximum, usually calculated from lifetime data.

III. TERMINOLOGY, SYMBOLS, AND UNITS *(Cont.)*

Name	Symbol	SI Unit	Suggested decimal multiple of submultiple SI Units for Mössbauer data	Definition and comments
Resonance effect magnitude	I_0			The difference in the transmitted or scattered intensity at resonance maximum and off-resonance, relative to the intensity off resonance. [9]
Recoil-free fraction	f			The fraction of all gamma rays of the Mössbauer transition which are emitted (f_s) or absorbed (f_a) without recoil energy loss.[10]
Mössbauer thickness	t			The effective thickness of a source (t_s) or an absorber (t_a) in the optical path. [11]
Resonance/cross section	σ_0	m^2		The cross section for resonant absorption of the Mössbauer gamma ray. [12]
Vibrational anisotropy	ε_m			When the vibrational anisotropy tensor ($\langle x^2_{ij} \rangle$) is axially

symmetric $\varepsilon_m = (1/\lambda\!\!\!^{-2})$ $(\langle x_{\parallel}^2 \rangle - \langle x_{\perp}^2 \rangle)$ where $\langle x_{\parallel}^2 \rangle$ and $\langle x_{\perp}^2 \rangle$ are the mean square vibrational amplitudes of the Mössbauer nucleus parallel and perpendicular to the cylindrical symmetry axis through the Mössbauer atom and $\lambda\!\!\!^{-}$ is the wavelength of the Mössbauer radiation divided by 2π.

FOOTNOTES

(1) If data are analyzed by computer, a brief description of the program should be given to identify the algorithm used. The number of constraints should be specified (e.g., equal line widths or intensities, etc.) and a measure of the goodness of fit should be indicated.

If measurements of very high accuracy are reported and the discussion of the reality of small effects is an important part of the work, then the following items should be included:

a. the functional form and all parameters used in fitting (i.e., the constraints should be clearly stated);

b. the treatment of the background (e.g., assumed energy independent, experimentally subtracted, etc.);

c. the relative weighting of abscissa and ordinate (e.g., equal weighting);

d. a measure of the statistical reliability;

e. the number of replications and the agreement between these if applicable;

f. an estimate of systematic errors as primary results.

(2) It has become customary to display data obtained in transmission geometry with the resonance maximum "down" and scattering data with the resonance maximum "up." In either case, sufficient data should be shown far enough from the resonance peaks to establish the nonresonant base line.

(3) In most instances (where the data are uncorrected counting results), the standard deviation (i.e., the square root of the second moment of the distribution) is given by $\pm N^{\frac{1}{2}}$, where N is the number of counts scaled per velocity point. For corrected data (i.e., when background or other nonresonant effects are subtracted from the raw data), the propagated error should be computed by normal statistical methods which are briefly described in the figure legend. Fiducial marks bracketing the data points to show the magnitude of the standard deviation are often used in indicating the spread of the data.

(4) The center of a Mössbauer spectrum is defined as the Doppler velocity at which the resonance maximum is (or would be) observed when all magnetic dipole, electric quadrupole, etc. hyperfine interactions are (or would be) absent. The contribution of the second-order Doppler shift should be indicated, if possible. The isomer shift is the sum of this term and the chemical isomer shift.

(5) The SI unit of energy for isomer shift, quadrupole-coupling constant, quadrupole splitting, and line width is the Joule. The measured quantity is the velocity (m/s) which can be converted to the desired energy units.

(6) The nuclear gyromagnetic ratio can be expressed in terms of the nuclear g factor (Landé factor) as $\gamma\hbar = g\mu_N$ where μ_N is called the nuclear magneton and is defined as $\mu_N = eh/2m_pc$ (m_p is the mass of the proton). Another quantity that is often used is the nuclear magnetic moment (μ) which is related to γ and g by $\mu = \gamma hI = g\mu_N I$. The usual unit for μ is μ_N, i.e., nuclear magnetons. Note that the units of γh are JT^{-1}.

(7) In the case of an isotropic interaction the symbol "a" is used (i.e., $a = A_x = A_y = A_z$).

(8) The sum $V_{xx} + V_{yy} + V_{zz} = 0$ regardless of the choice of axes. In the absence of magnetic hyperfine interaction, principal axes are chosen so that the off-diagonal matrix elements vanish, $V_{ij} = 0(i,j = x,z;\ i \neq j)$ and are defined such that $|V_{zz}| \geqslant |V_{yy}| \geqslant |V_{xx}|$, so that $0 \leqslant \eta \leqslant 1$. $(\mathrm{EFG})_{ij} = -(\partial^2 V/\partial x_i \partial x_j)$, where $x_i, x_j = x, y, or\ z$.

(9) This parameter is calculated from the relationship $I_0 = [N(\infty) - N(0)]/N(\infty)$, where $N(0)$ is the counting (or transmission or scattering intensity) at the resonance maximum, and $N(\infty)$ is the corresponding rate at a velocity at which the resonance effect is negligible. If corrections for nonresonant gamma- or X-rays, or other base line corrections have been made in evaluating I_0, these should be listed.

(10) The recoil-free fraction can be related to the expectation value of the mean square displacement of the Mössbauer atom by the relationship $f = \exp(-k^2\langle x^2\rangle)$ where k is the wave number of the Mössbauer gamma ray and x is the displacement taken along the optical axis.

(11) The t parameter is usually calculated from the relationship $t = n \cdot \sigma_0 \cdot IA$, in which n is the number of Mössbauer element atoms per unit area in the optical path, σ_0 is the cross section for recoilless scattering, IA is the fractional abundance of the Mössbauer transition active nuclides, and f is the recoil-free fraction (*vide supra*).

(12) This parameter is usually calculated from the relationship
$\sigma_0 = (h^2c^2/2\pi)E_\gamma^{-2}(1 + 2I_e)(1 + 2I_g)^{-1}(1 + \alpha_T)^{-1}(W_0/2W_a)$,
where E_γ is the transition energy; W_a is the absorber line width; I_e and I_g are the excited and ground-state spins, respectively, and α_T is the total internal conversion coefficient of the Mössbauer transition.

REFERENCES

1. Abragam, A., *The Theory of Nuclear Magnetism*, Oxford University, London (1961).
2. Asch, L., and G. M. Kalvius, "Calculated Sample Thicknesses for Absorbers," in J. G. Stevens, Ed., "Mössbauer Spectroscopy," in J. W. Robinson, Ed., *CRC Handbook of Spectroscopy, Volume 3*, CRC Press, Boca Raton, Florida, 1981, pp. 404-416.
3. Bancroft, G. M., *Mössbauer Spectroscopy, An Introduction for Inorganic Chemists and Geochemists*, McGraw Hill, New York (1973).
4. Bancroft, G. M., M. J. Mays, and B. E. Prater, *J. Chem. Soc. (A)*, 956 (1970).
5. Bancroft, G.M., "Point Charge Model Tables," in J. G. Stevens, Ed., "Mössbauer Spectroscopy," in J. W. Robinson, Ed., *CRC Handbook of Spectroscopy, Volume 3*, CRC Press, Boca Raton, Florida, 1981, pp. 480-490.
6. Benczer-Koller, N., and R. H. Herber, "Experimental Methods," in V. I. Gol'danskii and R. H. Herber, Eds., *Chemical Applications of Mössbauer Spectroscopy*, Academic, New York, 1968, pp. 114-158.
7. Berrett, R. R., and B. W. Fitzsimmons, *J. Chem. Soc. (A)*, 525 (1967).
8. Blume, M., and J. A. Tjon, *Phys. Rev.*, **165**, 446 (1968).
9. Biscar, J. P., W. Kundig, H. Bommel, and R. S. Hargrove, *Nucl. Instr. Methods*, **75**, 165 (1969).
10. Bowen, L. H., "^{121}Sb Mössbauer Spectroscopy," in J. G. Stevens and V. E. Stevens, Eds., *Mössbauer Effect Data Index—1972*, Plenum, 1973, pp. 71-110.
11. Clark, M. G., "Hyperfine Interactions and Molecular Structure," in A. D. Buckingham, Ed., *Molecular Structure and Properties*, Butterworths, London, 1975, pp. 239-297.
12. Cohen, R. L., and G. K. Wertheim, "Experimental Methods in Mössbauer Spectroscopy," in R. V. Coleman, Ed., *Methods of Experimental Physics, 11*, Academic, New York, 1974, pp. 307-369.
13. Cosgrove, J. G., and R. L. Collins, *Nucl. Instr. Methods*, **95**, 269 (1971).
14. De Waard, H., *Rev. Sci. Instr.*, **36**, 1728 (1965).
15. Fischer, H., and U. Gonser, "Relative Line Intensities of Magnetic Hyperfine Interactions," in J. G. Stevens, Ed., "Mössbauer Spectroscopy," in J. W. Robinson, Ed., *CRC Handbook of Spectroscopy, Volume 3*, CRC Press, Baca Raton, Florida, 1981, pp. 451-465.
16. Greenwood, N. N., and T. C. Gibb, *Mössbauer Spectroscopy*, Chapman and Hall, London (1971).
17. Gütlich, P. "Mössbauer Spectroscopy in Chemistry," in U. Gonser, Ed., *Mössbauer Spectroscopy*, Springer-Verlag, New York, 1975, pp. 53-96.
18. Herber, R. H., *Inorg. Chem.*, **3**, 101 (1964).
19. Kaindl, G., K. Leary, and N. Bartlett, *J. Chem. Phys.*, **59** 5050 (1973).
20. Kaindl, G., W. Potzel, F. Wagner, U. Zahn, and R. L. Mössbauer, *Z. Phys.*, **226**, 103 (1969).
21. Kalvius, G. M., "Mössbauer Spectroscopy in the Actinides," in *Mössbauer Spectroscopy and Its Applications*, International Atomic Energy Agency, 1972, pp. 169-196.
22. Kalvius, G. M., and E. Kankeleit, "Recent Improvements in Instrumentation and Methods of Mössbauer Spectroscopy," in *Mössbauer Spectroscopy and Its Applications*, International Atomic Energy Agency, Vienna, 1972, pp. 9-88.
23. Kistner, O. C., and A. W. Sunyar, *Phys. Rev. Lett*, **4**, 412 (1960).
24. Lees, J. K., Ph.D. Thesis, Carnegie Institute of Technology (1966).

25. Lindqvist, I., and Aiggli, *J. Inorg. Nucl. Chem.*, **2**, 345 (1956).
26. Margulies, S., and J. R. Ehrman, *Nucl. Instr. Methods*, **12**, 131 (1961).
27. Merzbacher, E., *Quantum Mechanics*, John Wiley, New York (1961).
28. Mössbauer, R. L., *Z. Physik*, **151**, 124 (1958).
29. Nowik, I., and E. R. Bauminger, "^{170}Yb Mössbauer Spectroscopy," in J. G. Stevens and V. G. Stevens, Ed., *Mössbauer Effect Data Index—1975*, Plenum, 1976, pp. 407–442.
30. Pasternak, M., A. Simopoulos, and Y. Hazony, *Phys. Rev.*, **140A**, 1892 (1965).
31. Pople, J. A., W. G. Schneider, and H. J. Bernstein, *High-Resolution Nuclear Magnetic Resonance*, McGraw Hill, New York (1959).
32. Ruby, S. L., G. M. Kalvius, G. B. Beard, and R. E. Snyder, *Phys. Rev.*, **159**, 239 (1967)
33. Shenoy, G. K., and B. D. Dunlap, *Nucl. Instr. Meth.*, **71**, 285 (1969).
34. Shenoy, G. K., and B. D. Dunlap, "Constants in Isomer Shift Expression," in G. K. Shenoy, and F. E. Wagner, Eds., *Mössbauer Isomer Shifts*, North-Holland, New York, 1978, pp. 889–894.
35. Shenoy, G. K., and F. E. Wagner, *Mössbauer Isomer Shifts*, North-Holland, New York, 1978.
36. Shirley, D. A., *Rev. Mod. Phys.*, **36**, 339 (1964).
37. Stadnik, Z. M., *Mössbauer Effect Ref. Data J.*, **1**, 217 (1978).
38. Stevens, J. G., and B. D. Dunlap, *J. Phys. Chem. Ref. Data*, **5**, 1093 (1976).
39. Stevens, J. G., J. M. Trooster, and H. A. Meinema, *Inorg. Chem.*, **20**, 801 (1981).
39a. Stevens, J. G., and G. K. Shenoy, Eds., *Mössbauer Spectroscopy and Its Chemical Applications*, American Chemical Society, Washington, 1981.
40. Trooster, J. M., and M. P. A. Viegers, *Mössbauer Effect Ref. Data J.*, **1**, 154 (1978).
41. Van der Woude, F., and G. A. Sawatzky, *Phys. Rep.*, **12**, 335 (1974).
42. Viste, A., and H. B. Gray, *Inorg. Chem.*, **3**, 1113 (1964).
43. Walker, L. R., G. K. Wertheim and V. Jaccarino, *Phys. Rev. Lett.*, **6**, 98 (1961).
44. Watson, R. E., and A. J. Freeman, *Phys. Rev.*, **123**, 2027 (1961).
45. Wickman, H. H., M. P. Klein, and D. A. Shirley, *Phys. Rev.*, **152**, 345 (1966).
46. Wickman, H. H., and G. K. Wertheim, "Spin Relaxation in Solids and Aftereffects of Nuclear Transformations," in V. I. Gol'danskii and R. H. Herber, Eds., *Chemical Applications of Mössbauer Spectroscopy*, Academic, New York, 1968, pp. 548–621.
47. Wolfsberg, M., and L. Helmholtz, *J. Chem. Phys.*, **20**, 837 (1952).